Brigham Young University
BYU ScholarsArchive

All Theses and Dissertations

2011-04-19

Experimental Investigation of Steel Pipe Pile to Concrete Cap Connections

Ryan S. Eastman
Brigham Young University - Provo

Follow this and additional works at: https://scholarsarchive.byu.edu/etd

Part of the Civil and Environmental Engineering Commons

BYU ScholarsArchive Citation

Eastman, Ryan S., "Experimental Investigation of Steel Pipe Pile to Concrete Cap Connections" (2011). *All Theses and Dissertations*. 2628.
https://scholarsarchive.byu.edu/etd/2628

This Thesis is brought to you for free and open access by BYU ScholarsArchive. It has been accepted for inclusion in All Theses and Dissertations by an authorized administrator of BYU ScholarsArchive. For more information, please contact scholarsarchive@byu.edu, ellen_amatangelo@byu.edu.

Experimental Investigation of Steel Pipe

Pile to Concrete Cap Connections

Ryan S. Eastman

A thesis submitted to the faculty of
Brigham Young University
in partial fulfillment of the requirements for the degree of

Master of Science

Paul W. Richards, Chair
Fernando S. Fonseca
Kyle M. Rollins

Department of Civil and Environmental Engineering

Brigham Young University

June 2011

Copyright © 2011 Ryan S. Eastman

All Rights Reserved

ABSTRACT

Experimental Investigation of Steel Pipe Pile to Concrete Cap Connections

Ryan S. Eastman
Department of Civil and Environmental Engineering
Master of Science

Piles are often used to resist vertical and lateral loads when shallow foundations are inadequate or uneconomical. A critical part in designing pile foundations is the pile-to-cap connection. When a moment resisting connection is desired, reinforcement is typically used between the pile and the cap. A pile-to-cap connection with sufficient pile embedment depth, however, may provide similar results. One model that is currently used to determine the capacity of a pile-to-cap connection was developed by Marcakis and Mitchell for steel members embedded in concrete. This model considers an embedment mechanism that resists rotation at the connection. Recent testing has shown, however, that this model is conservative and that additional mechanisms contribute to the strength of the connection.

An experimental study was conducted to investigate pile-to-cap connections for pipe piles without reinforcement. Three pile-to-cap specimens with varying pile embedment depth were loaded laterally to failure. The results from the testing confirm that pile-to-cap connections with shallow pile embedment depth have significant stiffness. An improved model was developed to estimate elastic and ultimate capacities of embedded connections. In addition to the embedment mechanism used by Marcakis and Mitchell, this model includes a bearing mechanism at the end of the pile. For pile-to-cap connections with a large pile bearing area to pile embedment depth ratio, this bearing mechanism provides more strength than the embedment mechanism. For pile-to-cap connections with a small pile bearing area to pile embedment depth ratio, this bearing mechanism has little contribution to the strength of the connection.

Keywords: pile, pile-to-cap, embedment, foundation

ACKNOWLEDGMENTS

Many individuals made valuable contributions to the work presented in this paper. I wish to thank my committee chair, Dr. Paul W. Richards, for the time, counsel, and technical advice he provided. I would also like to thank Dr. Fernando S. Fonseca and Dr. Kyle M. Rollins for being a part of my graduate committee. In addition, I thank the Oregon Department of Transportation for providing the pile-to-cap connection detail used in the testing.

My family has also provided a significant amount of loving support throughout this journey. I especially thank my wife Jamie for her generous encouragement. Her patience has also been evident, as our time together has been sacrificed to allow me to complete this document. I also appreciate my parents, Randy and Delores, for their guidance and examples throughout my life.

I would also like to acknowledge the funding that made this project possible. This project was funded by Contract No 069148 “Dynamic Passive Pressure of Abutments and Pile Cap” with the Utah Department of Transportation. The contract was part of a pooled-fund study supported by Departments of Transportation from California, Montana, New York, Oregon, and Utah. The project manager for UDOT was Daniel Hsiao. Despite this generous support, however, the conclusions reported in this thesis do not necessarily reflect those of the sponsors.

TABLE OF CONTENTS

LIST OF TABLES .... **vii**

LIST OF FIGURES .... **ix**

1 Introduction **1**

1.1 Common Uses for Deep Foundations 1

1.2 Fixed vs. Pinned Connections 1

1.3 Significance of Strength and Stiffness 2

1.4 Outline 3

2 Literature Review **5**

2.1 Methods for Computing Connection Capacity 5

2.2 The Marcakis and Mitchell Equation 8

2.3 Unexplained Strength of Pile-to-Cap Connections 12

3 Testing and Instrumentation **15**

4 Testing Results **21**

4.1 Specimen 1 21

4.2 Specimen 2 23

4.3 Specimen 3 25

4.4 Main Results 27

5 Discussion **35**

5.1 Elastic Strength 35

5.2 Elastic Stiffness 35

5.3 Model for Elastic Strength 40

5.4 Ultimate Strength 47

5.5 Ultimate Pile Strains 50

5.6 Model for Ultimate Strength 51

6 Conclusion 57

REFERENCES 59

Appendix A. Strain Data from Testing 61

A.1 Specimen 1 62

A.2 Specimen 2 69

A.3 Specimen 3 75

Appendix B. Displacement Data from Testing 81

B.1 Specimen 1 82

B.2 Specimen 2 85

B.3 Specimen 3 88

Appendix C. Example of Marcakis and Mitchell Procedure 91

Appendix D. Adjustment of Loads from Testing 93

Appendix E. Pile End Bearing Stress 95

E.1 Magnitude of Pile End Bearing Stress 95

E.2 Location of Pile End Bearing Stress 97

Appendix F. Example of Ultimate Strength Model 101

LIST OF TABLES

Table 3-1: Compressive Strengths of Concrete for Each Specimen..16

Table 3-2: Tensile Strength of Piles Used in Testing 16

Table C-1: Data from Marcakis and Mitchell Example..91

Table F-1: Data from Ultimate Strength Example..101

LIST OF FIGURES

Figure 2-1: Stress Distribution for Original PCI Equation (Marcakis 1979)....5

Figure 2-2: Capacity vs. Embedment Using Marcakis and Mitchell and Original PCI Design Handbook Equation for Pipes [Based on Figure 7 in (Marcakis and Mitchell 1980)]....8

Figure 2-3: Marcakis and Mitchell Model, a) Set-up for Testing, b) Stresses and Strains....9

Figure 2-4: Points from Iterative Procedure Compared with Marcakis and Mitchell Equation....11

Figure 2-5: Test Set-up for Testing by Xiao [(Xiao 2003), used without permission]....13

Figure 2-6: Test Set-up for Testing by Rollins and Stenlund [(Richards et al. 2011) used without permission]....14

Figure 3-1: Pile-to-Cap Connection Design, a) End View, b) Side View....16

Figure 3-2: Reaction Frame and Beams Used to Resist Loads....17

Figure 3-3: String Pots Used to Measure System Response, a) East-West, b) North-South....18

Figure 3-4: Strain Gages Used to Measure System Response, a) Plan View, b) Side View....18

Figure 4-1: Gap in Specimen 1 [249 kN (56 kips), 5.3 cm (2.1 in)]....22

Figure 4-2: Initial Cracking in Specimen 1 (East-West)....22

Figure 4-3: Specimen 1 at Maximum Displacement (East-West)....22

Figure 4-4: End of Cap of Specimen 1 After Testing (North-South)....23

Figure 4-5: Gap in Specimen 2 [49.3 kN (11.1 kips), 4.3 cm (1.7 in)]....24

Figure 4-6: Initial Cracking of Specimen 2 (East-West)....24

Figure 4-7: Peeling up of Concrete on the Top of Specimen 2 (East-West)....24

Figure 4-8: Cracking at the End of Specimen 2 After Testing (North-South)....25

Figure 4-9: Gap in Specimen 3 [6.2 kN (1.4 kips), 6.0 cm (2.3 in)]....26

Figure 4-10: Initial Cracking of Specimen 3 (East-West)....26

Figure 4-11: Cracking at the End of Specimen 3 (North-South)....26

Figure 4-12: Specimen 3 After Testing (East-West) 27

Figure 4-13: Lateral Load vs. Deflection, a) Specimen 1, b) Specimen 2, c) Specimen 3..........29

Figure 4-14: Lateral Load vs. Deflection of Pile 30

Figure 4-15: Strain vs. Location at Maximum Elastic Load, a) Specimen 1, b) Specimen 2, c) Specimen 3....................31

Figure 4-16: Strain vs. Depth at Maximum Elastic Load, a) Specimen 1, b) Specimen 2, c) Specimen 3....................32

Figure 4-17: Strain vs. Location at Ultimate Load, a) Specimen 1, b) Specimen 2, c) Specimen 3....................33

Figure 4-18: Strain vs. Depth at Ultimate Load, a) Specimen 1, b) Specimen 2, c) Specimen 3....................34

Figure 5-1: Elastic Moment vs. Normalized Pile Embedment Depth 36

Figure 5-2: Maximum Elastic Load vs. Normalized Pile Embedment Depth 36

Figure 5-3: Mechanisms Considered in Elastic Stiffness 37

Figure 5-4: Elastic Connection Stiffness vs. Normalized Pile Embedment Depth....................38

Figure 5-5: Elastic Total Stiffness vs. Normalized Pile Embedment Depth....................39

Figure 5-6: Strain vs. Depth at Reverse Cycle for Maximum Elastic Load, a) Specimen 1, b) Specimen 2, c) Specimen 3....................41

Figure 5-7: Strain vs. Depth at Peak Load of First Cycle, a) Specimen 1, b) Specimen 2, c) Specimen 3....................42

Figure 5-8: Stresses Used in Elastic Strength Model....................43

Figure 5-9: Model for Elastic Strength Compared with Elastic Strength of Specimens 46

Figure 5-10: Response of Specimen 1 from Testing by Rollins and Stenlund [(Richards et al. 2011), used without permission]....................48

Figure 5-11: Response of Specimen 2 from Testing by Rollins and Stenlund [(Richards et al. 2011), used without permission]....................48

Figure 5-12: Ultimate Strength and Calculated Strength vs. Pile Embedment Depth....................49

Figure 5-13: Stresses used in Ultimate Strength Model 52

Figure 5-14: Ultimate Strength Model Compared with Ultimate Strength of Specimens....................53

Figure 5-15: Ultimate Strength Model Compared with Ultimate Strength of Specimens...........54

Figure 5-16: Ultimate Strength Model with Required Coefficient of Friction............................55

Figure A-1: Strain Gauges Used to Measure the Response of the System, a) Plan View, b) Side View..61

Figure A-2: Moment vs. Strain for Gauge S1 on Specimen 1...62

Figure A-3: Moment vs. Strain for Gauge S2 on Specimen 1...62

Figure A-4: Moment vs. Strain for Gauge S3 on Specimen 1...63

Figure A-5: Moment vs. Strain for Gauge S4 on Specimen 1...63

Figure A-6: Moment vs. Strain for Gauge S5 on Specimen 1...64

Figure A-7: Moment vs. Strain for Gauge S7 on Specimen 1...64

Figure A-8: Moment vs. Strain for Gauge S6 on Specimen 1...65

Figure A-9: Moment vs. Strain for Gauge S8 on Specimen 1...65

Figure A-10: Moment vs. Strain for Gauge S9 on Specimen 1...66

Figure A-11: Moment vs. Strain for Gauge S10 on Specimen 1...66

Figure A-12: Moment vs. Strain for Gauge S11 on Specimen 1...67

Figure A-13: Moment vs. Strain for Gauge S12 on Specimen 1...67

Figure A-14: Moment vs. Strain for Gauge S13 on Specimen 1...68

Figure A-15: Moment vs. Strain for Gauge S14 on Specimen 1...68

Figure A-16: Moment vs. Strain for Gauge S1 on Specimen 2...69

Figure A-17: Moment vs. Strain for Gauge S2 on Specimen 2...69

Figure A-18: Moment vs. Strain for Gauge S3 on Specimen 2...70

Figure A-19: Moment vs. Strain for Gauge S4 on Specimen 2...70

Figure A-20: Moment vs. Strain for Gauge S5 on Specimen 2...71

Figure A-21: Moment vs. Strain for Gauge S7 on Specimen 2...71

Figure A-22: Moment vs. Strain for Gauge S6 on Specimen 2...72

Figure A-23: Moment vs. Strain for Gauge S8 on Specimen 2...72

Figure A-24: Moment vs. Strain for Gauge S9 on Specimen 2 73

Figure A-25: Moment vs. Strain for Gauge S10 on Specimen 2 73

Figure A-26: Moment vs. Strain for Gauge S11 on Specimen 2 74

Figure A-27: Moment vs. Strain for Gauge S12 on Specimen 2 74

Figure A-28: Moment vs. Strain for Gauge S1 on Specimen 3 75

Figure A-29: Moment vs. Strain for Gauge S2 on Specimen 3 75

Figure A-30: Moment vs. Strain for Gauge S3 on Specimen 3 76

Figure A-31: Moment vs. Strain for Gauge S4 on Specimen 3 76

Figure A-32: Moment vs. Strain for Gauge S5 on Specimen 3 77

Figure A-33: Moment vs. Strain for Gauge S7 on Specimen 3 77

Figure A-34: Moment vs. Strain for Gauge S6 on Specimen 3 78

Figure A-35: Moment vs. Strain for Gauge S8 on Specimen 3 78

Figure A-36: Moment vs. Strain for Gauge S9 on Specimen 3 79

Figure A-37: Moment vs. Strain for Gauge S10 on Specimen 3 79

Figure B-1: String Pots Used to Measure System Response, a) East-West Direction, b) North-South Direction 81

Figure B-2: Load vs. Displacement for SP1 on Specimen 1 82

Figure B-3: Load vs. Displacement for SP2 on Specimen 1 82

Figure B-4: Load vs. Displacement for SP3 on Specimen 1 83

Figure B-5: Load vs. Displacement for SP4 on Specimen 1 83

Figure B-6: Load vs. Displacement for SP6 on Specimen 1 84

Figure B-7: Load vs. Displacement for SP1 on Specimen 2 85

Figure B-8: Load vs. Displacement for SP2 on Specimen 2 85

Figure B-9: Load vs. Displacement for SP3 on Specimen 2 86

Figure B-10: Load vs. Displacement for SP4 on Specimen 2 86

Figure B-11: Load vs. Displacement for SP6 on Specimen 2 87

Figure B-12: Load vs. Displacement for SP1 on Specimen 3 88

Figure B-13: Load vs. Displacement for SP2 on Specimen 3 88

Figure B-14: Load vs. Displacement for SP3 on Specimen 3 89

Figure B-15: Load vs. Displacement for SP4 on Specimen 3 89

Figure B-16: Load vs. Displacement for SP5 on Specimen 3 90

Figure B-17: Load vs. Displacement for SP6 on Specimen 3 90

Figure E-1: Integration of Cylindrical Wedge, a) Top View, b) Side View.................................95

1 INTRODUCTION

1.1 Common Uses for Deep Foundations

Piles are often used to resist vertical and lateral loads when shallow foundations are inadequate or uneconomical. Buildings, for example, may use a pile foundation rather than spread footings when the soil bearing strength is inadequate or the predicted settlement is too large. Piles resist vertical loads through end bearing as well as skin friction along the exterior of the pile. In addition to supporting vertical loads, piles may help mitigate the effects of soft or expansive soils (Das 2011). Piles may also resist lateral loads. The lateral load capacity depends on soil properties, pile embedment into the soil, and the pile-to-cap connection (Budhu 2007). This thesis focuses on pile-to-cap connections.

1.2 Fixed vs. Pinned Connections

Pile-to-cap connections are generally considered either pinned or fixed. A pinned connection may be assumed if the piles are primarily used to resist vertical loads and uplift is not a concern. These connections typically have limited or no reinforcement between the pile and the cap. For lateral loads, a fixed pile-to-cap connection may be selected in order to minimize deflections in soft soils. It has been shown through testing on cast-in-steel-shell piles (Silva and Seible 2001) and prestressed concrete piles (Sheppard 1983) that a fixed pile-to-cap connection can be accomplished by extending reinforcement from the pile into the cap. Although a fixed pile-to-cap connection can be created using reinforcement, sufficient pile embedment depth without reinforcement may produce similar results (Richards et al. 2011) and be more cost effective. Different methods have been developed to compute the capacity of steel members embedded in concrete. These methods are commonly extended to compute the capacity of pile-to-cap connections.

Pile-to-cap connections can be compared to the connection of an embedded column in concrete. Both the pile-to-cap connection and the connection of an embedded column must be designed for lateral and vertical loads. However, embedded columns typically need to resist greater lateral loads at the connection than pile-to-cap connections. As a result, embedded columns will typically require a greater embedment depth. In addition, embedded columns will use shear studs on the column in order to resist uplift while reinforcement is more commonly used to resist uplift in a pile-to-cap connection (Pertold et al. 2000).

1.3 Significance of Strength and Stiffness

In the next chapter, it will be demonstrated that present methods for computing the strength and stiffness of embedded pile-to-cap connections are not precise. A better understanding of the strength and stiffness of pile-to-cap connections will lead to better analyses and more realistic design. This in turn can lead to safe yet cost effective solutions. When using programs such as LPILE to determine pile demands and deflections, the results of the analyses are sensitive to the assumptions made about the pile-to-cap connection strength and stiffness. A more complete understanding of the strength of pile-to-cap connections will lead to more accurate models.

A better understanding of the strength and stiffness of pile-to-cap connections may also lead to a more economical design and less or no reinforcement between the pile and the cap. As the strength of the connection is more accurately determined, the required pile embedment into the cap may be reduced. As a result, the connection will become more economical. A better understanding of the stiffness of the connection may also lead to a more economical design as fixed connections may be able to rely on embedment alone. If sufficient embedment is able to provide adequate stiffness for a fixed connection, then the intricate reinforcement between the pile and the cap may be eliminated.

1.4 Outline

This chapter has discussed background and motivation for the present work. Chapter two provides additional background from the literature. Chapter three describes laboratory testing that was performed to better understand the stiffness and strength of embedded pile-to-cap connections. This testing consisted of three pile-to-cap connections tested to failure in an inverted position. Chapters four through six present and discuss the test results.

2 LITERATURE REVIEW

2.1 Methods for Computing Connection Capacity

One method for computing the capacity of embedded steel members was presented in the first edition of the PCI Design Handbook (Prestressed Concrete Institute 1971). This method assumed an embedment mechanism acting about a constant neutral axis. Figure 2-1 shows the assumed stress distribution.

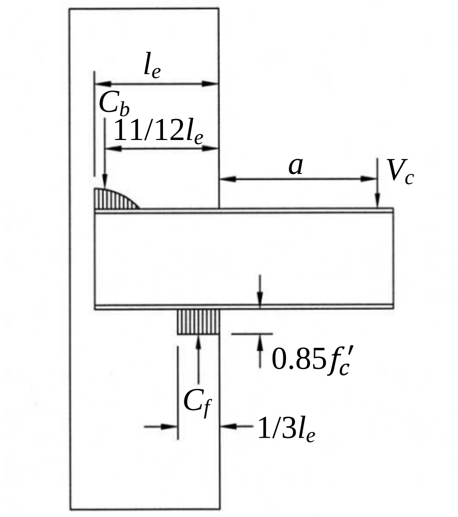

Figure 2-1: Stress Distribution for Original PCI Equation (Marcakis 1979)

The compression force C_f at the opposite side of the applied load (front of the connection) is given by equation 2-1.

$$C_f = 0.85 f_c' b \frac{l_e}{3} \tag{2-1}$$

where:
f_c' = compressive strength of concrete, kPa
b = width of embedded member, m
l_e = embedment depth, m (see Figure 2-1)

The force, C_f, is based on the assumption of a rectangular stress block and a maximum useable concrete compressive strength equal to 85 percent of f_c'. The stress distribution acts on an effective width of the steel member and 1/3 the embedment depth.

The compressive stress distribution on the same side as the applied load (back of connection) is assumed to have a parabolic shape with a resultant force, C_b, located at 11/12 of the embedment depth.

The maximum shear force, V_c, which is limited by the moment capacity of the connection, is determined by summing the moments about the location of the resultant compressive force at the back of the connection. This is given by equation 2-2.

$$V_c \left(a + \frac{11}{12} l_e\right) = C_f \left(\frac{3}{4} l_e\right) \tag{2-2}$$

The shear span of the pile, a, is the distance from the point of application of the load to the face of the concrete (see Figure 2-1)

The maximum shear force can then be determined in terms of the compressive force, C_f, given by equation 2-3.

$$V_c = \frac{3C_f}{3.67 + 4\frac{a}{l_e}} \tag{2-3}$$

Substituting the compressive force, C_f, given by equation 2-1 into equation 2-3 produces equation 2-4.

$$V_c = \frac{0.85 f_c' b l_e}{3.67 + 4\frac{a}{l_e}} \qquad (2\text{-}4)$$

Equation 2-4 is the equation in the original PCI Design Handbook used to calculate the capacity of embedded steel members.

In 1980, Marcakis and Mitchell proposed a different equation that appears in later editions of the PCI Design Handbook. This maximum shear force is given by equation 2-5.

$$V_c = \frac{0.85 f_c' b l_e}{1 + 3.6\frac{e}{l_e}} \qquad (2\text{-}5)$$

where:
b = effective width of compression block, m
$e = a + \frac{l_e}{2}$, m

The two differences between equations 2-4 and 2-5 are the factors in the denominator and the width of the compression block. The factors in equation 2-4 come from the assumed locations of the reactions, while the factors in equation 2-5 have been calibrated using experimental data. In equation 2-4, the width of the compression block was the width of the embedded member, but in equation 2-5 the width of the compression block is defined as an "effective width" which is larger than the width of the member (Marcakis and Mitchell 1980). Both the equation from the original PCI Design Handbook and the equation presented by Marcakis and Mitchell are plotted in Figure 2-2 with the data shown in the paper.

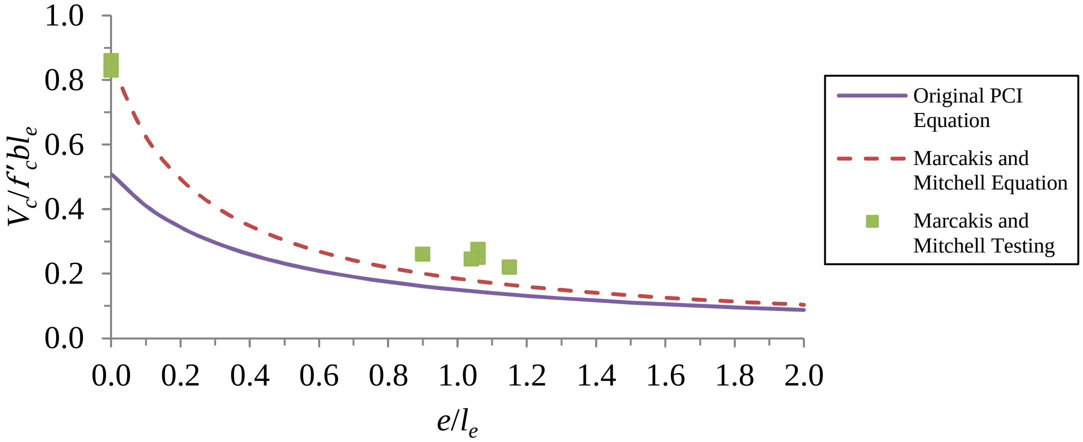

Figure 2-2: Capacity vs. Embedment Using Marcakis and Mitchell and Original PCI Design Handbook Equation for Pipes [Based on Figure 7 in (Marcakis and Mitchell 1980)]

2.2 The Marcakis and Mitchell Equation

The testing that was performed to calibrate equation 2-5 consisted of 25 corbel specimens with varying member embedment, shear span, shape of member, and axial load. The set-up used to test these specimens is shown in Figure 2-3. The embedment of the members varied from 0.10 to 0.20 m (4 to 8 in) in depth with a shear span varying from 0.08 to 0.20 m (3 to 8 in). The shapes of the steel members were primarily HSS6×4×3/8. Other shapes tested included HSS4×4×1/4, W6×25, 0.10 m (4 in) square bar, and 0.2×0.10 m (3/4×4 in) plate. An axial load ranging from 134 to 1450 kN (30 to 326 kips) was applied to the column on 7 of the specimens as shown in Figure 2-3.

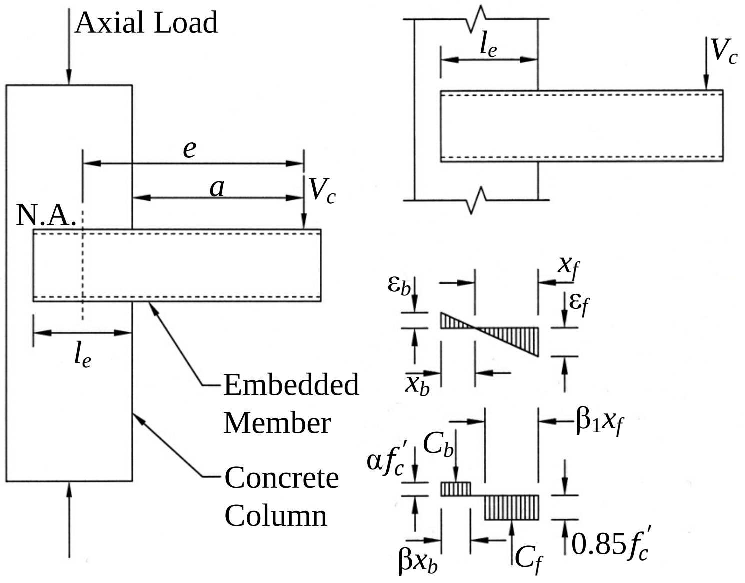
Axial Load
e
a
V_c
N.A.
l_e
Embedded Member
Concrete Column
l_e
V_c
x_f
ε_b
ε_f
x_b
$\beta_1 x_f$
$\alpha f_c'$
C_b
βx_b
C_f
$0.85f_c'$

(a) (b)

Figure 2-3: Marcakis and Mitchell Model, a) Set-up for Testing, b) Stresses and Strains

The stress-strain relationship for the model used by Marcakis and Mitchell is also shown in Figure 2-3. Like the model for equation 2-4, this model also assumes a maximum strain of 0.003 at the front of the connection, ε_f, as well as an equivalent stress block of 85 percent the concrete compressive strength. The model used by Marcakis and Mitchell, however, assumes that the location of the neutral axis depends on the loading conditions. As a result, the strain at the back of the member must be determined using an iterative procedure.

The first step in this iterative procedure is to assume a depth to the neutral axis, x_f. The strain at the back of the embedded member can be determined using equation 2-6.

$$\varepsilon_b = \frac{\varepsilon_f x_b}{x_f} \tag{2-6}$$

Once the strain at the back of the connection has been determined, the corresponding stress block factors, β and α, can then be calculated using equations 2-7 and 2-8, respectively. The strain at the maximum concrete stress, ε_o, is assumed to be 0.002 in each of these equations.

$$\beta = \frac{4 - \frac{\varepsilon}{\varepsilon_o}}{6 - 2\frac{\varepsilon}{\varepsilon_o}} \tag{2-7}$$

$$\alpha\beta = \frac{\varepsilon}{\varepsilon_o} - \frac{1}{3}\left(\frac{\varepsilon}{\varepsilon_o}\right)^2 \tag{2-8}$$

Since an equivalent stress block factor of 85 percent of the concrete compressive strength is used at the front of the connection, the depth of the stress block is defined as β_1 (American Concrete Institute 2008). This factor can be calculated using equation 2-9.

$$\beta_1 = 0.85 - 0.08\left(\frac{f_c' - 30}{10}\right) \geq 0.65;\ \beta_1 = 0.85 \text{ for } f_c' \leq 30 \text{ MPa} \tag{2-9}$$

Using the stress block factors α, β, and β_1 the magnitudes of the stress resultants C_f and C_b can then be determined using equations 2-10 and 2-11, respectively.

$$C_f = 0.85 f_c' \beta_1 x_f b \tag{2-10}$$

$$C_b = \alpha f_c' b \beta x_b \tag{2-11}$$

Once the stress resultants have been calculated, the maximum shear force of the connection can be determined using force equilibrium given by equation 2-12.

$$V_c = C_f - C_b \tag{2-12}$$

The final step in the procedure is to calculate the corresponding value of e using moment equilibrium about the center of the embedment given by equation 2-13.

$$V_c e = C_f\left(\frac{l_e}{2} - \beta_1 \frac{x_f}{2}\right) + C_b\left(\frac{l_e}{2} - \beta \frac{x_b}{2}\right) \tag{2-13}$$

If this procedure is repeated several times, varying the depth to the neutral axis, the normalized maximum shear force can then be plotted against the variable e normalized by the embedment depth. Figure 2-4 shows the results obtained from performing this iterative procedure using values between 0.24 m (9.5 in) and 0.46 m (18 in) for x_f and a concrete compressive strength of 27.6 MPa (4.0 ksi). The equation presented by Marcakis and Mitchell is also shown in the figure. Equation 2-5 has been calibrated to fit the points obtained from the procedure just described.

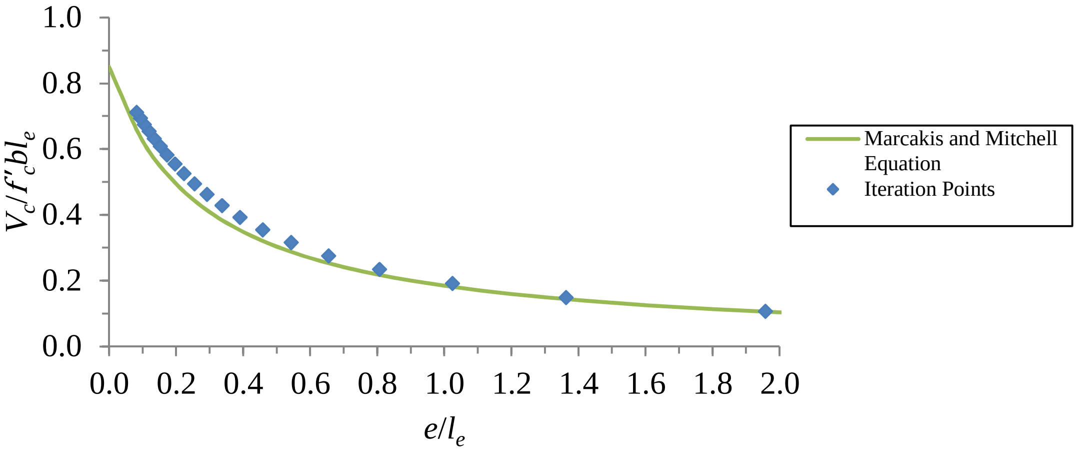

Figure 2-4: Points from Iterative Procedure Compared with Marcakis and Mitchell Equation

Markacis and Mitchell indicate that when the width of the embedded member is used, the calculated maximum shear force is significantly lower than the actual maximum shear force of the connection. This was believed to be due to the added strength of the confined concrete. They claimed that the load was able to spread to a width greater than the width of the embedded member. As a result, for situations where the width of the confined concrete is much larger than the width of the embedded steel member, it was suggested that the compression block may be increased up to 2.5 times the width of the embedded steel member. This amplification is limited to this factor in order to maintain the same safety margin as smaller connections. This is called an effective width (Marcakis and Mitchell 1980).

2.3 Unexplained Strength of Pile-to-Cap Connections

Since the 1980's, when Marcakis and Mitchell's equation was proposed, some experiments have shown that the maximum shear force of embedded connections is significantly greater than what equation 2-5 predicts.

Xiao researched the ability of precast, prestressed concrete pile-to-cap connections with shallow embedment to resist moment. Two identical pile-to-cap specimens were tested with a single 0.36 m (14.0 in) square pile and a shear span of 1.3 m (52 in) as shown in Figure 2-5. Each pile was embedded 7.5 cm (2.95 in) with four dowel bars extending into the cap. The specimens were tested with cyclic lateral loading and constant axial loading. The axial loading of 1780 kN (400 kip) and 890 kN (200 kip) was the only difference between the two tests. Using equation 2-5 above, the moment capacity of each of the two specimens due to the embedment of the pile into the cap was 46.0 kN-m (33.9 kip-ft). Note that the computed moment capacity using equation 2-5 does not account for axial load. The moment capacity due to the flexural resisting mechanism of the specimen with the larger axial load was 220 kN-m (163 kip-ft) resulting in a total calculated moment capacity of 266 kN-m (196 kip-ft). The measured strength of the specimen was 396 kN-m (292 kip-ft), which was 1.5 times larger than the calculated moment capacity. The moment capacity due to the flexural resisting mechanism of the specimen with the smaller axial load was 175 kN-m (129 kip-ft) resulting in a total calculated moment capacity of 221 kN-m (163 kip-ft). The measured strength of the specimen was 264 kN-m (195 kip-ft), which was 1.2 times larger than the calculated moment capacity. Both specimens from this testing reported larger capacities than were predicted (Xiao 2003).

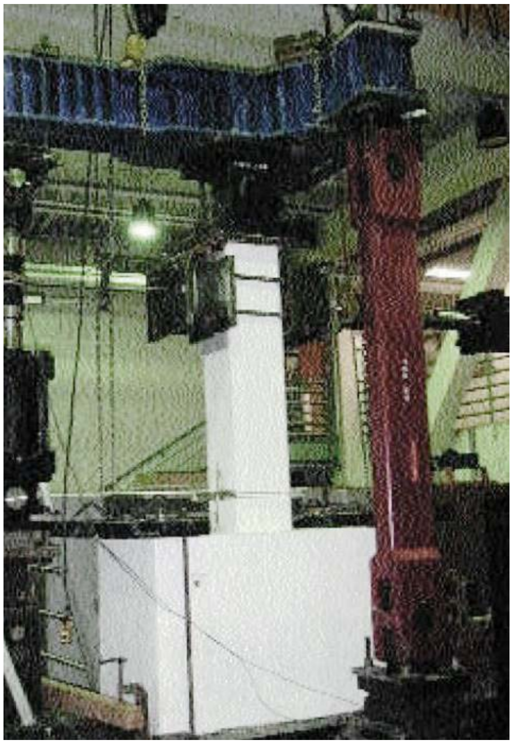

Figure 2-5: Test Set-up for Testing by Xiao [(Xiao 2003), used without permission]

Rollins and Stenlund performed testing on the connection between driven pipe piles and concrete caps. One specimen that was tested had two 0.32 m (12.75 in) diameter piles embedded 0.15 m (6.0 in) into the concrete cap with reinforcement between the piles and the cap. The results from this test were interesting because the leading pile reached a moment of 260 kN-m (192 kip-ft) while the calculated moment capacity using equation 2-5 was only 100 kN-m (74 kip-ft). Including the concrete cover in the embedment length increased the moment capacity to 185 kN-m (137 kip-ft). However, the measured moment capacity of the connection was still 1.4 times the largest calculated moment capacity. Since the leading pile-to-cap connection did not reach failure, the actual moment capacity was unknown (Richards et al. 2011).

Richards et al. suggested two mechanisms that may explain the additional moment capacity observed in the testing. The first was dowel action from two of the grid bars that passed through holes in the piles. Since the holes in the piles were relatively large compared to the bars, this mechanism was not considered in preliminary calculations. This mechanism could not account for all the moment capacity. The second mechanism that was considered was friction between the pile and the concrete. This mechanism may account for the increased moment capacity, however, additional testing is required to verify this mechanism (Richards et al. 2011).

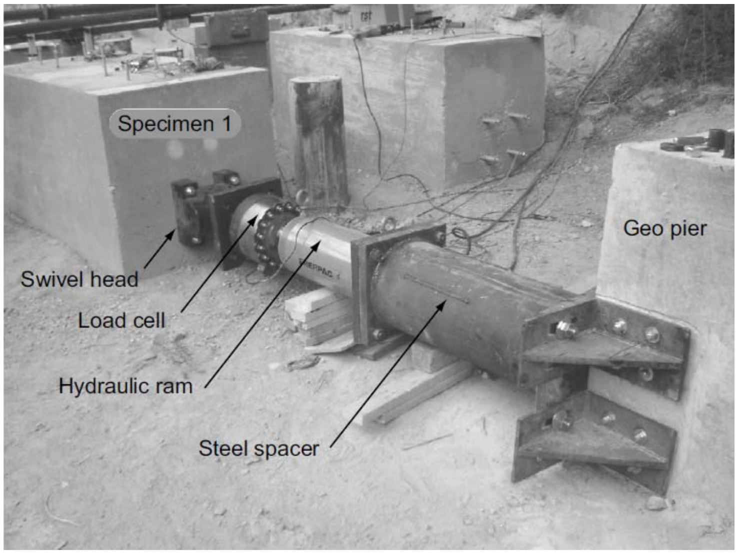
Specimen 1
Geo pier
Swivel head
Load cell
Hydraulic ram
Steel spacer

Figure 2-6: Test Set-up for Testing by Rollins and Stenlund [(Richards et al. 2011) used without permission]

3 TESTING AND INSTRUMENTATION

The pile-to-cap specimens used in the study each consisted of a cap with a single pile. The cap for each specimen was 0.91×0.91×1.52 m (3×3×5 ft) with reinforcement as shown in Figure 3-1. The design strength of the concrete was 27.6 MPa (4 ksi). Both the compressive strength at 28-days and on the day of testing for each cap is shown in Table 3-1. The piles were standard 0.32 m (12.75 in) diameter pipe piles that extended approximately 1.52 m (5.0 ft) out of the cap, and had varying pile embedment depths. All of the piles were hollow with a steel cover plate welded to the embedded end; there was no reinforcement between the piles and the caps. The nominal yield strength of the piles was 310 MPa (45 ksi) and the nominal ultimate strength of the piles was 455 MPa (66 ksi) (ASTM International 2010). The measured material strengths of the piles were substantially greater and are shown in Table 3-2. The pile embedment depths for Specimens 1, 2, and 3 were 0.45 m (17.9 in), 0.16 m (6.25 in), and 0.12 m (4.56 in), respectively.

The test set-up is illustrated in Figure 3-2. Loads were applied to each specimen using an actuator mounted on a reaction frame. The actuator, capable of inducing 445 kN (100 kips), was positioned 1.52 m (5.0 ft) above the pile-to-cap connection. This load location corresponds to the approximate inflection point locations of similar piles from a field study (Richards et al. 2011). Uplift of the specimen was resisted by two W12×72 hold-down beams that extended over the cap and were post-tensioned to the floor. Bearing plates were used between the hold-down beams and the cap. Additional restraint beams were post-tensioned to the floor to prevent the cap from moving in each direction.

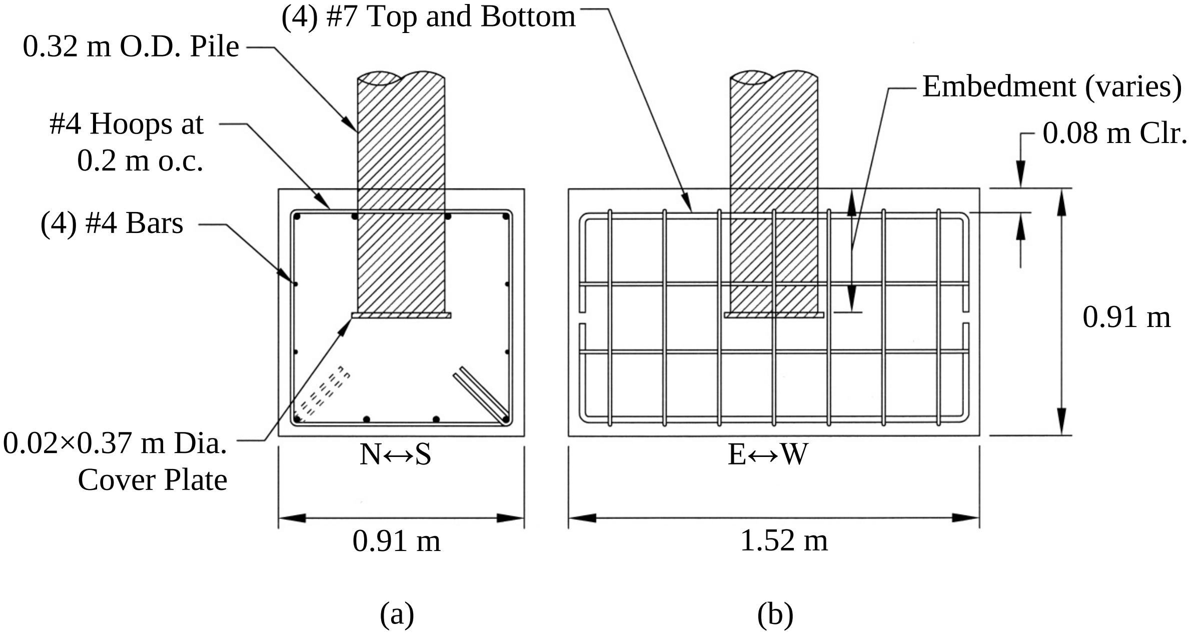
(4) #7 Top and Bottom
0.32 m O.D. Pile
#4 Hoops at 0.2 m o.c.
(4) #4 Bars
0.02×0.37 m Dia. Cover Plate
N↔S
0.91 m
Embedment (varies)
0.08 m Clr.
0.91 m
E↔W
1.52 m
(a)
(b)

Figure 3-1: Pile-to-Cap Connection Design, a) End View, b) Side View

Table 3-1: Compressive Strengths of Concrete for Each Specimen

Specimen	f_c' 28-day, MPa[a]	f_c' day of test, MPa[a]
1	28.1	27.3
2	28.1	31.9
3	28.1	32.6

a. Results shown are the average of two cylinders

Table 3-2: Tensile Strength of Piles Used in Testing

Sample	f_y, MPa	f_u, MPa
1	386.1	457.1
2	393.7	463.3

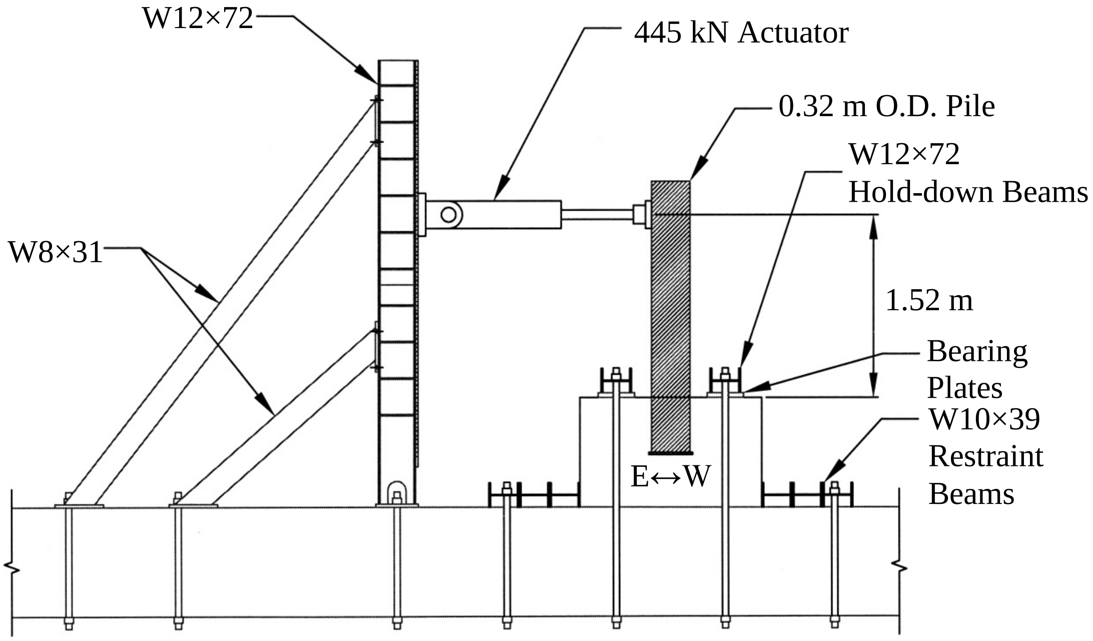

Figure 3-2: Reaction Frame and Beams Used to Resist Loads

Various string pots and strain gages measured the response of each specimen. Two string pots were used to measure the response in each plan direction at the load point as well as at the mid-height of the pile as shown in Figure 3-3. The string pots at the mid-height of the pile were located approximately 0.42 m (1.4 ft) above the cap. The displacement of the cap was also measured using string pots in either direction. In order to measure activity inside the cap, four strain gages were installed on the longitudinal reinforcement for each specimen. These gages were labeled S1 through S4. The gages on the reinforcement were placed on two bars on either side of the pile as shown in Figure 3-4. In addition to gages inside the cap, gages were also used to measure the response of the pile. Four strain gages were installed on the exterior of the pile at approximately 2.54 cm (1.0 in) above the concrete surface for each specimen. These gages were labeled S5 through S8. Six, four, and two additional gages were placed on the interior of the pile for Specimens 1, 2, and 3 respectively as shown in Figure 3-4. For Specimen 1 these gages were labeled S9 through S14, for Specimen 2 these gages were labeled S9 through S12, and for Specimen 3 these gages were labeled S9 and S10.

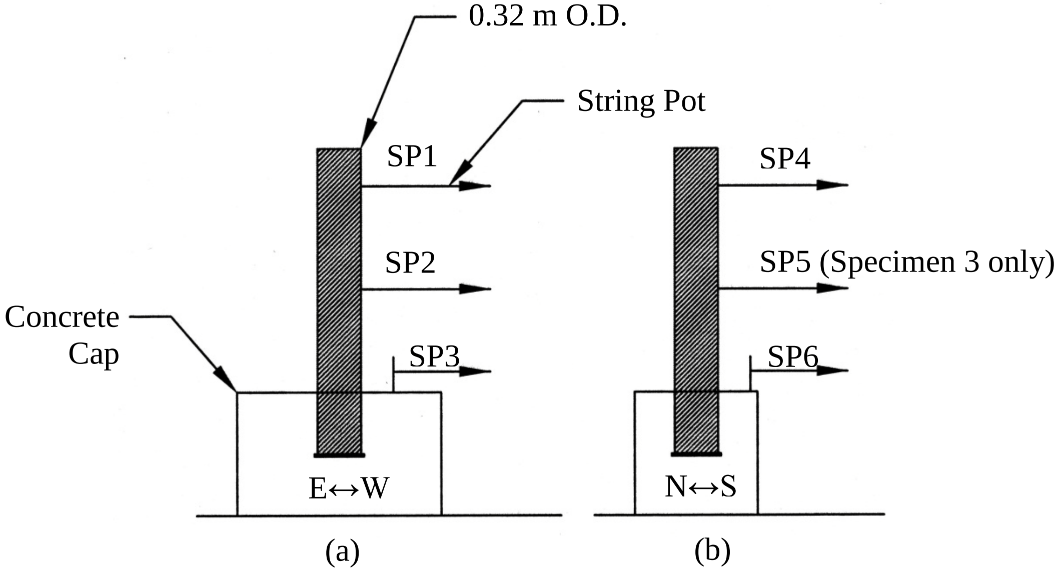
0.32 m O.D.
String Pot
SP1
SP2
SP3
SP4
SP5 (Specimen 3 only)
SP6
Concrete Cap
E↔W
N↔S
(a)
(b)

Figure 3-3: String Pots Used to Measure System Response, a) East-West, b) North-South

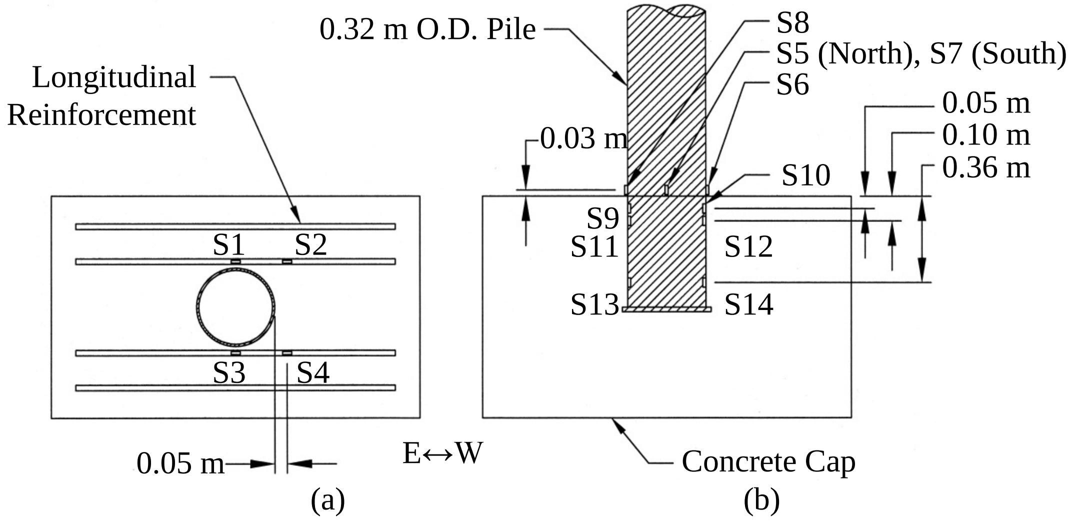
0.32 m O.D. Pile
Longitudinal Reinforcement
S1
S2
S3
S4
0.05 m
E↔W
(a)
S8
S5 (North), S7 (South)
S6
0.05 m
0.10 m
0.36 m
0.03 m
S10
S9
S11
S12
S13
S14
Concrete Cap
(b)

Figure 3-4: Strain Gages Used to Measure System Response, a) Plan View, b) Side View

Both force-controlled and displacement-controlled protocols were used in testing. A force-controlled protocol was used on Specimen 1 because the stiffness of the set-up was not precisely known. Once the stiffness of the set-up was better understood, a displacement-controlled protocol was used for Specimens 2 and 3. The force-controlled protocol was 36, 71, 107, and 142 kN (8, 16, 24, and 32 kips) with five cycles at each load. Loads of 214 and 249 kN (48 and 56 kips) were then reached with two cycles each. The final cycles went up to 285 kN (64 kips) until failure was reached. The load rate for this protocol was 1.8 kN (0.4 kips) per second. The displacement-controlled protocol went from 0.38 cm (0.15 in) to 1.52 cm (0.60 in) in increments of 0.38 cm (0.15 in) with five cycles at each displacement. The load rate for this protocol was 1.27 cm (0.5 in) per minute.

4 TESTING RESULTS

4.1 Specimen 1

Specimen 1, with a pile embedment depth of 1.5 pile diameters [0.45 m (17.9 in)], had sufficient connection capacity for the pile to yield. The first noticeable change in the specimen due to loading was a gap that appeared between the pile and the concrete. This occurred at a lateral load of approximately 107 kN (24 kips). This gap grew throughout the test and is shown in Figure 4-1 when the load was 249 kN (56 kips) and when the displacement was 5.3 cm (2.1 in). Shortly after the gap first became apparent, a hairline crack appeared at 142 kN (32 kips) that extended from the pile down the side of the cap as shown in Figure 4-2. As testing approached the ultimate load, additional cracks appeared, progressing outward from the pile in various directions as shown in Figure 4-3. After an ultimate lateral load of 255 kN (57.4 kips) was reached, a significant vertical crack appeared on the end of the cap as shown in Figure 4-4. The corresponding ultimate moment of the pile-to-cap connection was 391 kN-m (288 kip-ft). Using the properties of the pile, the yield and plastic moments of the pile were calculated to be 280 kN-m (207 kip-ft) and 373 kN-m (275 kip-ft) respectively. Since the ultimate moment exceeded the yield and plastic moments, the strength of the connection was sufficient to both yield the pile and permit strain hardening to occur.

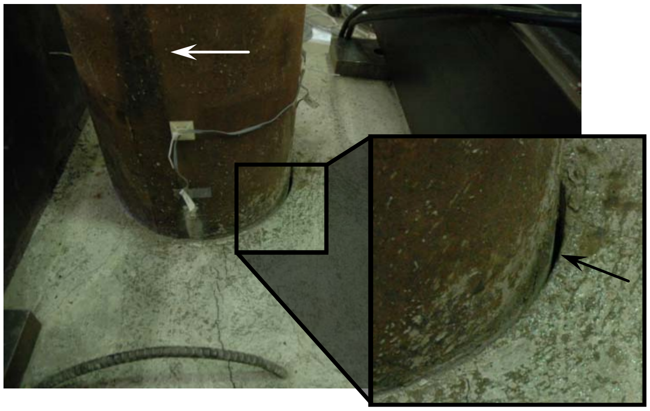

Figure 4-1: Gap in Specimen 1 [249 kN (56 kips), 5.3 cm (2.1 in)]

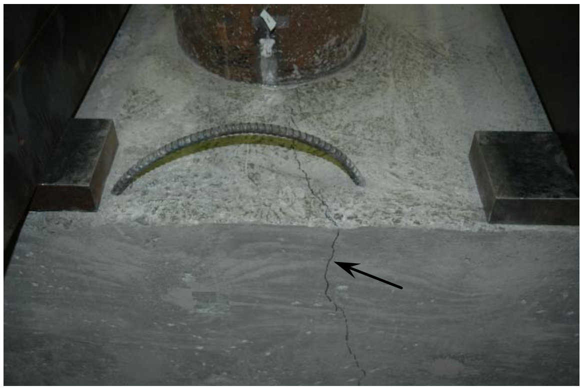

Figure 4-2: Initial Cracking in Specimen 1 (East-West)

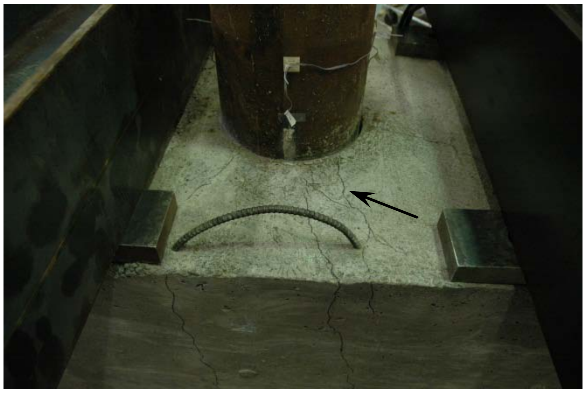

Figure 4-3: Specimen 1 at Maximum Displacement (East-West)

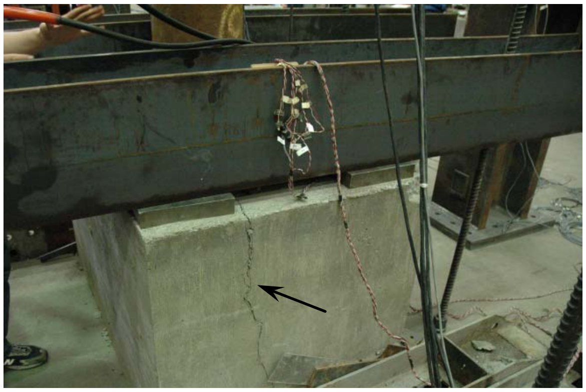

Figure 4-4: End of Cap of Specimen 1 After Testing (North-South)

4.2 Specimen 2

Specimen 2, with a pile embedment depth of one-half a pile diameter [0.16 m (6.25 in)], did not have sufficient capacity to permit the pile to yield. A gap between the pile and the concrete was also the first observable load effect in the cap. It was noticed much earlier than Specimen 1 at approximately 39 kN (8.7 kips). This gap grew throughout the test and is shown in Figure 4-5 when the load was 49.3 kN (11.1 kips) and when the displacement was 4.3 cm (1.7 in). Shortly after the gap first appeared, cracking on the top surface of the cap became visible at 61 kN (13.7 kips) as shown in Figure 4-6. After an ultimate lateral load of 66.3 kN (14.9 kips) and a corresponding ultimate moment of 102 kN-m (75.3 kip-ft) were reached, the top surface of the cap on the side of the pile began peeling up creating a crack parallel to the direction of loading as shown in Figure 4-7. Cracking also appeared at the end of the cap toward the end of testing as shown in Figure 4-8. A final gap of 0.95 cm (0.38 in) was measured between the pile and the concrete.

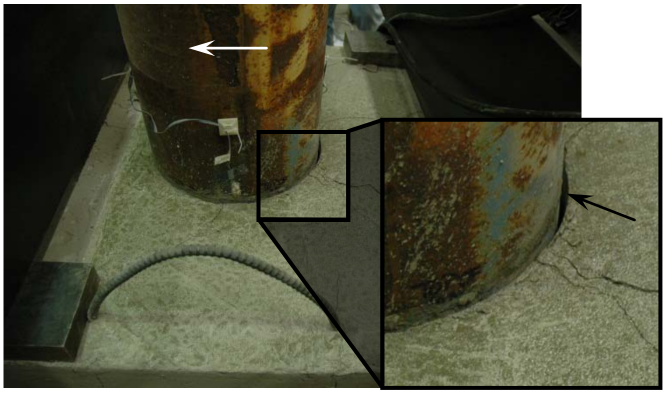

Figure 4-5: Gap in Specimen 2 [49.3 kN (11.1 kips), 4.3 cm (1.7 in)]

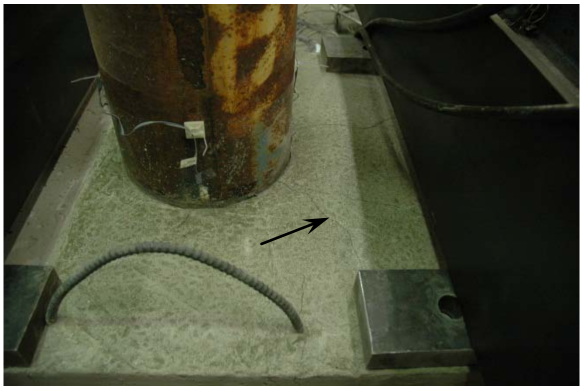

Figure 4-6: Initial Cracking of Specimen 2 (East-West)

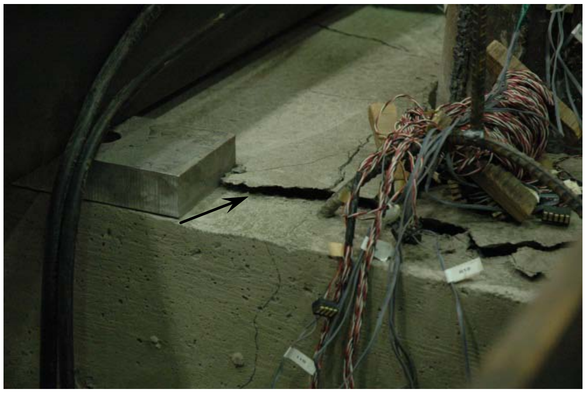

Figure 4-7: Peeling up of Concrete on the Top of Specimen 2 (East-West)

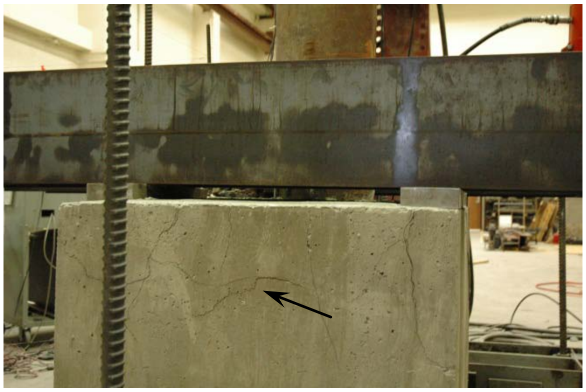

Figure 4-8: Cracking at the End of Specimen 2 After Testing (North-South)

4.3 Specimen 3

Specimen 3, with the least pile embedment depth (0.4 pile diameters) [0.12 m (4.56 in)], had the least capacity. A gap between the pile and the concrete became apparent earlier than either of the other two specimens at 17.3 kN (3.9 kips). This gap grew throughout the test and is shown in Figure 4-9 when the load was 6.2 kN (1.4 kips) and when the displacement was 6.0 cm (2.3 in). Hairline cracks appeared shortly after the gap first appeared at 29.8 kN (6.7 kips) as shown in Figure 4-10. Toward the end of testing, after an ultimate lateral load of 34.7 kN (7.8 kips) and a corresponding ultimate moment of 53.6 kN-m (39.5 kip-ft) were reached, significant cracks appeared at the end of the cap as shown in Figure 4-11. After testing was complete, various cracks were apparent in all directions on the top of the cap as shown in Figure 4-12. A final gap of 0.79 cm (0.31 in) was measured between the pile and the concrete. This pile-to-cap connection had insufficient capacity to allow the pile to yield.

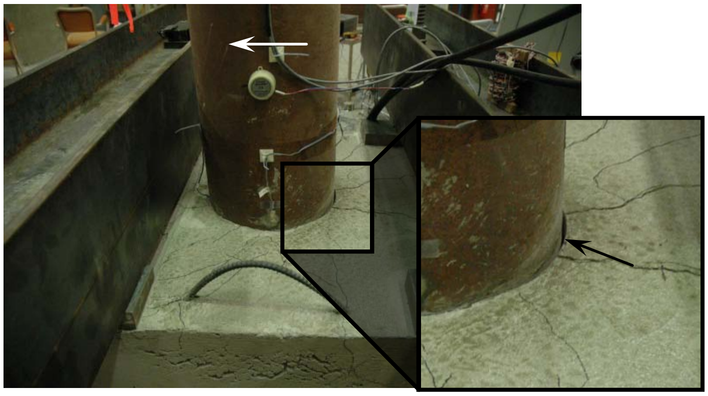

Figure 4-9: Gap in Specimen 3 [6.2 kN (1.4 kips), 6.0 cm (2.3 in)]

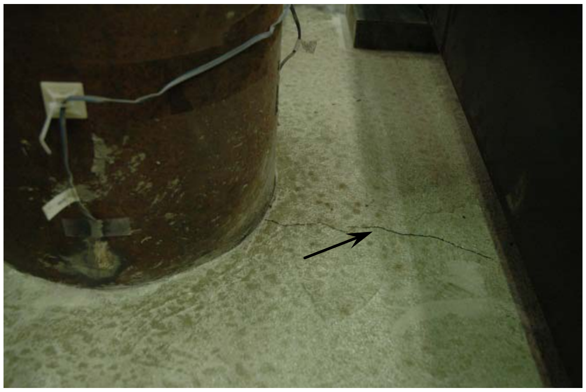

Figure 4-10: Initial Cracking of Specimen 3 (East-West)

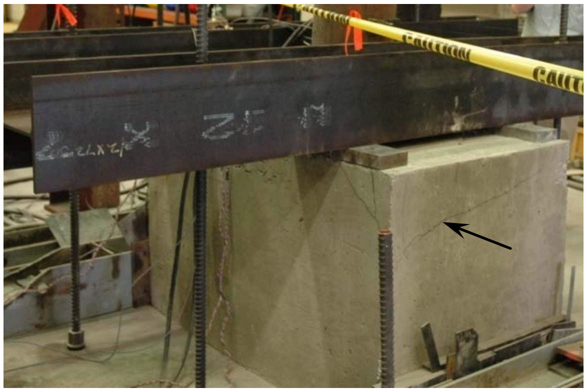

Figure 4-11: Cracking at the End of Specimen 3 (North-South)

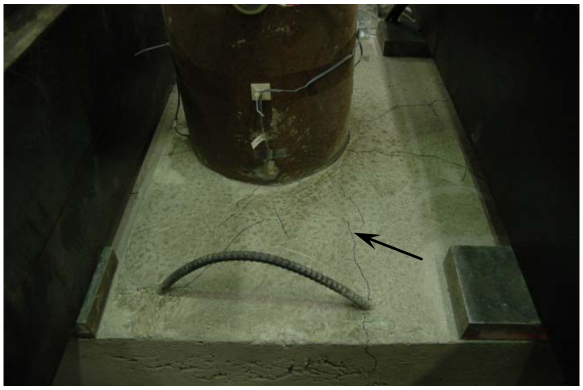

Figure 4-12: Specimen 3 After Testing (East-West)

4.4 Main Results

The response of each specimen to the loading is shown in Figure 4-13. In this figure, the lateral load is plotted against the deflection at the load-point of the pile. The ultimate lateral load for each specimen is also shown in the figure and is reported as 255 kN (57 kip), 66 kN (15 kip), and 35 kN (8 kip) for Specimens 1, 2, and 3, respectively.

Figure 4-14 shows the lateral load versus the deflection at the load-point of the pile for each specimen. For Specimen 1, the loads plotted in the figure are the peak loads from the first cycle in each load increment during testing. For Specimens 2 and 3, the loads that are plotted in the figure are the peak loads from the first cycle in each displacement increment during testing since they were tested using a displacement-controlled protocol. The maximum elastic load for each specimen is also shown in the figure. This maximum elastic load is defined as the lateral load at which the stiffness of the specimen appears to change significantly.

The strain in the pile at various depths of the connection is compared with its location in Figure 4-15. These strains are from the strain gages on the east and west sides of the pile and are reported at the maximum elastic load for each specimen. The maximum elastic load was measured when the pile was pushed toward the east causing the east side to be more compressive and the west side to be more tensile. Lines are shown connecting the strain gages at each elevation to aid in comparing paired strain gages. These lines, however, do not imply a linear relationship in the strains between the strain gages.

Figure 4-16 plots the same data as Figure 4-15, but shows the pile strain plotted versus depth.

Figure 4-17 and Figure 4-18 are similar to Figure 4-15 and Figure 4-16, but strains are shown at the time when the ultimate strength was achieved rather than the maximum elastic strength.

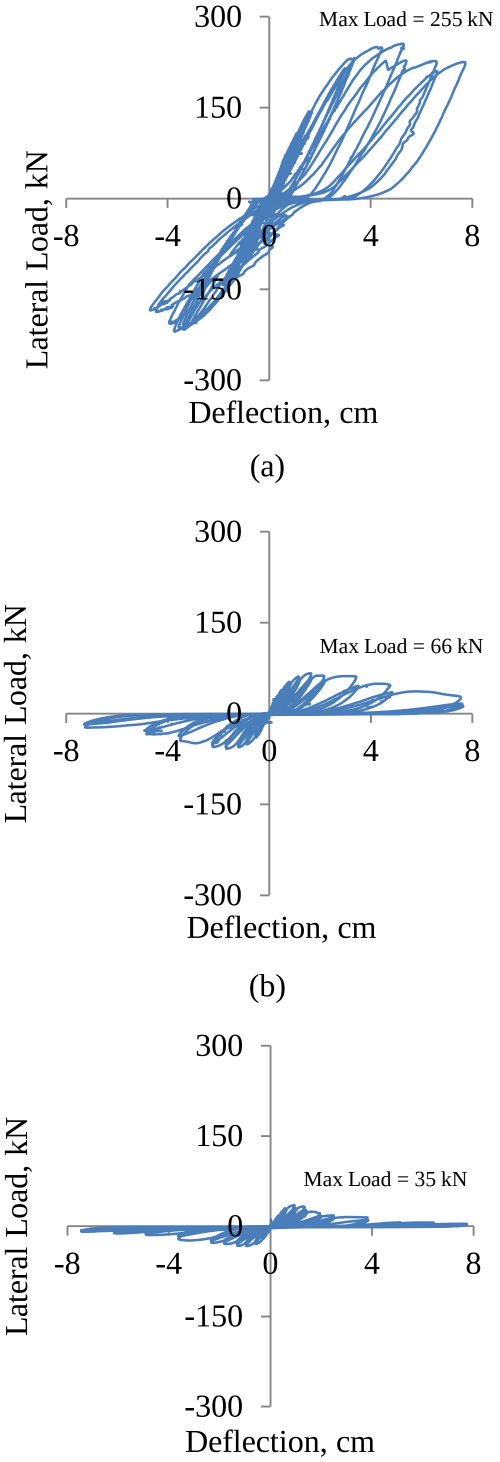

(a)

(b)

(c)

Figure 4-13: Lateral Load vs. Deflection, a) Specimen 1, b) Specimen 2, c) Specimen 3

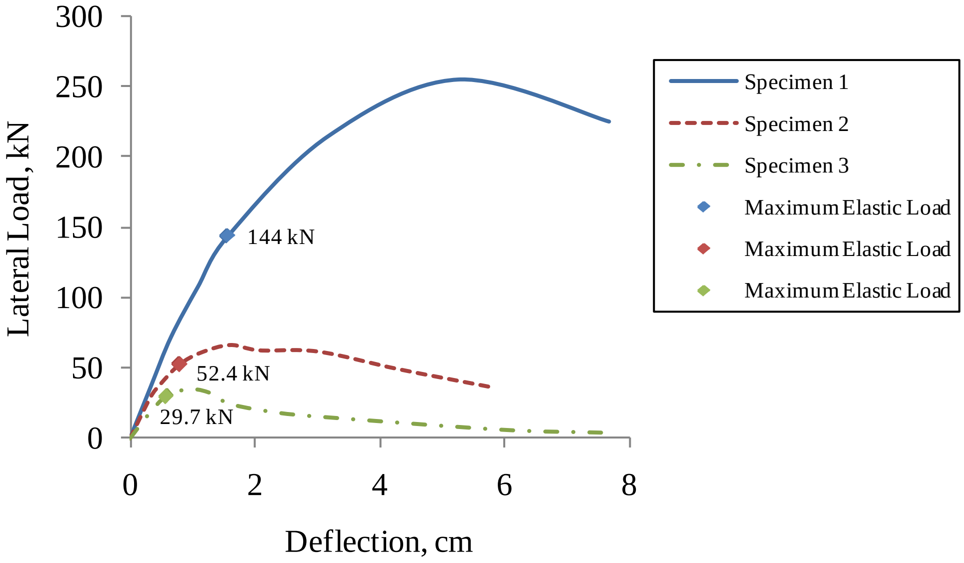

Figure 4-14: Lateral Load vs. Deflection of Pile

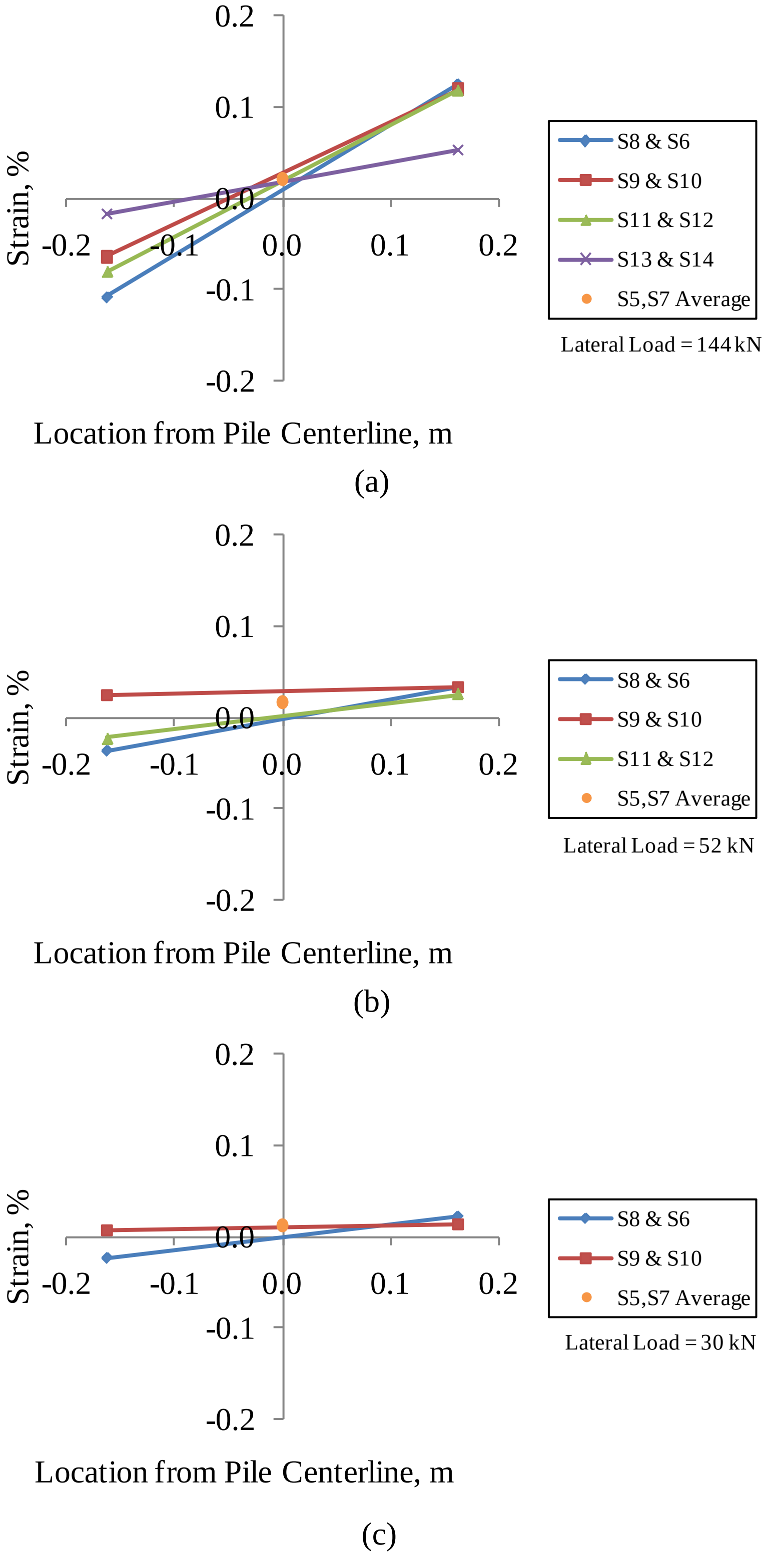

Figure 4-15: Strain vs. Location at Maximum Elastic Load, a) Specimen 1, b) Specimen 2, c) Specimen 3

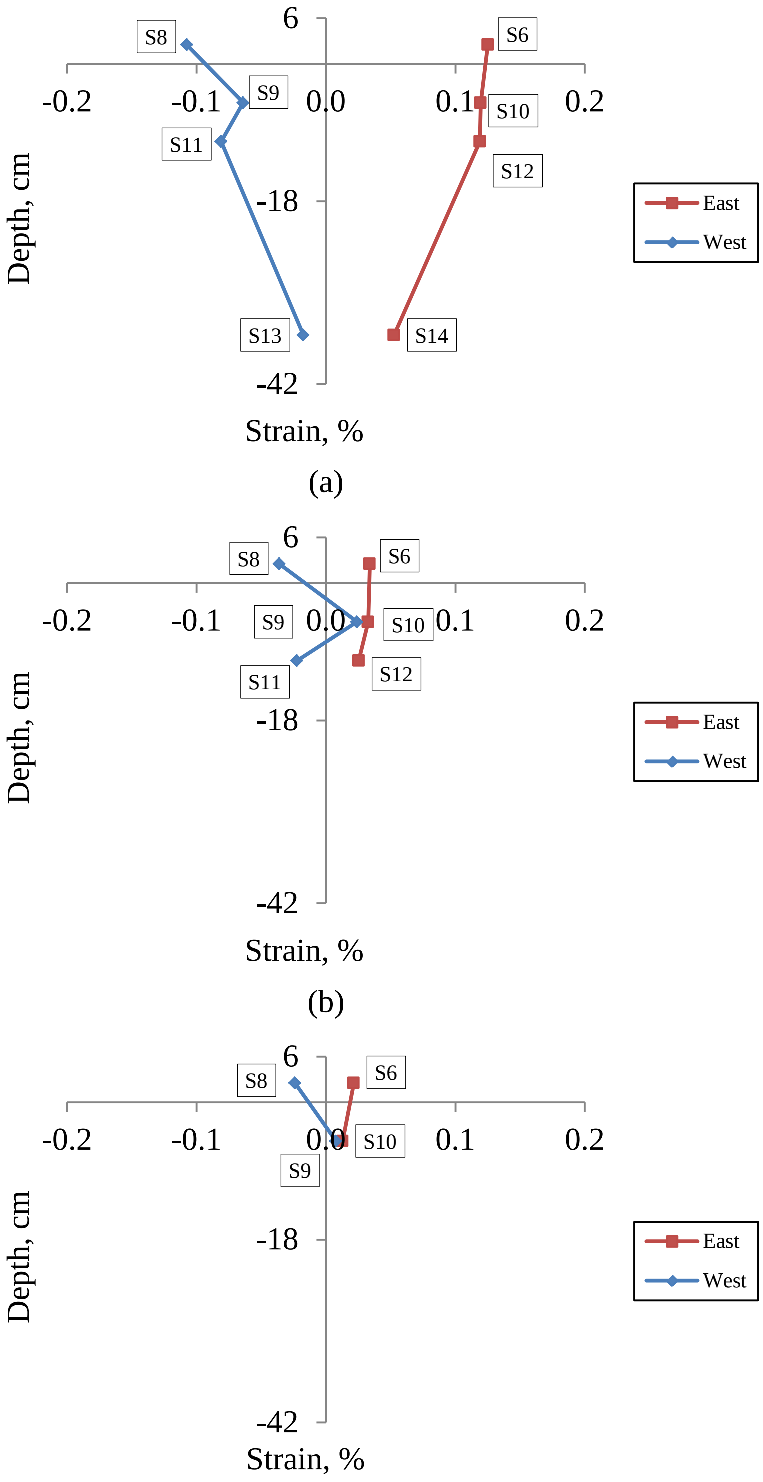

(a)

(b)

(c)

Figure 4-16: Strain vs. Depth at Maximum Elastic Load, a) Specimen 1, b) Specimen 2, c) Specimen 3

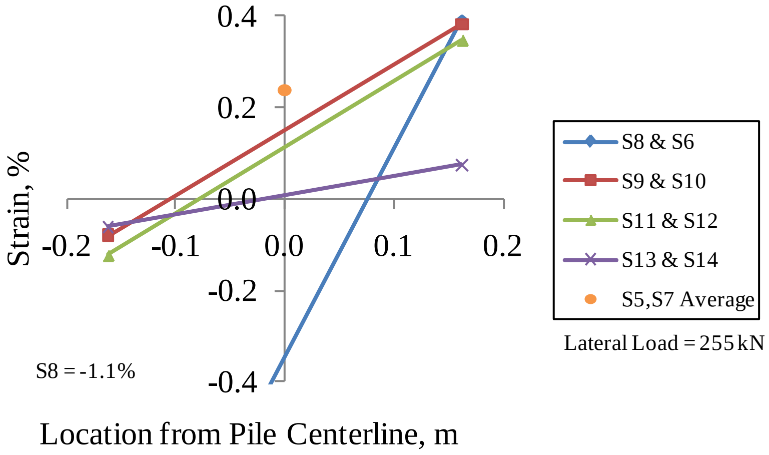

(a)

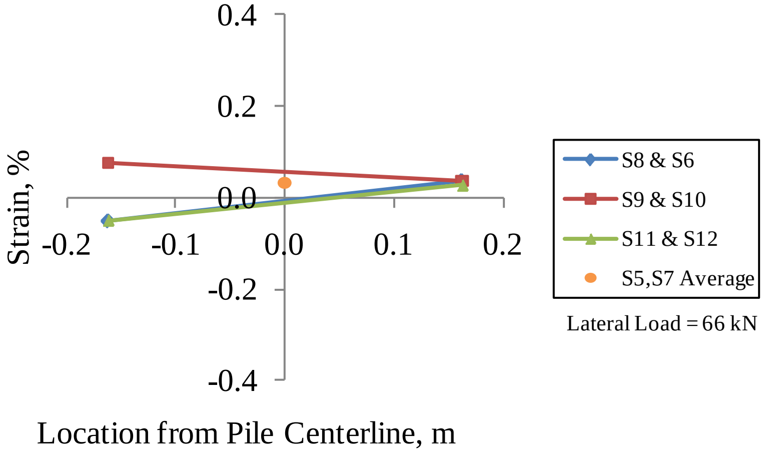

(b)

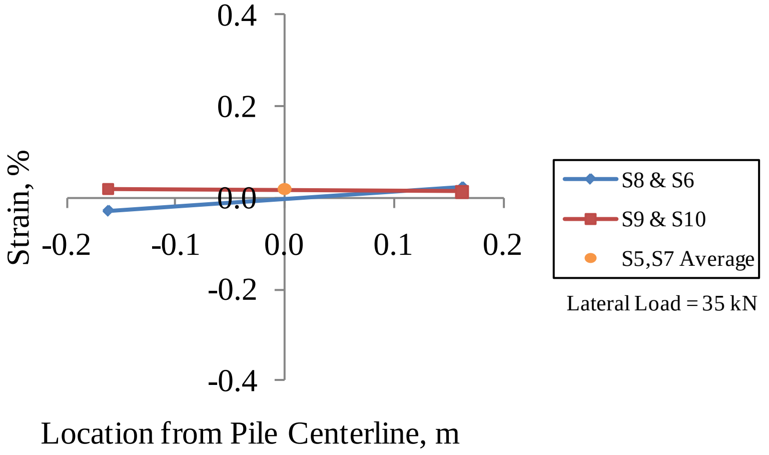

(c)

Figure 4-17: Strain vs. Location at Ultimate Load, a) Specimen 1, b) Specimen 2, c) Specimen 3

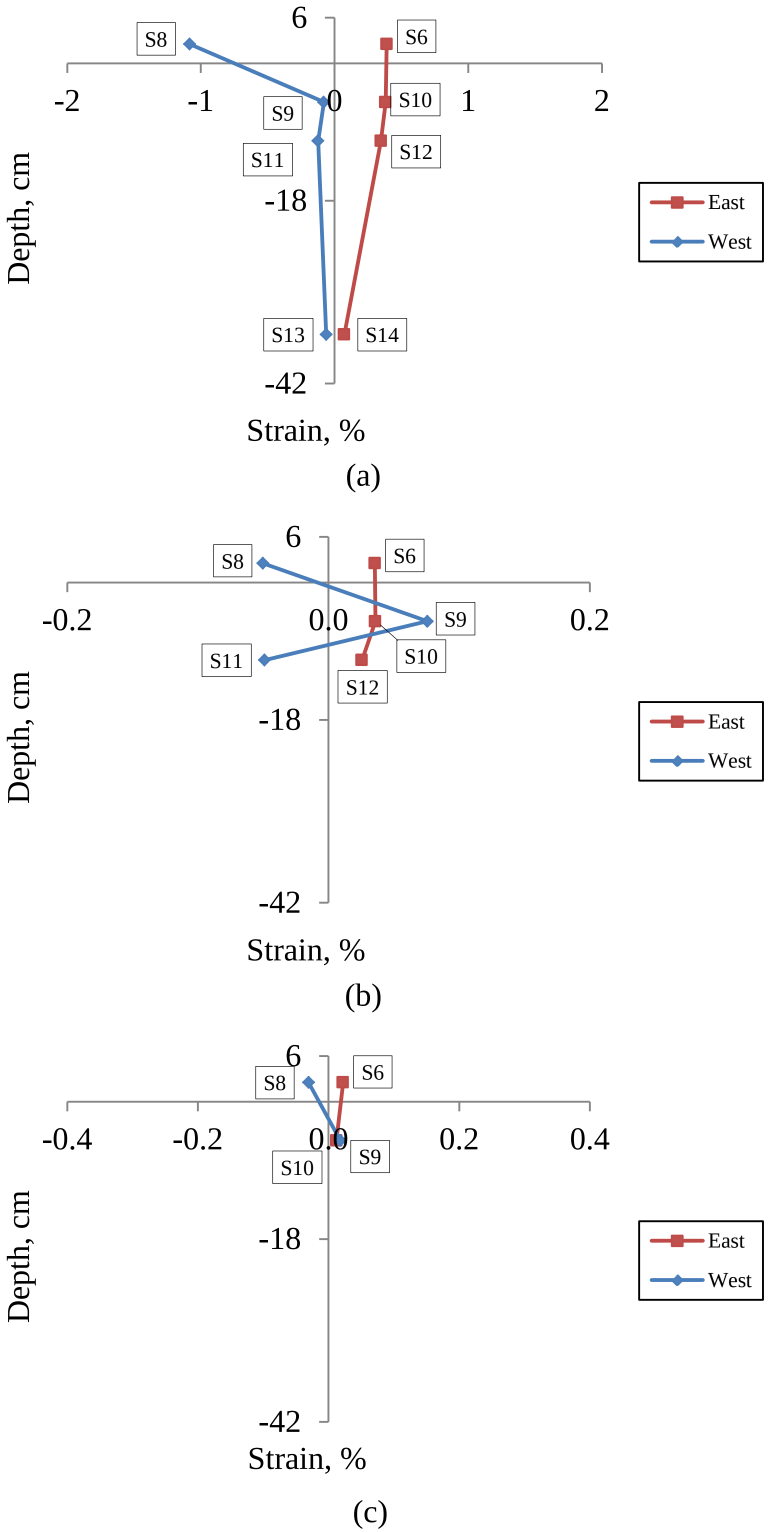

Figure 4-18: Strain vs. Depth at Ultimate Load, a) Specimen 1, b) Specimen 2, c) Specimen 3

5 DISCUSSION

5.1 Elastic Strength

Figure 4-14 showed the strength versus pile embedment depth for the three specimens and identified elastic capacities. Figure 5-1 and Figure 5-2 show the elastic capacity plotted against the normalized pile embedment depth. The elastic capacity shown in Figure 5-1 is the elastic moment capacity while the elastic capacity shown in Figure 5-2 is the maximum elastic lateral load. The elastic moment capacity is the moment corresponding to the maximum elastic lateral load. As shown in the figure, the elastic moment capacities of Specimens 2 and 3 were much lower than the elastic moment capacity of Specimen 1. The graphs suggest that the elastic capacity might be approximated by a linear function in terms of the normalized pile embedment depth, but the data is sparse.

5.2 Elastic Stiffness

The total deflection, Δ_t, of a pile-to-cap specimen is composed of two parts as shown in Figure 5-3. Part of the total deflection is due to the deflection of the pile, Δ_p. The other part of the total deflection is due to the rotation of the connection, Δ_c. Using the deflection from each mechanism, a corresponding stiffness can be determined.

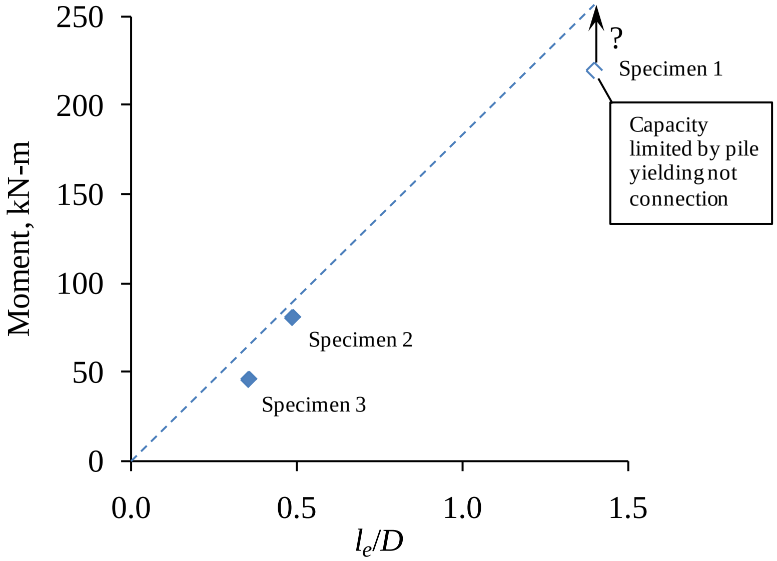

Figure 5-1: Elastic Moment vs. Normalized Pile Embedment Depth

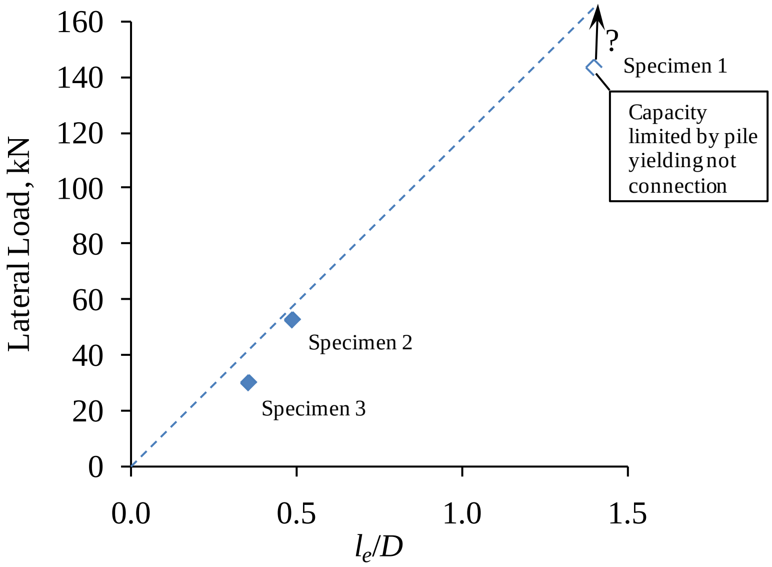

Figure 5-2: Maximum Elastic Load vs. Normalized Pile Embedment Depth

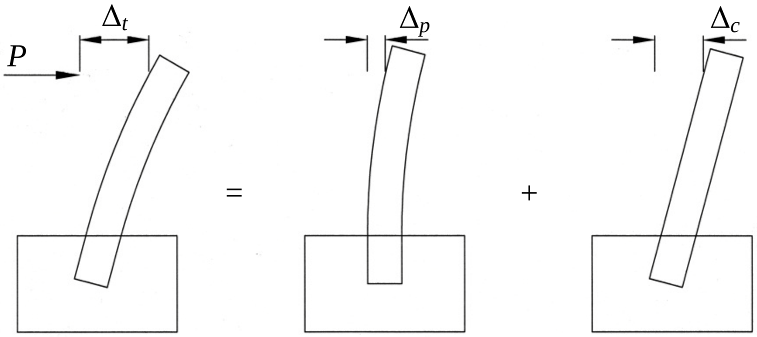

Figure 5-3: Mechanisms Considered in Elastic Stiffness

The total stiffness, k_t, is given by equation 5-1.

$$k_t = \frac{P}{\Delta_t} \tag{5-1}$$

where:
P = lateral load, kN
Δ_t = total deflection, m

The stiffness due to the pile can be determined using equation 5-2.

$$k_p = \frac{3EI}{L^3} \tag{5-2}$$

where:
E = modulus of elasticity of pile, kN/m^2
I = moment of inertia, m^4
L = length of pile, m

Since the total stiffness of the specimen is known from testing, the stiffness of the connection can be determined as given in equation 5-3.

$$\frac{1}{k_t} = \frac{1}{k_p} + \frac{1}{k_c} \tag{5-3}$$

where:
k_c = Stiffness due to connection, kN/m

The connection stiffness corresponding to the maximum elastic load for each specimen is plotted against the normalized pile embedment depth in Figure 5-4. As shown in the figure, the connection stiffness of the specimens increased with increasing pile embedment depth. The pile-to-cap connection that had adequate strength to permit the pile to yield still had flexibility in the connection; in other words, the connection stiffness certainly is not infinite as may be assumed in typical computer models. The shallow pile embedment depth of 0.16 m (6.25 in) provided more than half the connection stiffness of the deeper pile embedment depth of 0.45 m (17.9 in). Additional data is necessary to fully understand the relationship.

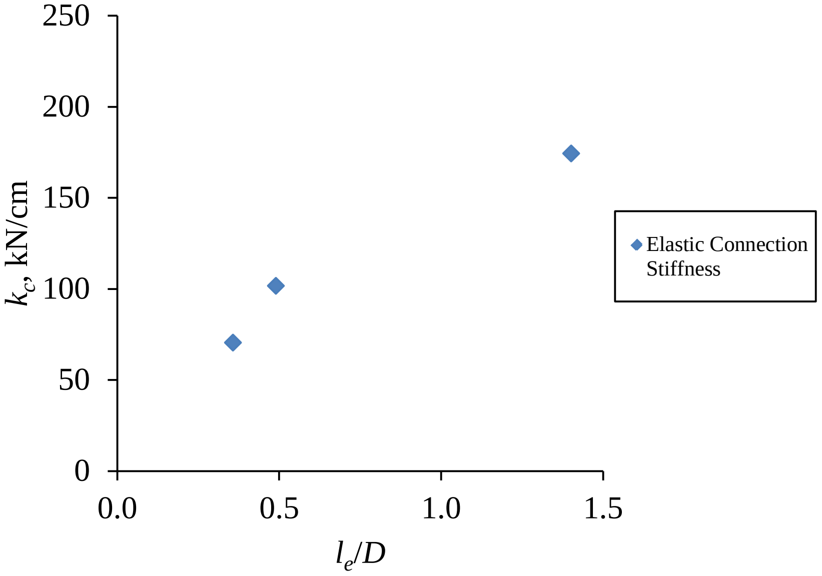

Figure 5-4: Elastic Connection Stiffness vs. Normalized Pile Embedment Depth

The total stiffness corresponding to the maximum elastic load for each specimen is plotted against the normalized pile embedment depth in Figure 5-5. A line representing the stiffness of the pile at a length of 1.53 m (60.3 in) is also shown in the figure. If the total stiffness were equal to the stiffness of the pile, the specimen would have infinite connection stiffness. As shown in the figure, however, the total stiffness of each specimen was much less than the stiffness of the pile for each specimen. The total stiffness of Specimen 1, for example, was about half the stiffness of the pile.

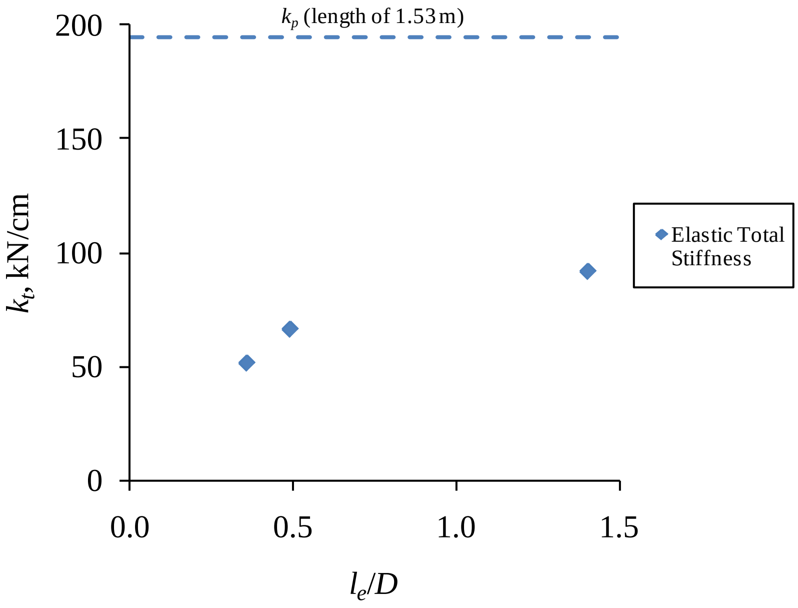

Figure 5-5: Elastic Total Stiffness vs. Normalized Pile Embedment Depth

The strain gage results indicate a bearing reaction at the end of the pile. As shown in Figure 4-16, for each specimen the strains in gages S6, S10, and S12 were very similar. This suggests that the load has not left the pile in these locations. The strains at the end of the pile [S14 in Figure 4-16(a), S12 in Figure 4-16(b), and S10 in Figure 4-16(c)] also show significant strain indicating that there is still load in the pile at these depths. These results suggest that the pile is bearing at the base in the direction that the pile is being pushed. This bearing force is not accounted for in the Marcakis and Mitchell model.

Strain gage S9 demonstrated unusual results for each of the three specimens. The results were unusual because the strain in gage S9 was less than the strain in gage S11 just below for Specimens 1 and 2 as shown in Figure 4-16(a) and Figure 4-16(b). A similar pattern seems to have been happening with Specimen 3. In addition, the strain in gage S9 for Specimens 2 and 3 was compressive while all the other strains reported on this side of the pile were tensile as shown in Figure 4-16 (b) and Figure 4-16 (c). It is difficult to explain this result. It may be related to the fact that the pile has peeled away from the concrete in these zones or it may be due to deformation of the pile.

To further understand the unusual results from strain gage S9, additional plots have been provided for each specimen. Figure 5-6 shows the strain for the reverse cycle at the maximum elastic load plotted versus depth. Gage S10 shows similar behavior as S9 did, confirming accurate data. Figure 5-7 shows the strain for the peak of the first cycle plotted versus depth. Even at low load levels, prior to observation of gap, the same trends in strain appear.

5.3 Model for Elastic Strength

A model was developed to estimate the elastic moment capacity for an embedded pile connection. Conceptually, the model is an elastic version of the Marcakis and Mitchell approach, with the addition of an end bearing force. Three reaction forces, shown in Figure 5-8, are considered in this model: the force at the front of the connection, C_f, the force at the back of the connection, C_b, and the pile end bearing force, C_e, with an equal and opposite balancing force. These forces are the resultants of stresses defined by the neutral axes in the horizontal and vertical directions as shown in the figure. The location of the horizontal axis is variable while the location of the vertical axis is assumed to be constant and located along the centerline of the pile.

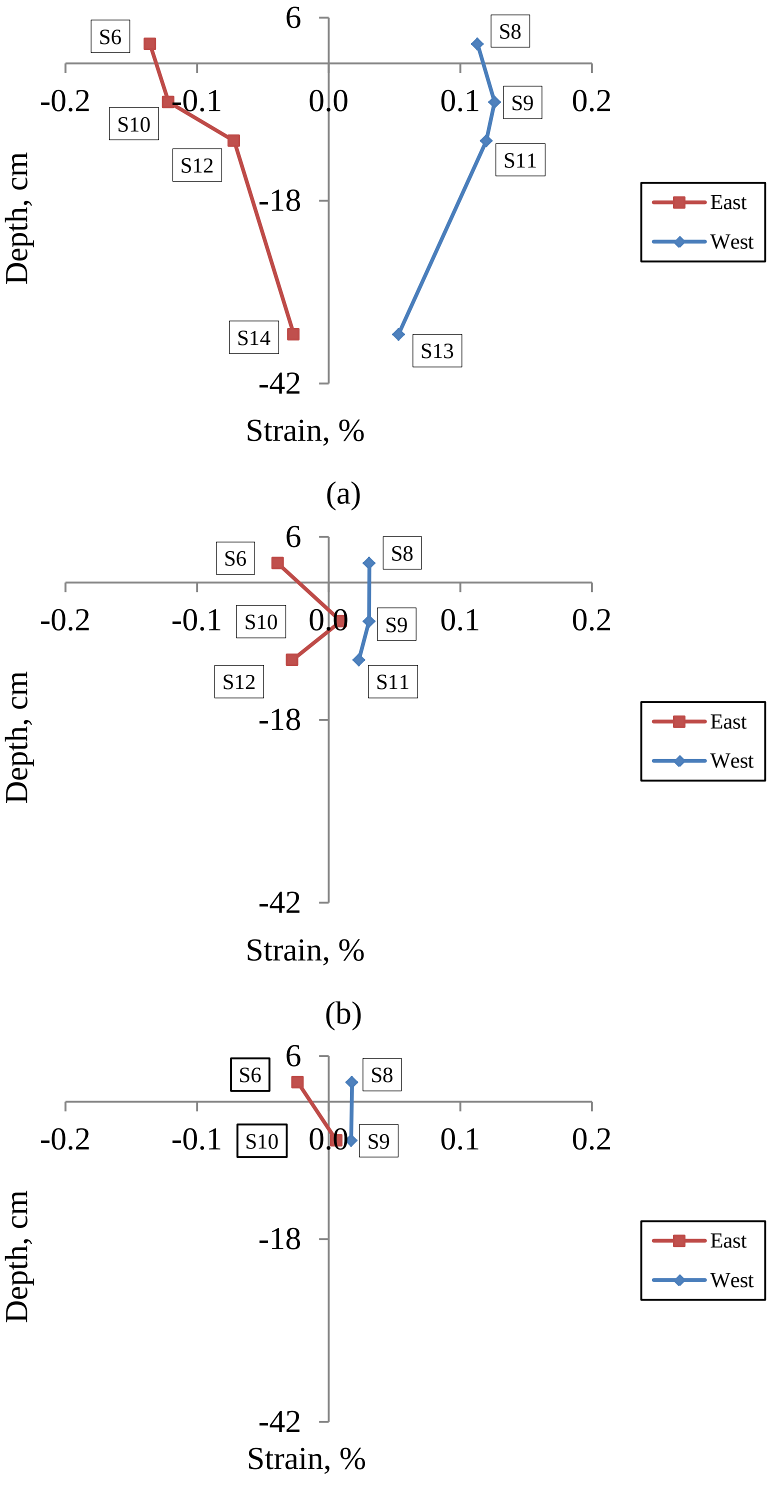

(a)

(b)

(c)

Figure 5-6: Strain vs. Depth at Reverse Cycle for Maximum Elastic Load, a) Specimen 1, b) Specimen 2, c) Specimen 3

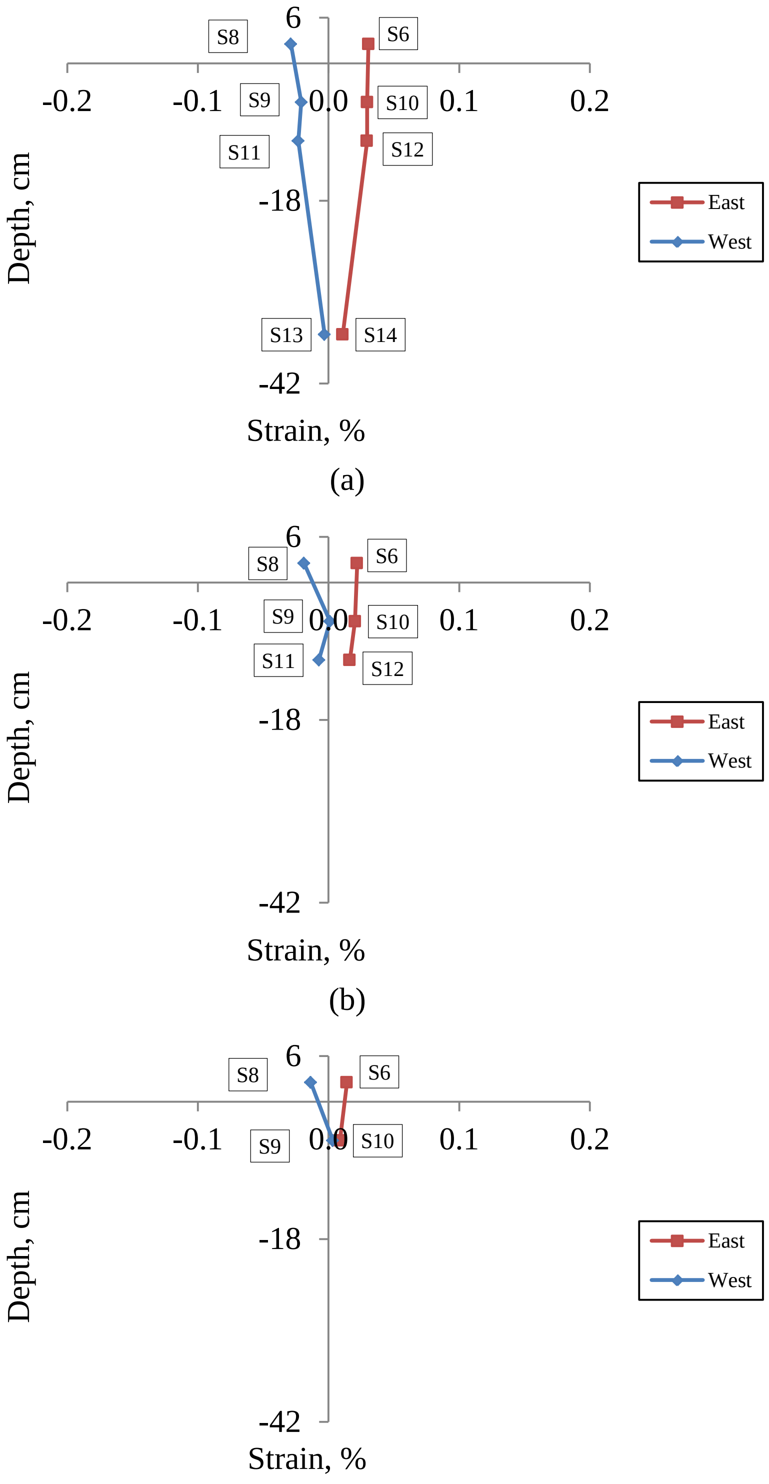

(a)

(b)

(c)

Figure 5-7: Strain vs. Depth at Peak Load of First Cycle, a) Specimen 1, b) Specimen 2, c) Specimen 3

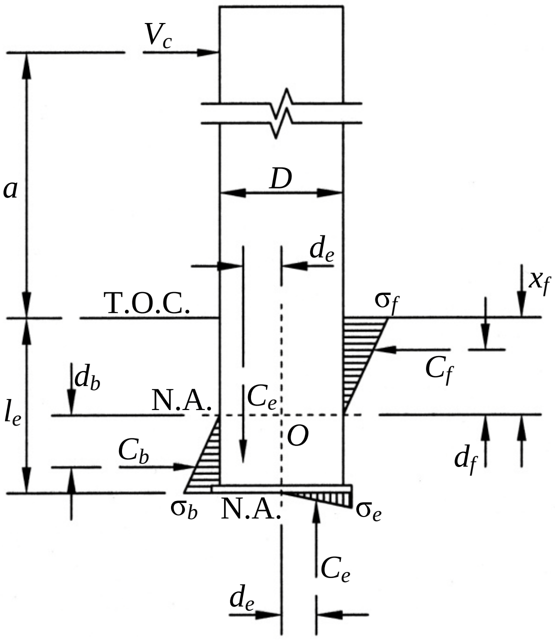

Figure 5-8: Stresses Used in Elastic Strength Model

With this model, if a few values are assumed, the rest can be calculated. The stresses at the front and back of the connection have a triangular distribution that is assumed to act over the width of the pile (the pile diameter). The maximum stress at the front of the connection is assumed to correspond to a concrete strain of 0.001. This can be determined using equation 5-4.

$$\sigma_f = \varepsilon_e E_c \qquad (5\text{-}4)$$

where:
$\varepsilon_e = 0.001$
$E_c = 4731\sqrt{f_c'}$, MPa
f_c' = Compressive strength of concrete, MPa

The magnitude of the resultant acting at the front of the connection can then be determined using equation 5-5.

$$C_f = \frac{1}{2} x_f D \sigma_f \qquad (5\text{-}5)$$

Since elastic loads are used, a linear relationship between the stress at the front and the back of the connection can be established as given by equation 5-6 allowing the stress at the back of the connection to be calculated.

$$\sigma_b = \left(l_e - x_f\right)\left(\frac{\sigma_f}{x_f}\right) \tag{5-6}$$

The magnitude of the resultant acting at the back of the connection can then be determined using equation 5-7.

$$C_b = \frac{1}{2}\left(l_e - x_f\right)D\sigma_b \tag{5-7}$$

The distances from the horizontal neutral axis to the locations of the front and back stress resultants are given by equations 5-8 and 5-9 respectively.

$$d_f = \frac{2}{3}x_f \tag{5-8}$$

$$d_b = \frac{2}{3}\left(l_e - x_f\right) \tag{5-9}$$

Once equations for the resultant forces at the front and back of the connection have been established, a force equilibrium equation can be formulated relating C_f, C_b, and V_c as given by equation 5-10.

$$V_c = C_f - C_b \tag{5-10}$$

The remaining discussion relates to the calculation of the force C_e. The value of C_e can be determined in three different ways. The first is to assume that the force, C_e, is equal to zero. This approach is equivalent to an elastic version of the model proposed by Marcakis and Mitchell. The second is to assume that the end bearing stress, σ_e, is similar to the stress at the back of the connection, σ_b. The third is to assume that the force, C_e, is limited by the friction force between the pile and the concrete at the back of the connection.

The pile end bearing stress is assumed to be zero in the middle of the pile and vary linearly to a stress, σ_e, at the edge. Assuming a rigid rotation about point *O*, σ_e should be similar to σ_b since each is located a similar distance from point *O*. As a result, the pile end bearing stress is given by equation 5-11.

$$\sigma_e \leq \sigma_b \tag{5-11}$$

The resultant of the pile end bearing stress is the "volume" of a cylindrical wedge and is given by equation 5-12 (see Appendix E for derivation).

$$C_e = \frac{1}{6} D^2 \sigma_e \tag{5-12}$$

The distance from the vertical neutral axis to the location of the pile end bearing resultant is given by equation 5-13 (see Appendix E for derivation).

$$d_e = \frac{3\pi D}{32} \tag{5-13}$$

A balancing vertical force, equal to C_e, is also assumed to exist in the model. This force may be due to friction between the pile and the concrete or resistance due to the lip of the plate welded to the end of the pile. If this force is assumed to be a friction force, it is limited in magnitude to $C_e \leq \mu_k C_b$ assuming $\mu_k = 0.35$ for kinetic friction between steel and concrete. This coefficient was determined by taking 75% of the static friction [$\mu_s = 0.47$, (Baltay and Gjelsvik 1990)] as suggested by Hibbeler (Hibbeler 2004). This force is assumed to act the same distance, d_e, from the neutral axis toward the back of the connection.

Using one of these three methods for computing the force C_e, the location of the neutral axis can then be found using moment equilibrium as given by equation 5-14.

$$V_c\left(a + x_f\right) = C_f d_f + C_b d_b + C_e d_e + C_e d_e \tag{5-14}$$

Once the location of the horizontal neutral axis has been determined, the maximum elastic load can then be calculated using previously defined equation 5-10.

The elastic strength model is compared with the elastic strength of the three pile-to-cap connection specimens in Figure 5-9. Three curves are shown in the figure. Each curve shows the elastic moment capacity of the connection using each of the three methods for computing C_e. The lowest curve is $C_e = 0$ (no end bearing force). The highest curve assumes the bearing stress is equal to the stress at the back of the connection ($\sigma_e = \sigma_b$). The middle curve assumes that the force, C_e, is limited by the friction force between the pile and the concrete at the back of the connection. The elastic strengths of the three test specimens are also shown in the figure.

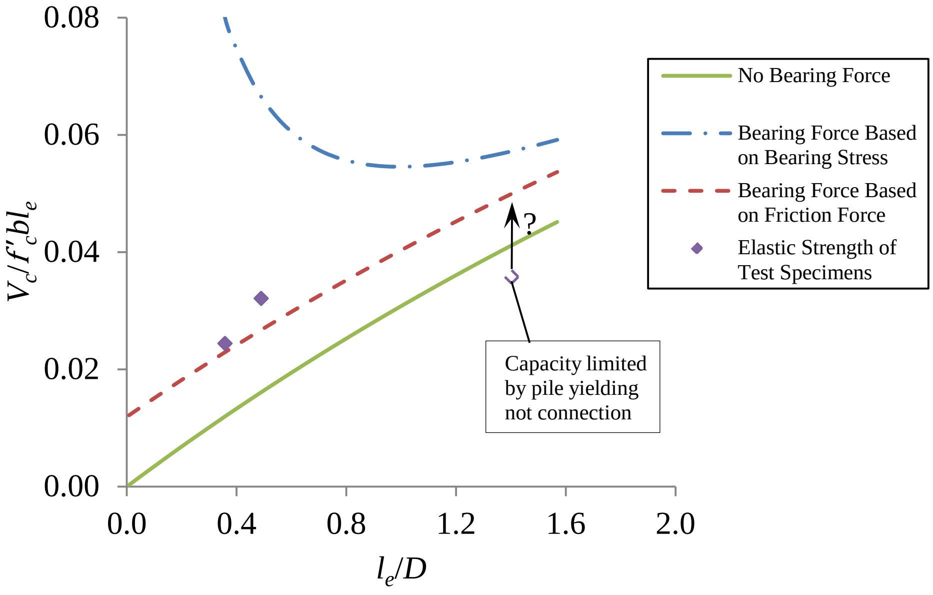

Figure 5-9: Model for Elastic Strength Compared with Elastic Strength of Specimens

Of the three approaches, the capacity calculated by limiting the force C_e to the friction force at the back of the connection appears to be the best fit to the elastic strength of the test specimens.

5.4 Ultimate Strength

Previously, Rollins and Stenlund performed field-testing on pile-to-cap connections similar to those described in this study. Each specimen consisted of two driven pipe piles with a single concrete cap. Specimen 1 had a pile embedment depth of 0.15 m (6 in) and Specimen 2 had a pile embedment depth of 0.30 m (12 in). The two specimens were loaded laterally until failure occurred. Both specimens failed due to pullout of the trailing pile. These two specimens tested by Rollins and Stenlund responded similarly to the lateral loading. The moment in the pile was measured in the locations shown in Figure 5-10 and Figure 5-11 for Specimens 1 and 2 respectively. The moments at the two locations in the trailing pile for Specimen 1 increased until a cap displacement of approximately 2 cm (0.8 in) after which the moment began to decrease. The moments at the same two locations for Specimen 2 increased at the same rate until a cap displacement of approximately 5 cm (1.97 in). Only the moment in the lower location of the leading pile was recorded for Specimen 1 while both the moments in the upper and lower locations were recorded for Specimen 2. Since the moments in the lower locations of the two specimens were very similar, however, it was assumed that the moments in the upper locations would also be very similar (Richards et al. 2011).

The measured moment capacity of Specimen 1 from the testing by Rollins and Stenlund was significantly larger than the calculated moment capacity. Although the specimen failed due to pile pullout of the trailing pile, the measured moment capacity of the leading pile was determined to be greater than 260 kN-m (192 kip-ft) (Richards et al. 2011). The maximum moment in the trailing pile was 110 kN-m (81.1 kip-ft) from Figure 5-10.

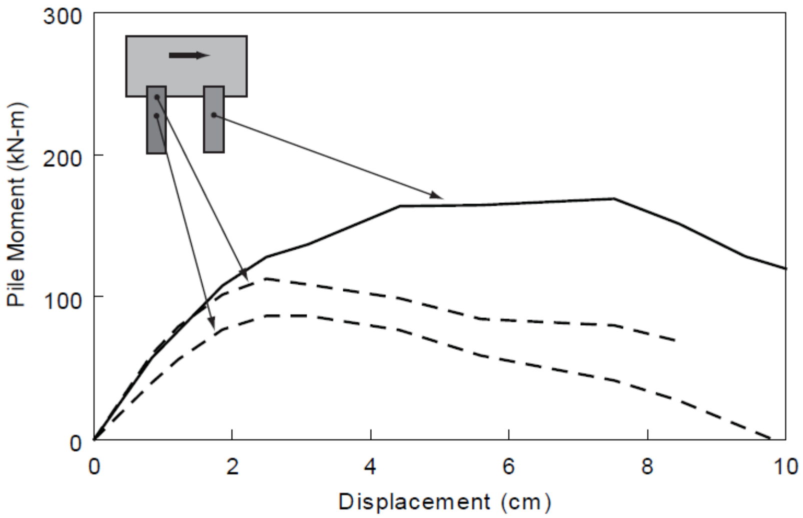

Figure 5-10: Response of Specimen 1 from Testing by Rollins and Stenlund [(Richards et al. 2011), used without permission]

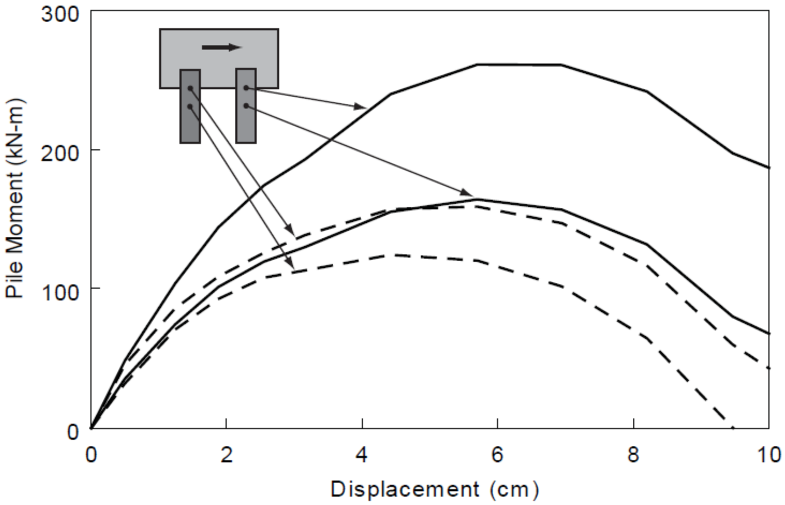

Figure 5-11: Response of Specimen 2 from Testing by Rollins and Stenlund [(Richards et al. 2011), used without permission]

Figure 5-12 shows information from the testing by Rollins and Stenlund and the experimental tests from this study. Two curves are shown in the figure representing the calculated moment capacity of an embedded steel member using the equation proposed by

Marcakis and Mitchell. For the lower curve, the equation has been plotted with an effective width equal to the width of the pile. For the upper curve, the equation has been plotted using an effective width equal to 2.5 times the width of the pile. Both curves are based on a concrete compressive strength of 27.6 MPa (4.0 ksi). The ultimate moment capacities for the leading and trailing piles of Specimen 1 from the testing by Rollins and Stenlund are also plotted in the figure. In addition, the ultimate moment capacities of the specimens from this study have also been shown in the figure.

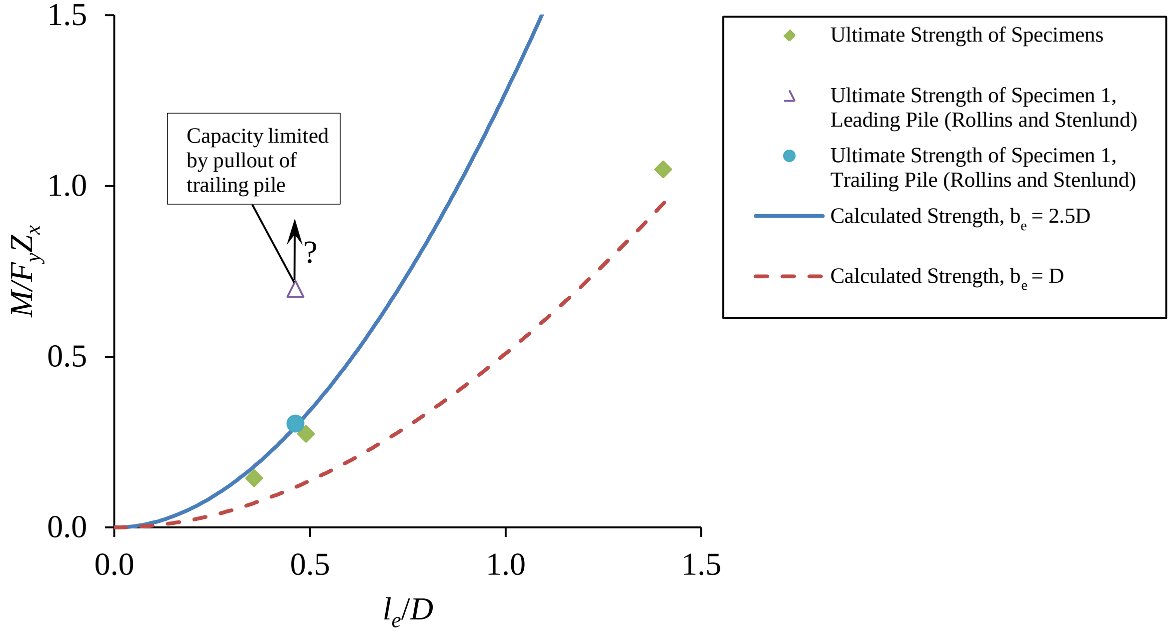

Figure 5-12: Ultimate Strength and Calculated Strength vs. Pile Embedment Depth

The trailing pile of Specimen 1 from the testing by Rollins and Stenlund and Specimen 2 from this study performed very similarly despite different testing conditions. These two connections were similar in pile embedment depth as well as pile diameter. However, Specimen 1 from the testing by Rollins and Stenlund was tested in the field with two piles embedded in a single cap. As a result, when the lateral load was applied to the cap, a tensile force was introduced in the trailing pile. In contrast, Specimen 2 from this study was tested with only a single pile without any axial loading.

The leading pile of Specimen 1 from the testing by Rollins and Stenlund had significantly greater moment capacity than either curve. The ultimate moment capacity of this specimen was over twice the moment capacity calculated using an effective width of 2.5 times the width of the pile. The capacity of this specimen cannot be explained by the Marcakis and Mitchell model.

The ultimate strengths of the three pile-to-cap specimens from this study were between the two curves shown in Figure 5-12. The ultimate strength of Specimen 1 was slightly above the calculated moment capacity using an effective width of one pile diameter. Specimens 2 and 3, however, were closer to the calculated moment capacity using an effective width of 2.5 pile diameters. This suggests that the best “effective width” to use in the equation actually varies with embedment and has nothing to do with width.

5.5 Ultimate Pile Strains

The strains at the ultimate load for Specimen 1 were presented in Figure 4-18(a). As shown in the figure, the highest tensile and compressive strains recorded in the pile at the ultimate load were observed in gages S6 and S8. Gage S8, however, reported a strain much higher than gage S6 suggesting that the pile cross-section did not yield evenly. Although, gages S6, S10, and S12 increased from the maximum elastic load, similar relative values were reported. The strain in gage S6 was greater by 212% at the ultimate load. Gage S14 reported a strain only 40% larger than the strain reported at the maximum elastic load.

The strains at the ultimate load for Specimen 2 were presented in Figure 4-18(b). As shown in the figure, the strain in strain gages S8, S9, and S11 increased from the maximum elastic load. In contrast, the strain in strain gages S6, S10, and S12 remained essentially unchanged from the maximum elastic load.

The strains at the ultimate load for Specimen 3 were presented in Figure 4-18(c). Like Specimen 2, the strains reported in strain gages S8 and S9 increased from the maximum elastic load. In addition, gages S6 and S10 remained essentially unchanged from the maximum elastic load.

5.6 Model for Ultimate Strength

A model was developed to determine the ultimate moment capacity of an embedded steel member. This model is based on two mechanisms: an embedment mechanism and an end bearing mechanism. The embedment mechanism used in the ultimate strength model is based on the principles presented by Marcakis and Mitchell. The end bearing mechanism for the ultimate strength model is the same as the end bearing mechanism that was presented for the elastic strength model. The two mechanisms used in the ultimate strength model are shown in Figure 5-13.

The forces that contribute to the embedment mechanism can be found using the equations developed by Marcakis and Mitchell. The force at the front of the connection is found by assuming an equivalent stress block. The magnitude and location of this force can be found by using equations 2-9 and 2-10 defined previously. The magnitude and location of the force at the back of the connection, which also assumes an equivalent stress block, can be found by using previously defined equations 2-6, 2-7, 2-8, and 2-11. Using force equilibrium equation 5-15 can be formulated.

$$V_c = C_f - C_b \tag{5-15}$$

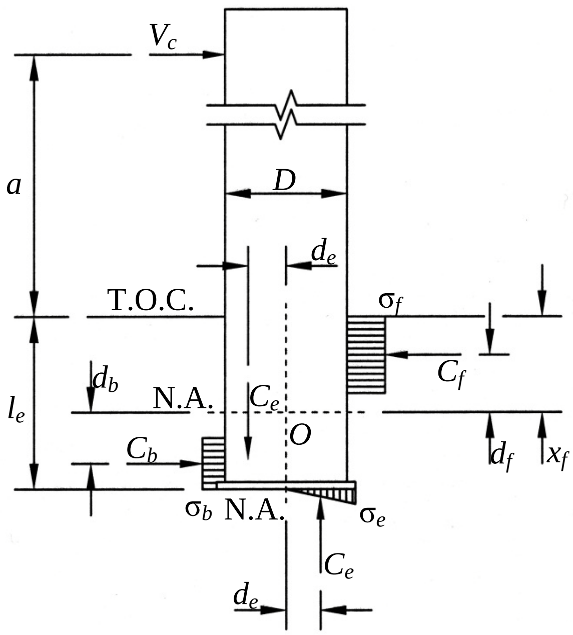

Figure 5-13: Stresses used in Ultimate Strength Model

For the end bearing mechanism, the force C_e acts at the end of the member as well as vertically toward the back of the connection as shown in Figure 5-13. The same three methods that were used in the elastic strength model are used to calculate the force C_e in the ultimate strength model. For the first method, the force C_e equals zero. For the second method, the magnitude and location of the force C_e is found using equations 5-11, 5-12, and 5-13. For the third method, the force C_e can be calculated using the friction force at the back of the connection as defined for the elastic strength model.

Using equations for the resultants from the embedment mechanism and one of these three methods to calculate the force C_e, the location of the neutral axis can then be found using moment equilibrium as given by equation 5-16.

$$V_c\left(a+x_f\right) = C_f d_f + C_b d_b + C_e d_e + C_e d_e \tag{5-16}$$

Once the depth to the horizontal neutral axis is known, the resultant force at the front of the connection, C_f, and the resultant force at the back of the connection, C_b, can then be determined. Using force equilibrium as given by previously defined equation 5-15, the ultimate load can then be determined.

The ultimate strength model is compared with the ultimate strength of the three pile-to-cap connection specimens in Figure 5-14. Figure 5-15 also shows the ultimate strength of the specimens, however, the ultimate strength in this figure is normalized. Like Figure 5-9 for the elastic strength model, the figures also show three curves representing the capacity computed using each of the three methods for computing C_e. The capacity shown in the figures, however, is the ultimate capacity. In addition, the maximum shear force calculated using the Marcakis and Mitchell equation is also shown in each of the figures. These capacities can be compared with the ultimate strengths of the three specimens from this study.

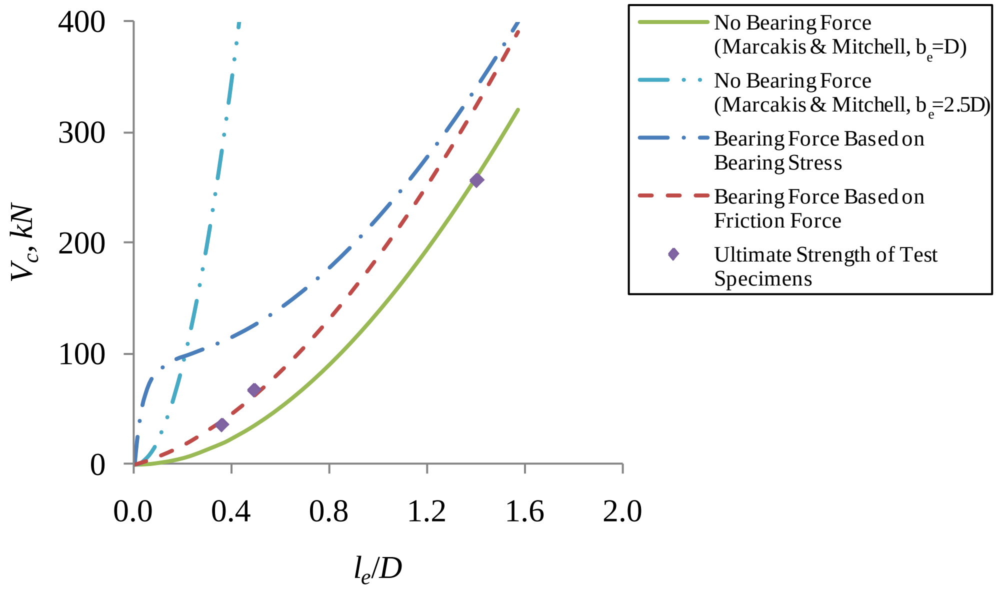

Figure 5-14: Ultimate Strength Model Compared with Ultimate Strength of Specimens

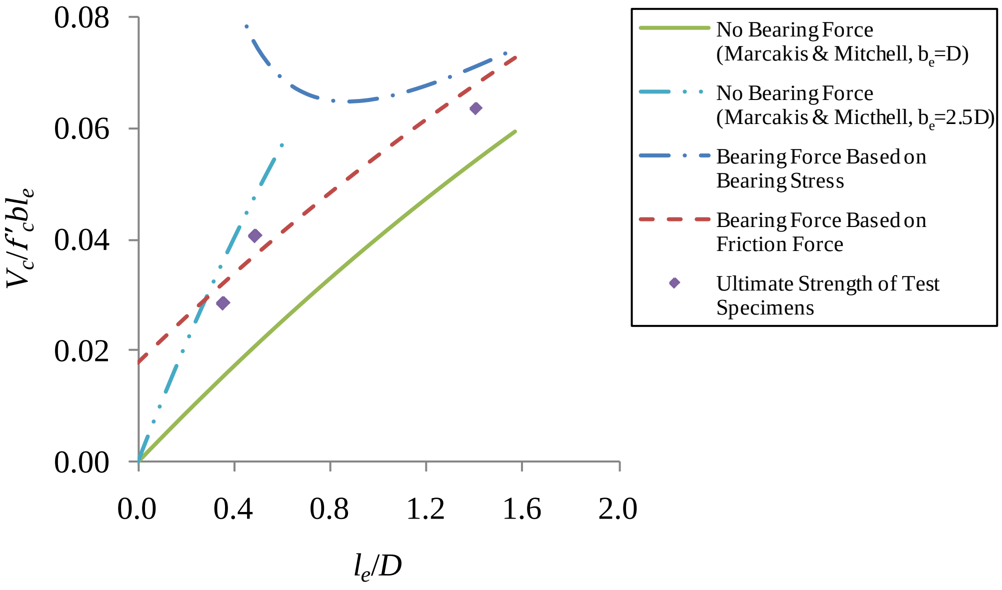

Figure 5-15: Ultimate Strength Model Compared with Ultimate Strength of Specimens

Like the elastic strength model, the maximum shear force calculated by limiting the force C_e to the friction force at the back of the connection appears to be the best fit to the ultimate strengths of the test specimens.

As shown in Figure 5-15, the maximum shear force limited by the friction force at the back of the connection is not conservative for Specimens 1 and 3. However, if the coefficient of friction is reduced to 0.23 then the maximum shear force calculated with this model is conservative. This model, shown in Figure 5-16, may be reasonable since it predicts the maximum shear force of two of the three specimens very well. More data points are needed, however, to verify this model.

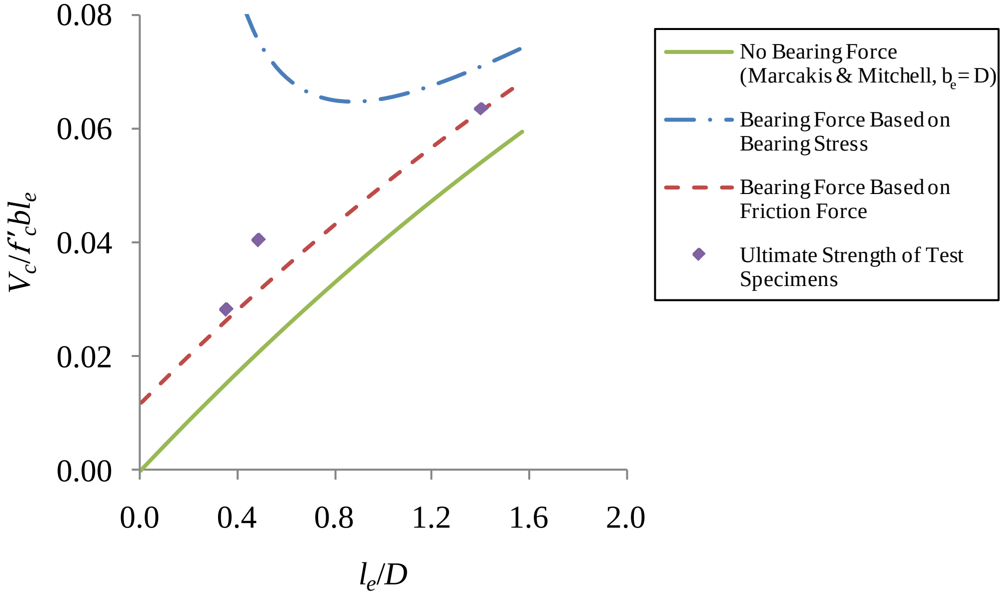

Figure 5-16: Ultimate Strength Model with Required Coefficient of Friction

6 CONCLUSION

An experimental study investigated steel pipe pile-to-cap connections without reinforcement. Three pile-to-cap connection specimens varying only in pile embedment depth were laterally loaded to failure. The pile-to-cap connection with the deepest pile embedment depth of 1.5 pile diameters had sufficient capacity for the pile to yield. The other two pile-to-cap connections with shallower pile embedment depths of 0.5 and 0.4 pile diameters had less capacity.

Based on the results from the experimental testing, the following conclusions can be made.

1. Pile-to-cap connections with minimal pile embedment depth still have significant moment resisting capacity. A connection with a pile embedment of only 0.5 pile diameters had over a third of the moment resisting capacity of a connection with a pile embedment of 1.5 pile diameters at the maximum elastic load.
2. Pile-to-cap connections with minimal pile embedment depth still have significant rotational stiffness. A shallow pile embedment of only 0.5 pile diameters provided more than half the connection stiffness of a deeper pile embedment depth of 1.5 pile diameters.
3. The maximum shear force of a connection with 1.5 pile diameters of embedment is reasonably predicted using the equation presented by Marcakis and Mitchell if an

effective width equal to the width of the pile is assumed. The maximum shear force of connections with shallow pile embedment depths, however, cannot be correctly calculated using an effective width equal to the width of the pile.

4. Pile-to-cap connections with shallow pile embedment rely on end bearing resistance for additional moment resisting capacity. A model that includes end bearing, limited by friction, appears to describe the capacity.
5. The effective width proposed by Marcakis and Mitchell probably accounts for some end bearing. The capacity being modeled as proposed, however, is more accurate in considering the relative contribution from end bearing as a function of embedment depth.

REFERENCES

American Concrete Institute. *Building Code Requirements for Structural Concrete (ACI 318-08) and Commentary*. Farmington Hills, MI: American Concrete Institute, 2008.

ASTM International. *Annual Book of ASTM Standards.* Vol. 1. West Conshohocken, PA: ASTM International, 2010.

Baltay, P., and A. Gjelsvik. "Coefficient of Friction for Steel on Concrete at High Normal Stress." *Journal of Materials in Civil Engineering*, February 1990: 46-49.

Budhu, M. *Soil Mechanics and Foundations.* Hoboken, NJ: John Wiley & Sons, Inc., 2007.

Das, B. M. *Principles of Foundation Engineering.* Stamford, CT: Cengage Learning, 2011.

Hibbeler, R.C. *Engineering Mechanics: Statics.* New Jersey: Pearson Prentice Hall, 2004.

Marcakis, K. "Precast Concrete Connections with Embedded Steel Members." Thesis, Department of Civil Engineering and Applied Mechanics, McGill University, Montreal, 1979.

Marcakis, K., and D. Mitchell. "Precast Concrete Connections with Embedded Steel Members." *PCI Journal* 25 (1980): 88-116.

Pertold, J., R.Y. Xiao, and F. Wald. "Embedded Steel Column Bases II. Design Model Proposal." *Journal of Constructional Steel Research*, 2000: 271-286.

Prestressed Concrete Institute. *PCI Design Handbook - Prescast and Prestressed Concrete.* Chicago, 1971.

Richards, P. W., K. M. Rollins, and T. E. Stenlund. "Experimental Testing of Pile-to-Cap Connections for Embedded Pipe Piles." *Journal of Bridge Engineering*, March/April 2011: 286-294.

Sheppard, D. A. "Seismic Design of Prestressed Concrete Piling." *PCI Journal*, 1983: 21-49.

Silva, P. F., and F. Seible. "Seismic Performance Evaluation of Cast-in-Steel-Shell (CISS) Piles." *Structural Journal* 98, no. 1 (January 2001): 36-49.

Xiao, Y. "Experimental studies on precast prestressed concrete pile to CIP concrete pile-cap connections." *PCI journal*, 2003: 82-91.

APPENDIX A. STRAIN DATA FROM TESTING

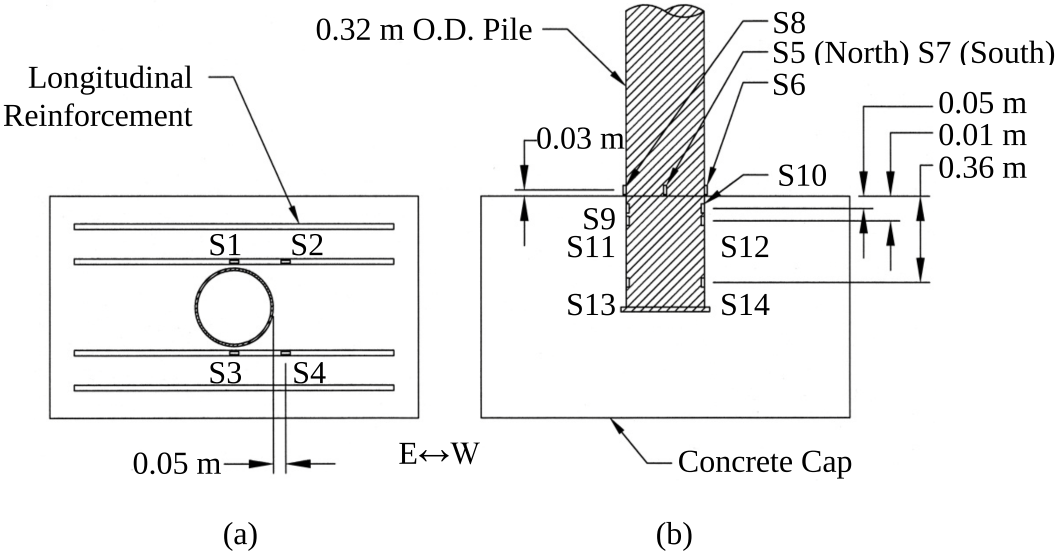

Longitudinal Reinforcement
S1
S2
S3
S4
0.05 m
E↔W
0.32 m O.D. Pile
S8
S5 (North) S7 (South)
S6
0.05 m
0.01 m
0.36 m
0.03 m
S10
S9
S11
S12
S13
S14
Concrete Cap
(a)
(b)

Figure A-1: Strain Gauges Used to Measure the Response of the System, a) Plan View, b) Side View

A.1 Specimen 1

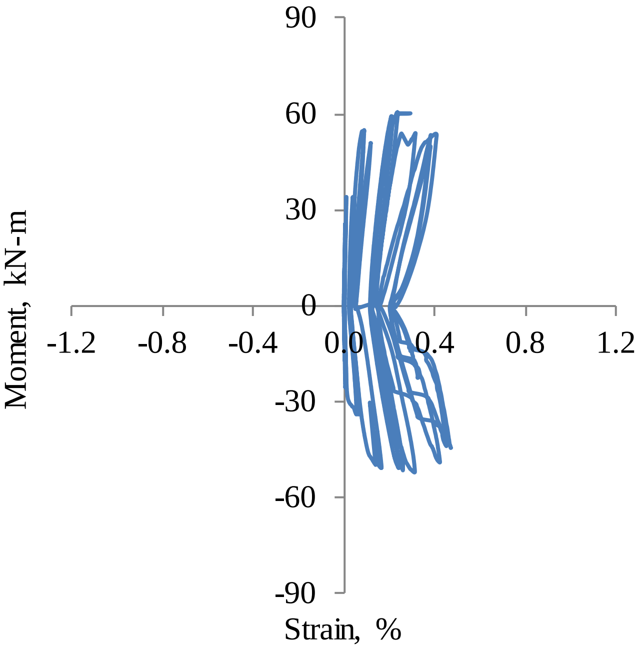

Figure A-2: Moment vs. Strain for Gauge S1 on Specimen 1

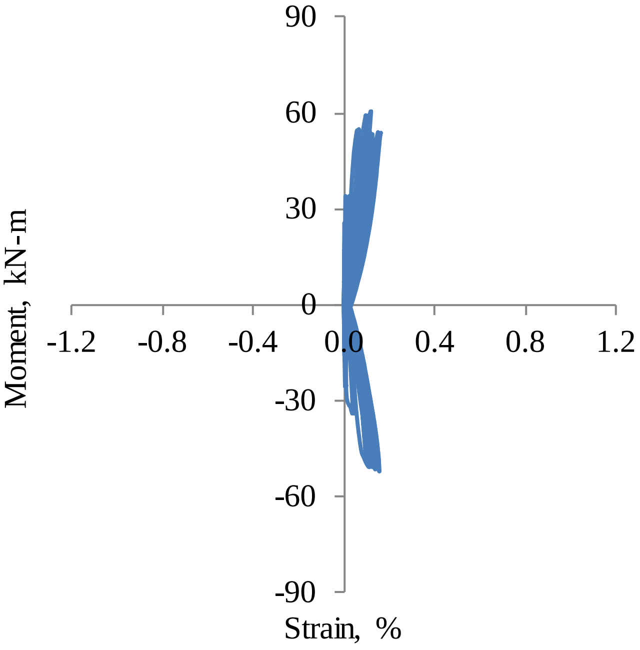

Figure A-3: Moment vs. Strain for Gauge S2 on Specimen 1

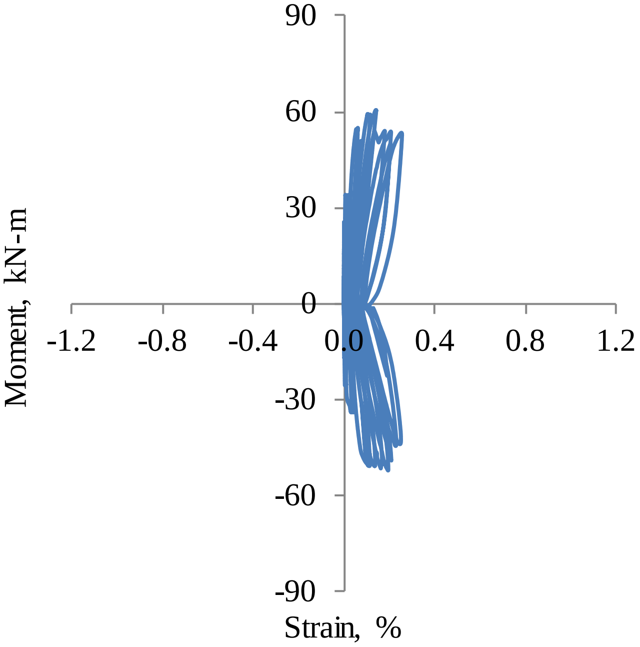

Figure A-4: Moment vs. Strain for Gauge S3 on Specimen 1

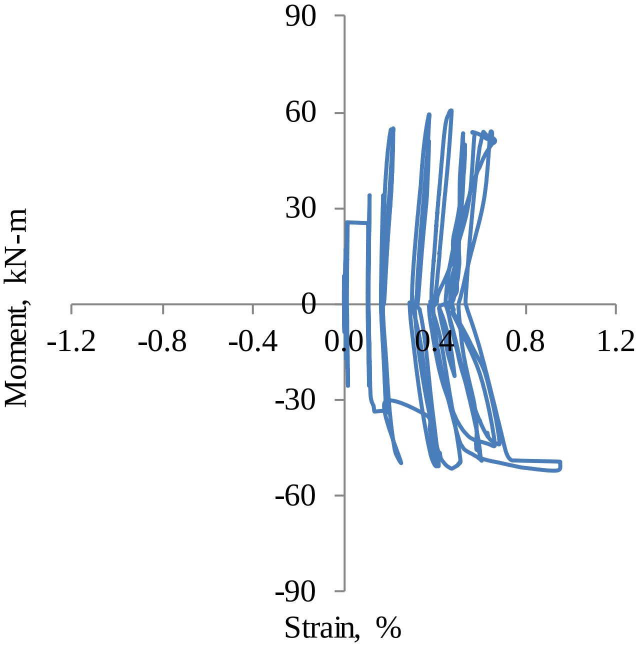

Figure A-5: Moment vs. Strain for Gauge S4 on Specimen 1

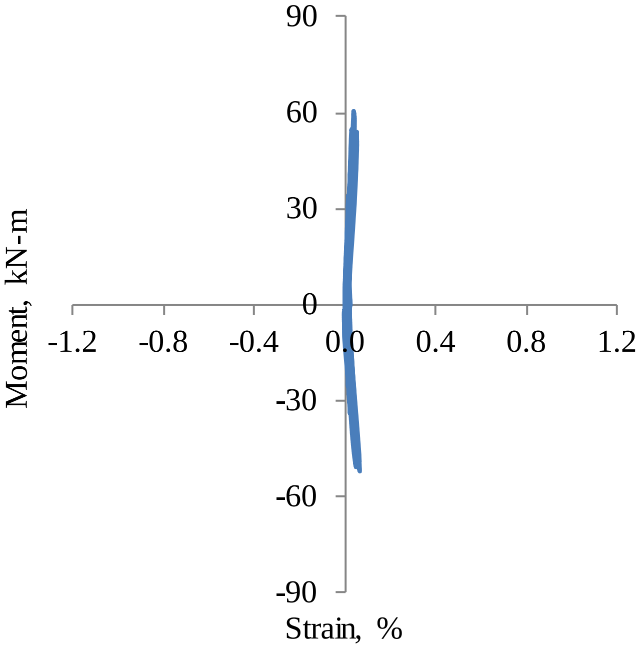

Figure A-6: Moment vs. Strain for Gauge S5 on Specimen 1

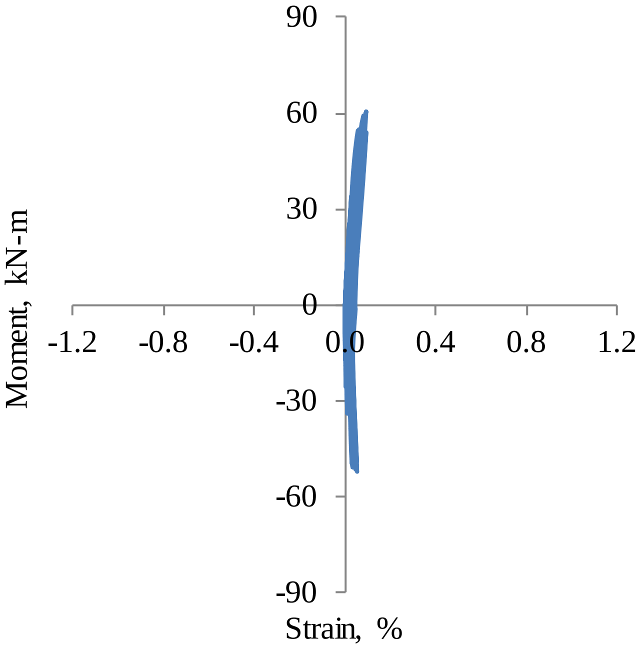

Figure A-7: Moment vs. Strain for Gauge S7 on Specimen 1

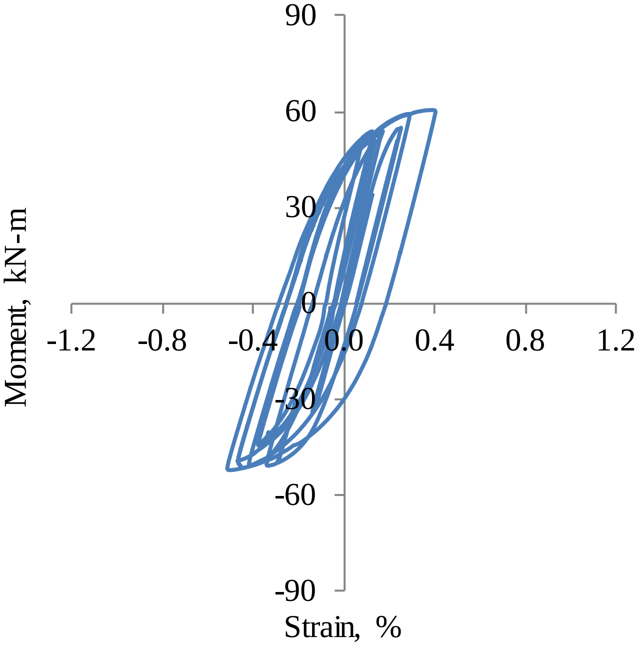

Figure A-8: Moment vs. Strain for Gauge S6 on Specimen 1

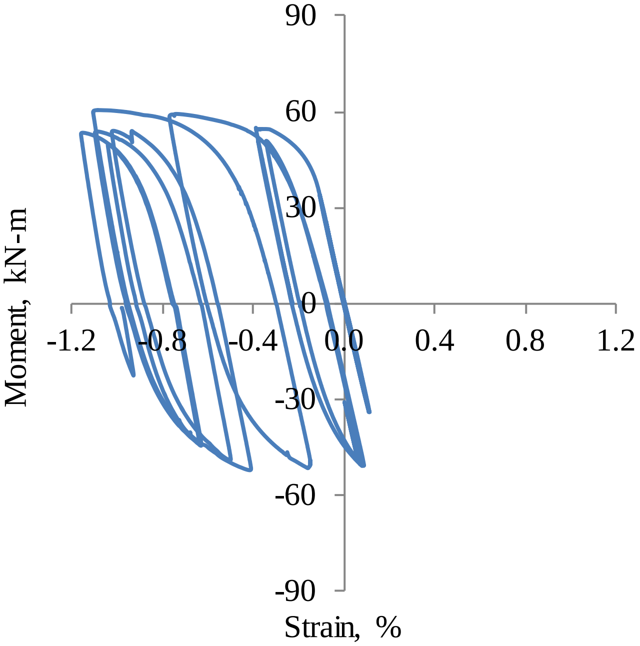

Figure A-9: Moment vs. Strain for Gauge S8 on Specimen 1

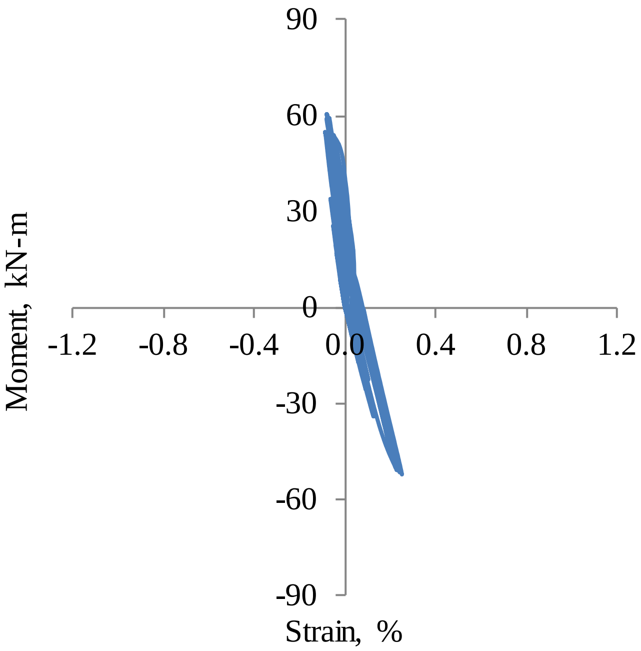

Figure A-10: Moment vs. Strain for Gauge S9 on Specimen 1

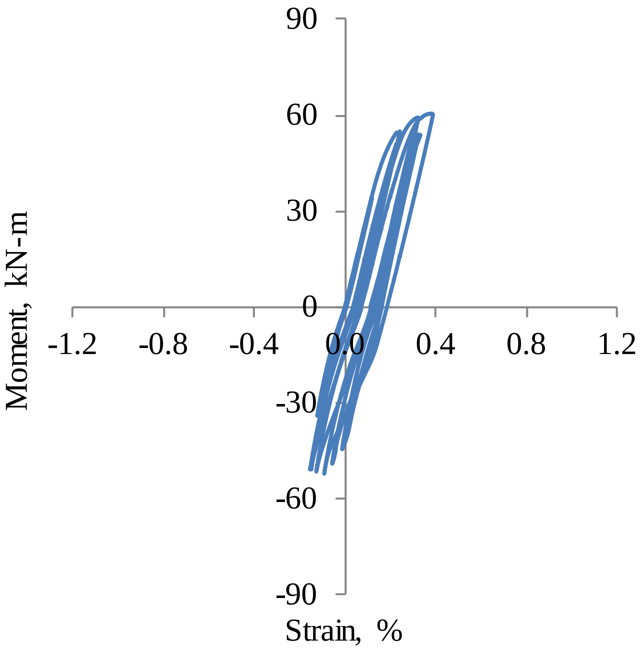

Figure A-11: Moment vs. Strain for Gauge S10 on Specimen 1

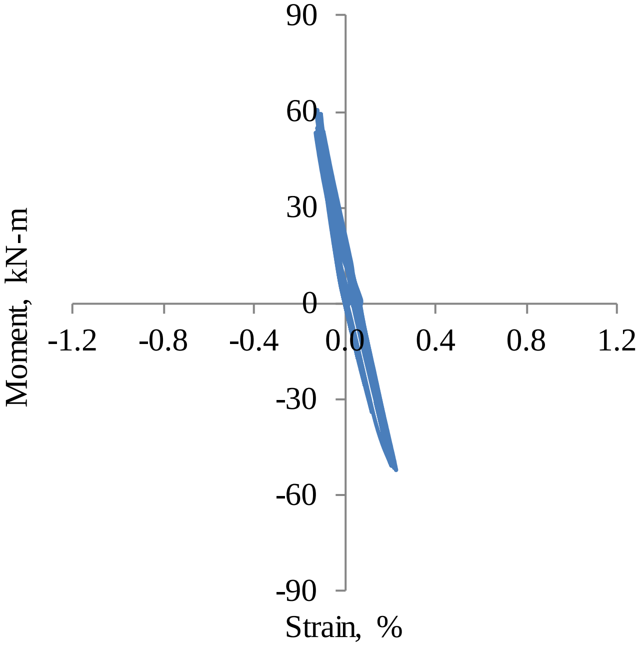

Figure A-12: Moment vs. Strain for Gauge S11 on Specimen 1

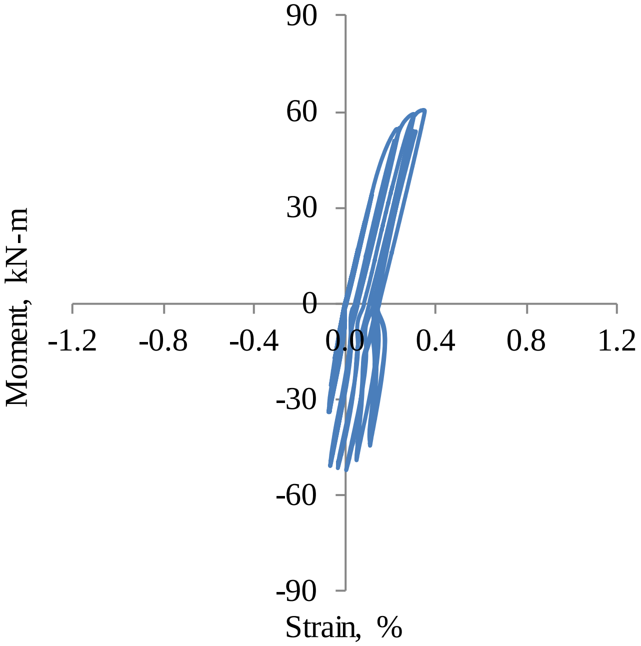

Figure A-13: Moment vs. Strain for Gauge S12 on Specimen 1

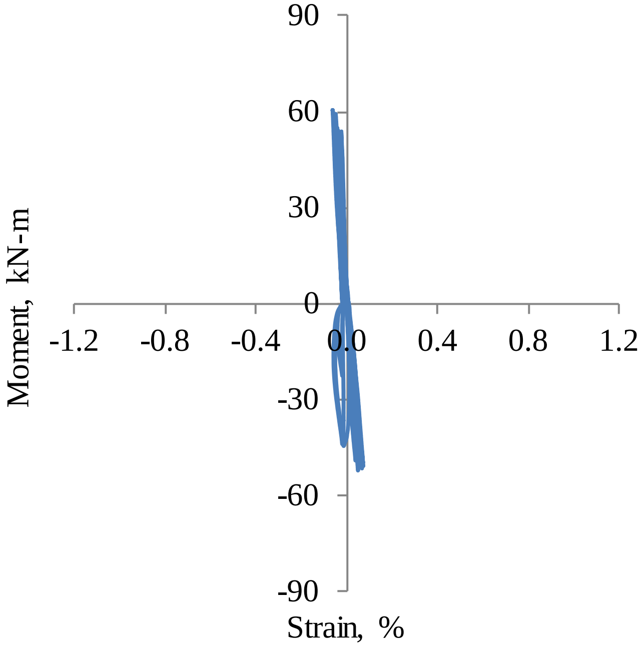

Figure A-14: Moment vs. Strain for Gauge S13 on Specimen 1

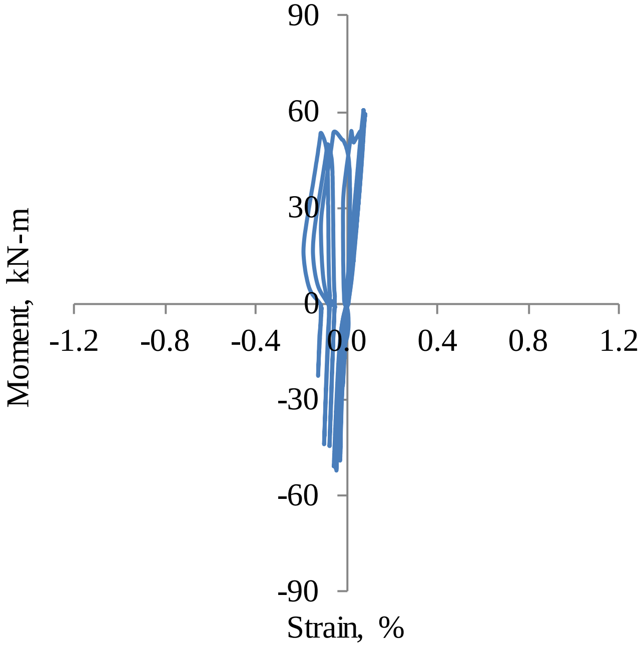

Figure A-15: Moment vs. Strain for Gauge S14 on Specimen 1

A.2 Specimen 2

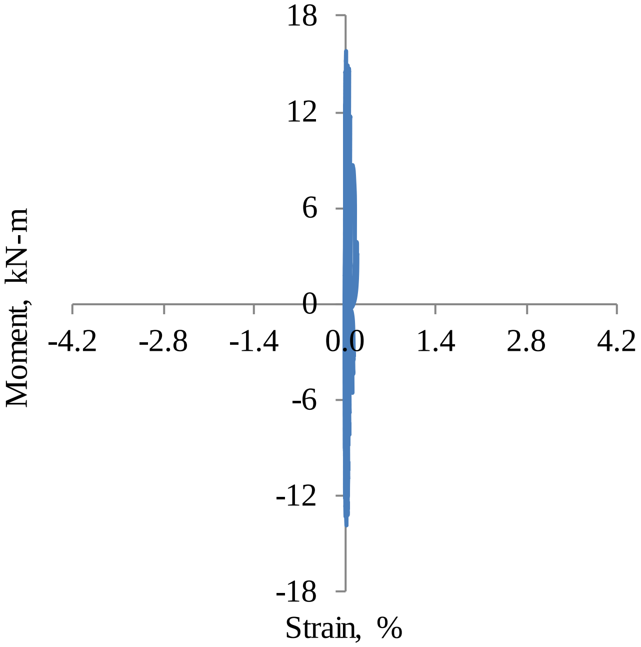

Figure A-16: Moment vs. Strain for Gauge S1 on Specimen 2

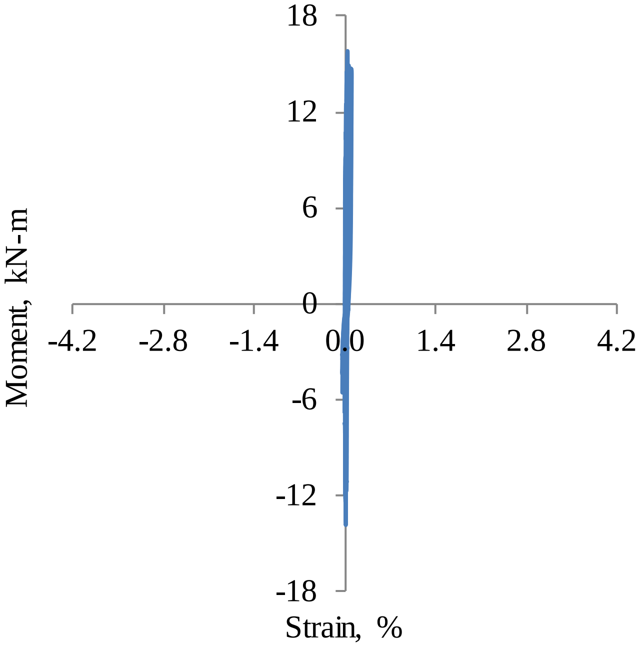

Figure A-17: Moment vs. Strain for Gauge S2 on Specimen 2

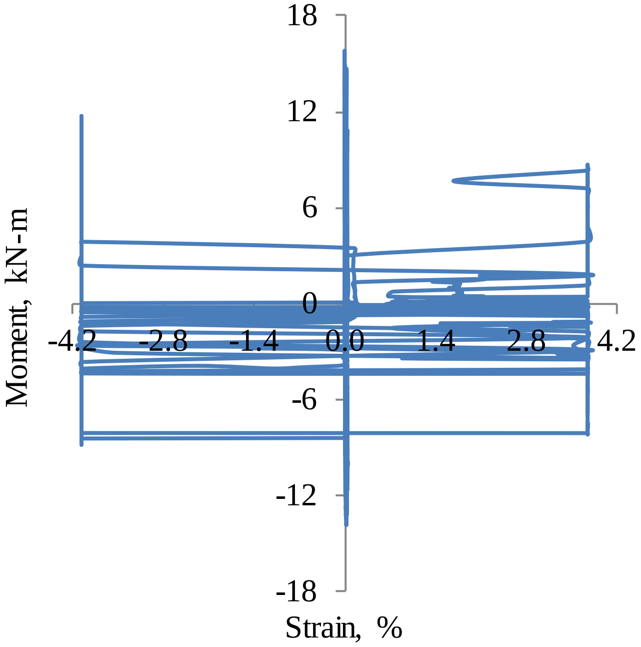

Figure A-18: Moment vs. Strain for Gauge S3 on Specimen 2

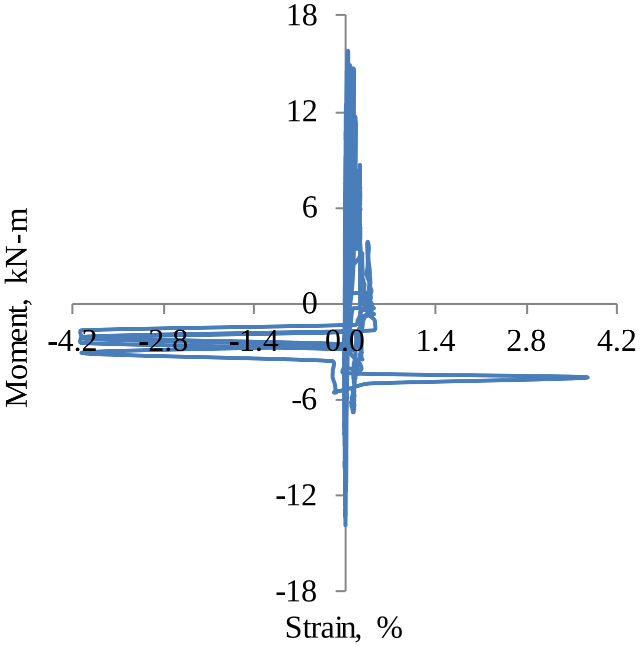

Figure A-19: Moment vs. Strain for Gauge S4 on Specimen 2

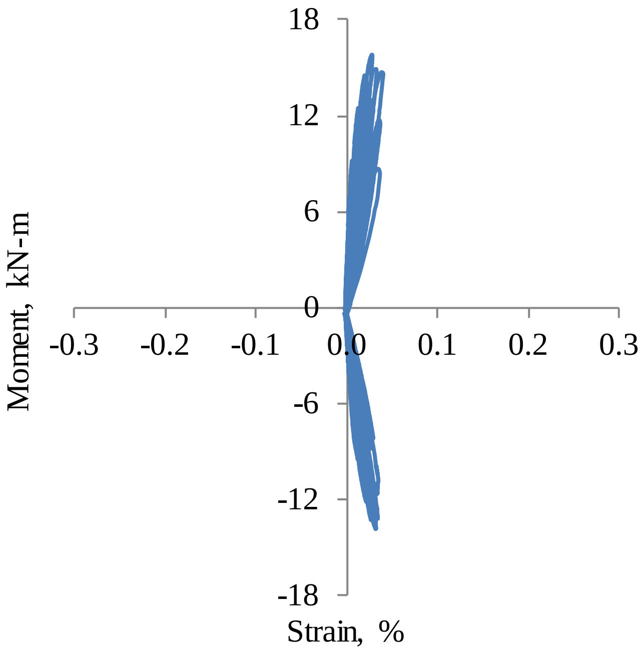

Figure A-20: Moment vs. Strain for Gauge S5 on Specimen 2

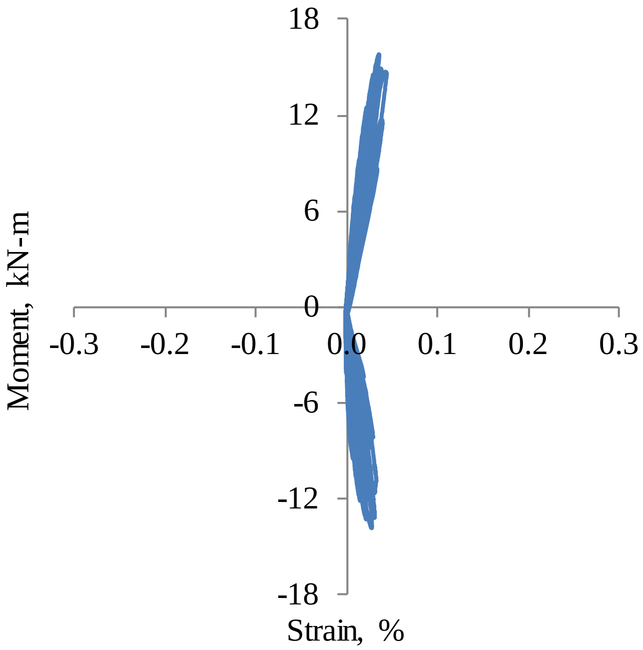

Figure A-21: Moment vs. Strain for Gauge S7 on Specimen 2

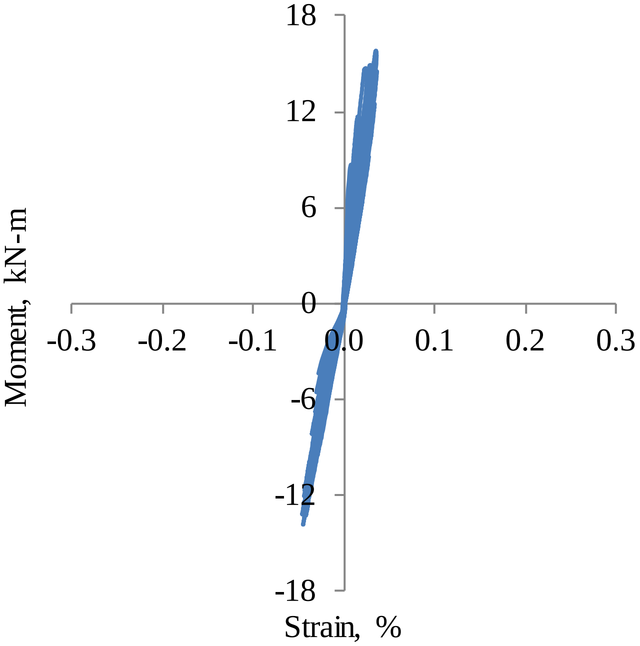

Figure A-22: Moment vs. Strain for Gauge S6 on Specimen 2

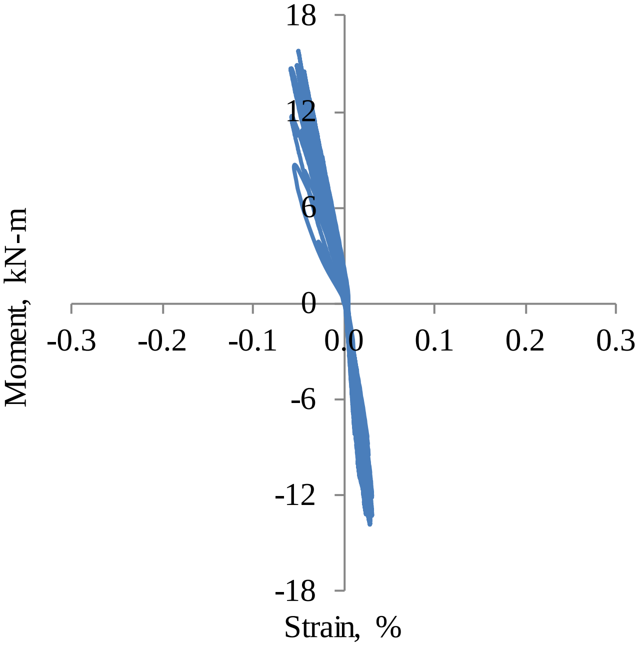

Figure A-23: Moment vs. Strain for Gauge S8 on Specimen 2

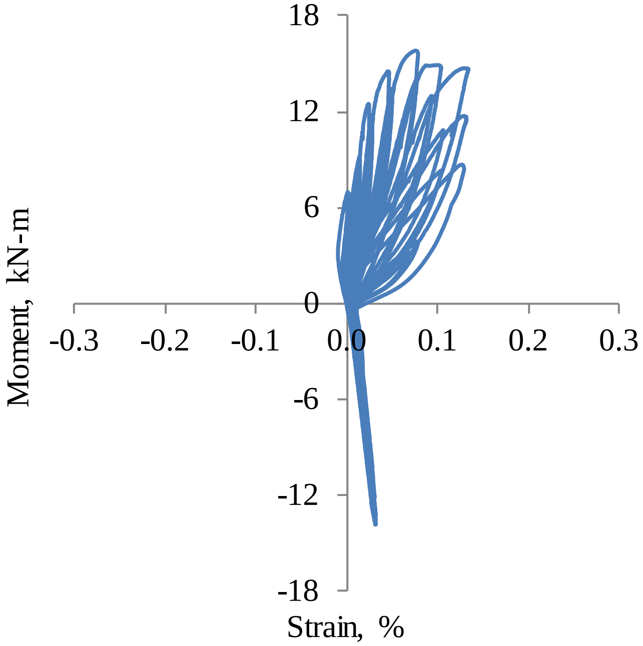

Figure A-24: Moment vs. Strain for Gauge S9 on Specimen 2

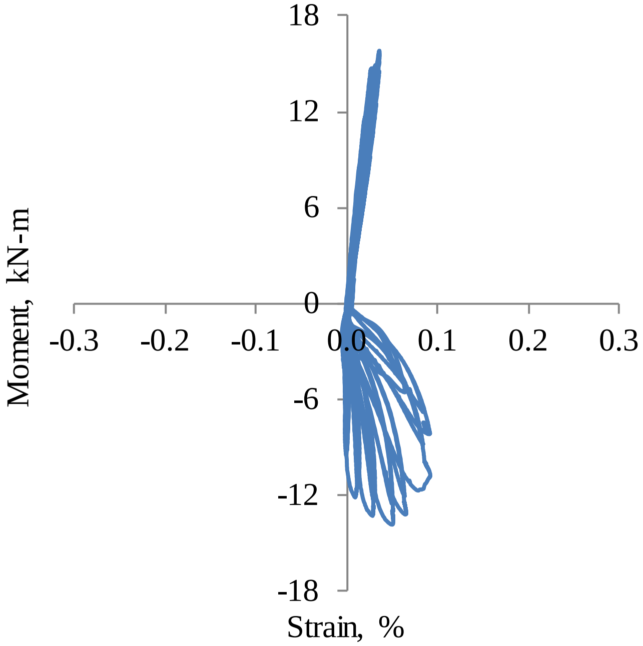

Figure A-25: Moment vs. Strain for Gauge S10 on Specimen 2

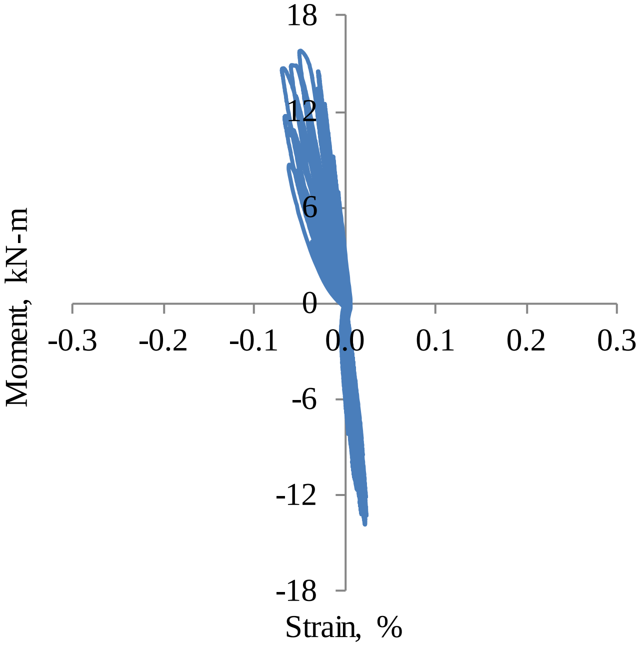

Figure A-26: Moment vs. Strain for Gauge S11 on Specimen 2

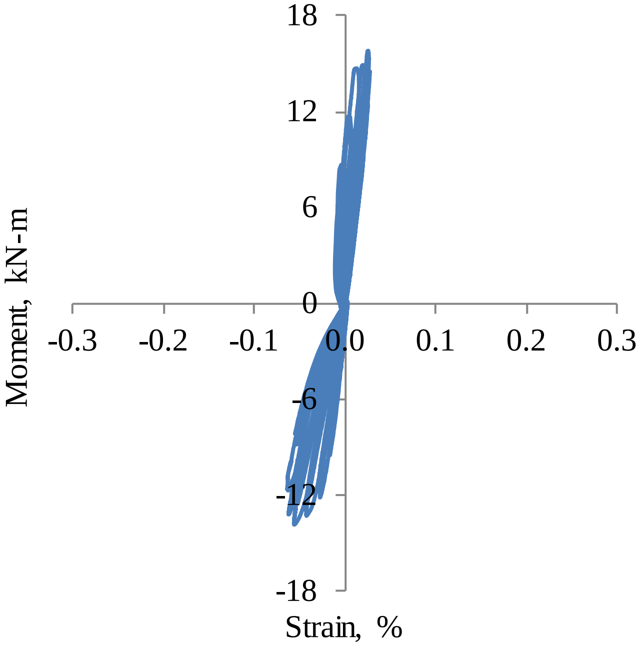

Figure A-27: Moment vs. Strain for Gauge S12 on Specimen 2

A.3 Specimen 3

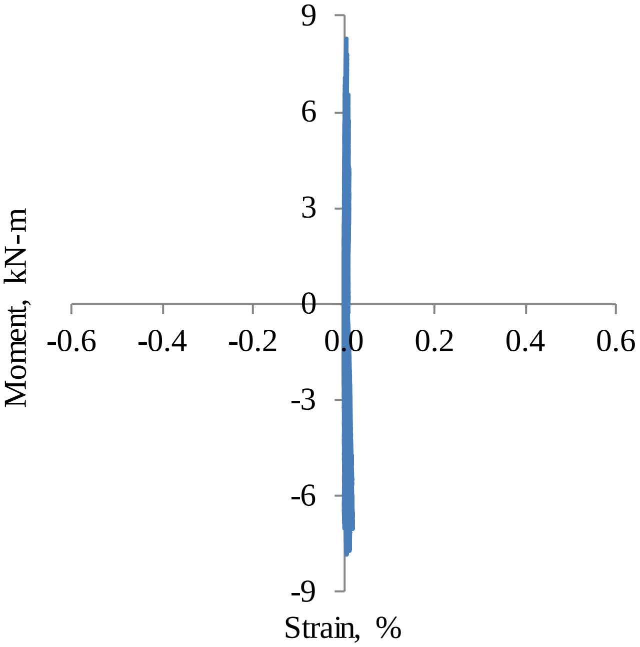

Figure A-28: Moment vs. Strain for Gauge S1 on Specimen 3

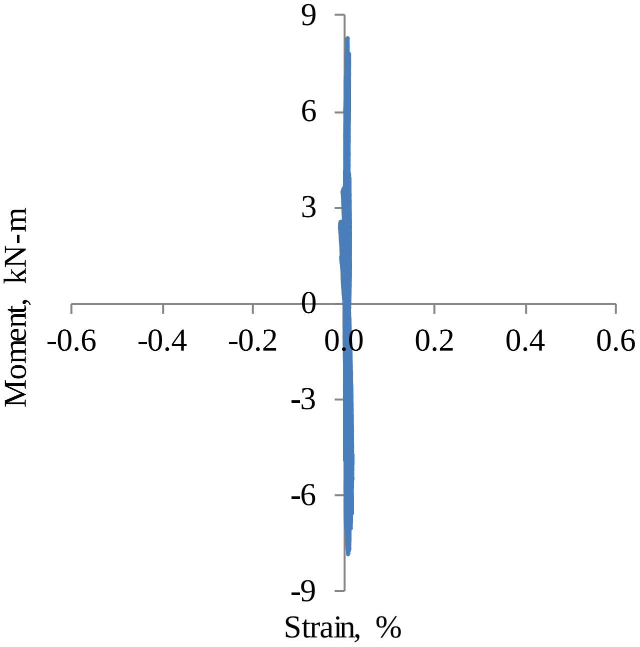

Figure A-29: Moment vs. Strain for Gauge S2 on Specimen 3

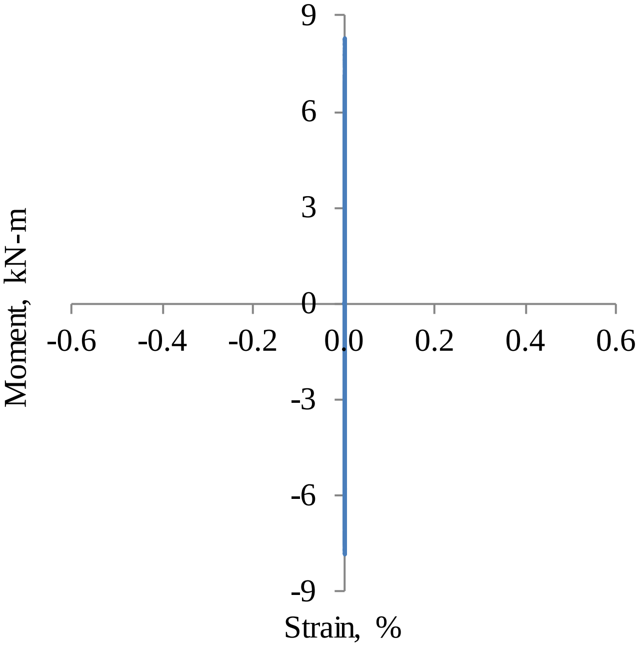

Figure A-30: Moment vs. Strain for Gauge S3 on Specimen 3

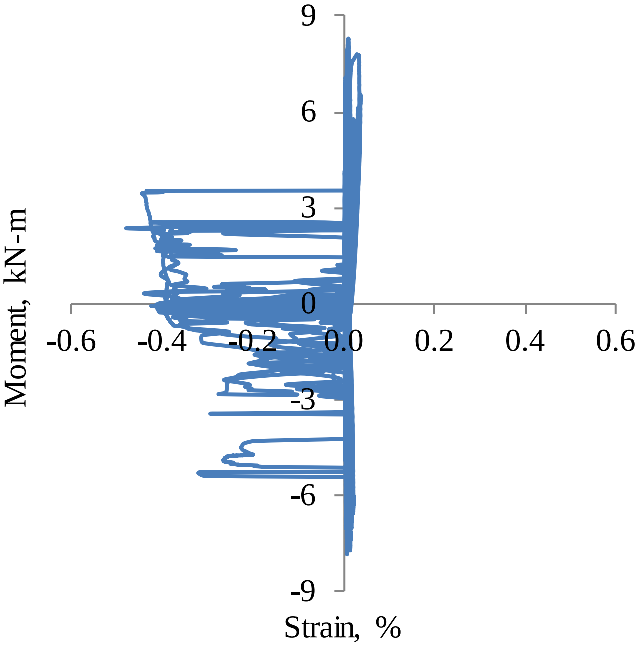

Figure A-31: Moment vs. Strain for Gauge S4 on Specimen 3

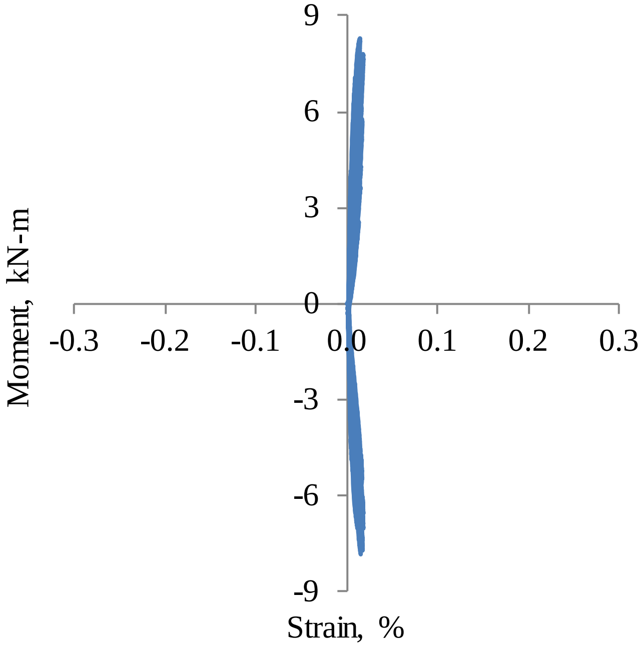

Figure A-32: Moment vs. Strain for Gauge S5 on Specimen 3

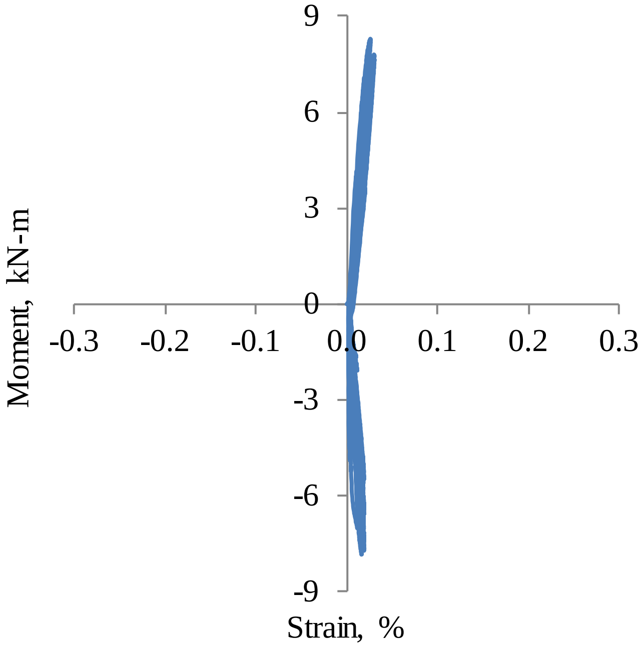

Figure A-33: Moment vs. Strain for Gauge S7 on Specimen 3

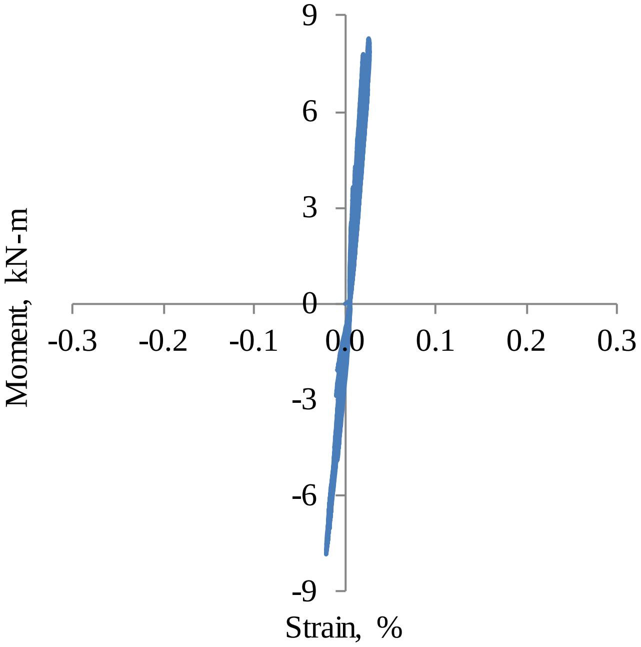

Figure A-34: Moment vs. Strain for Gauge S6 on Specimen 3

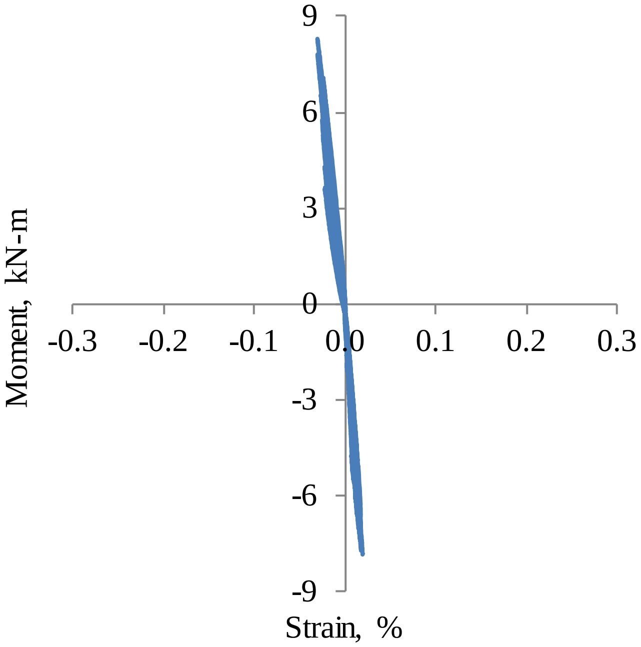

Figure A-35: Moment vs. Strain for Gauge S8 on Specimen 3

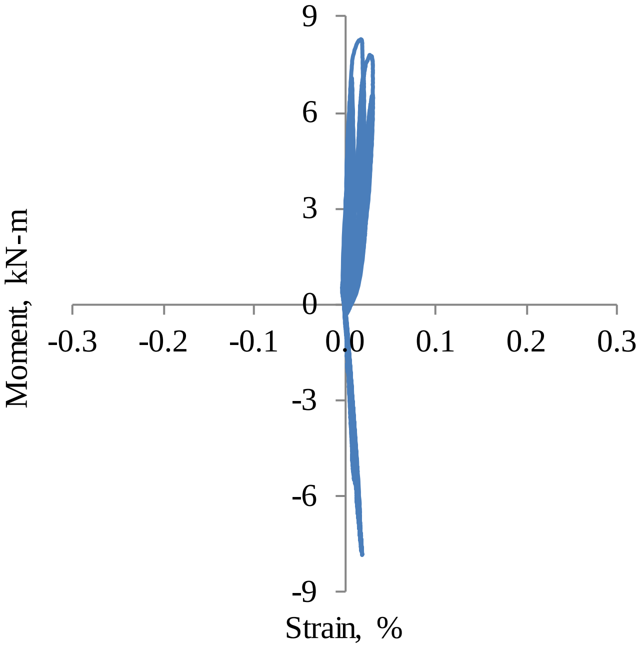

Figure A-36: Moment vs. Strain for Gauge S9 on Specimen 3

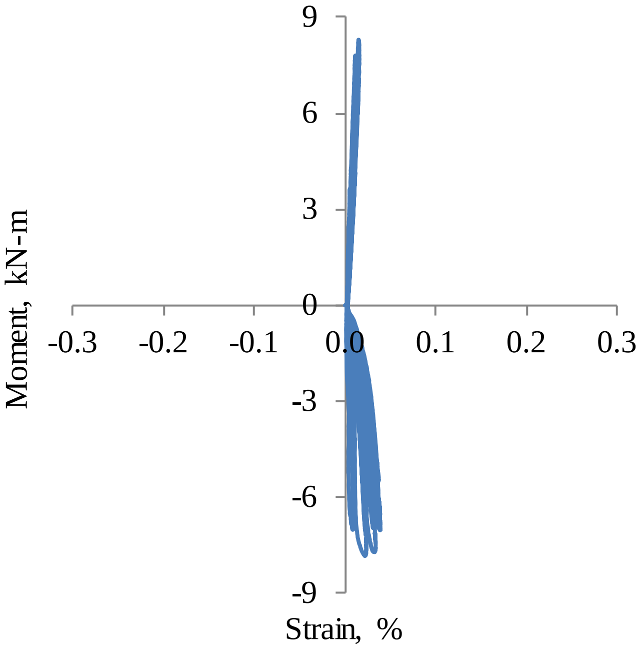

Figure A-37: Moment vs. Strain for Gauge S10 on Specimen 3

APPENDIX B. DISPLACEMENT DATA FROM TESTING

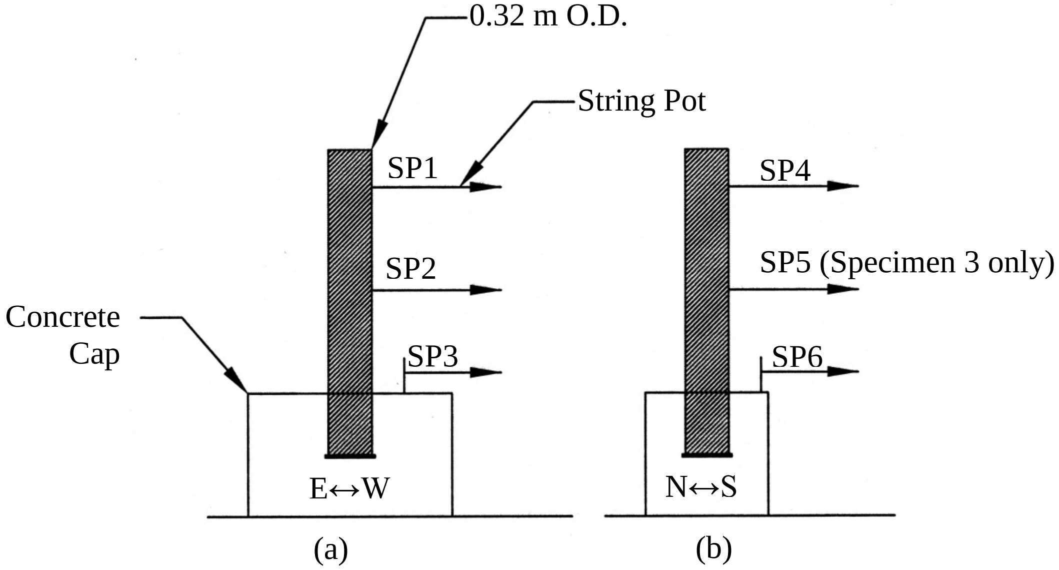
0.32 m O.D.
String Pot
SP1
SP2
SP3
Concrete Cap
E↔W
SP4
SP5 (Specimen 3 only)
SP6
N↔S
(a)
(b)

Figure B-1: String Pots Used to Measure System Response, a) East-West Direction, b) North-South Direction

B.1 Specimen 1

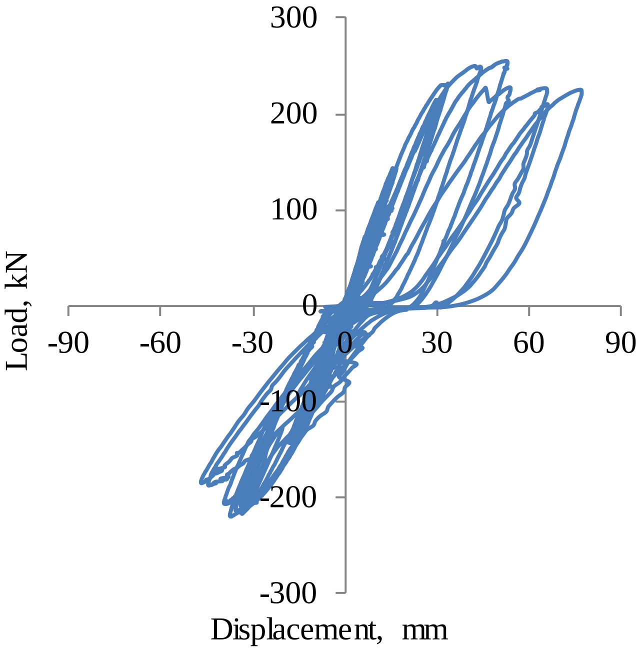

Figure B-2: Load vs. Displacement for SP1 on Specimen 1

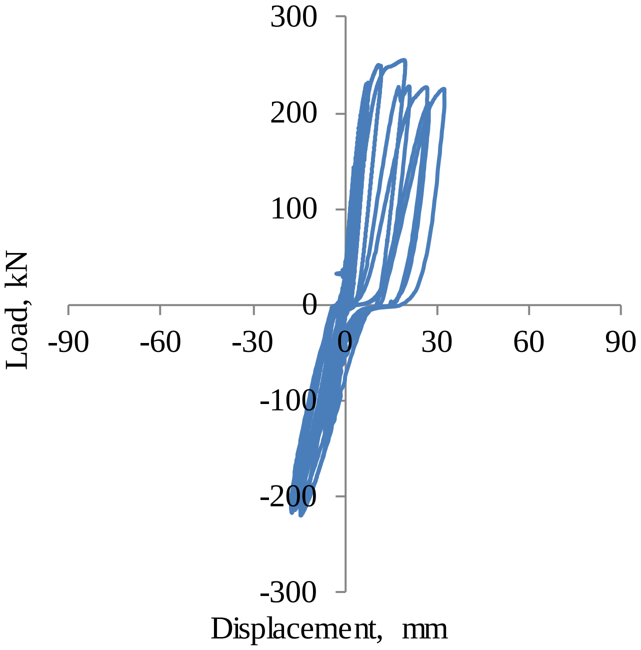

Figure B-3: Load vs. Displacement for SP2 on Specimen 1

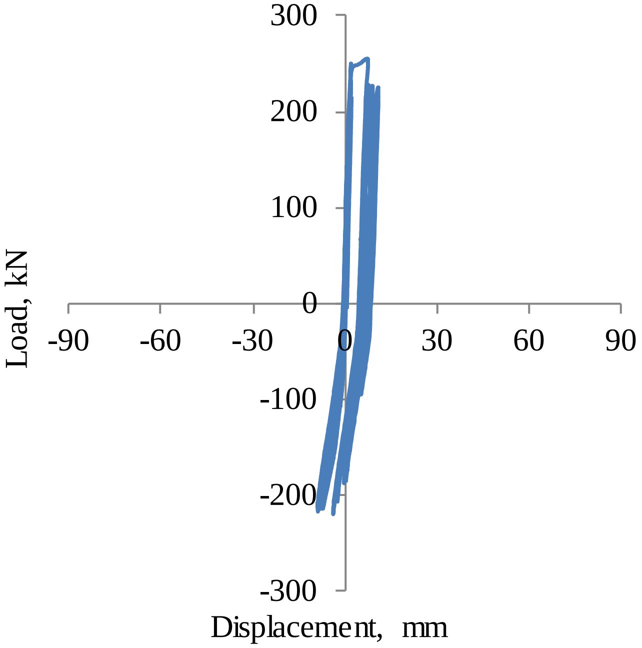

Figure B-4: Load vs. Displacement for SP3 on Specimen 1

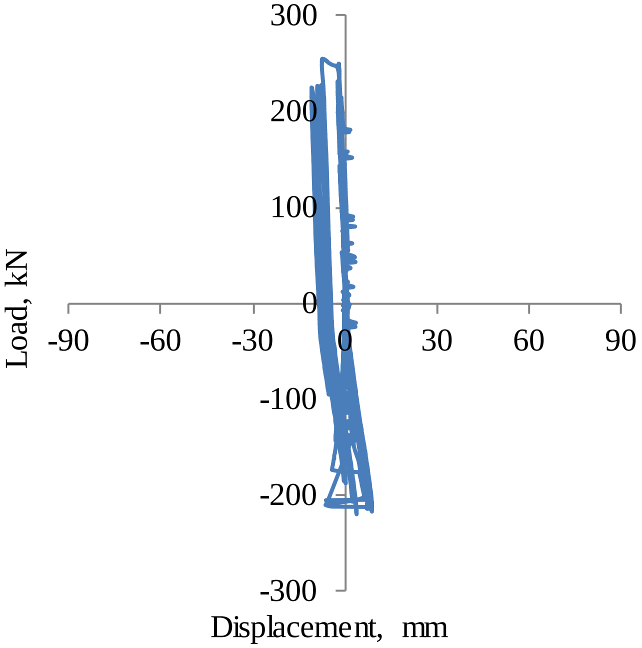

Figure B-5: Load vs. Displacement for SP4 on Specimen 1

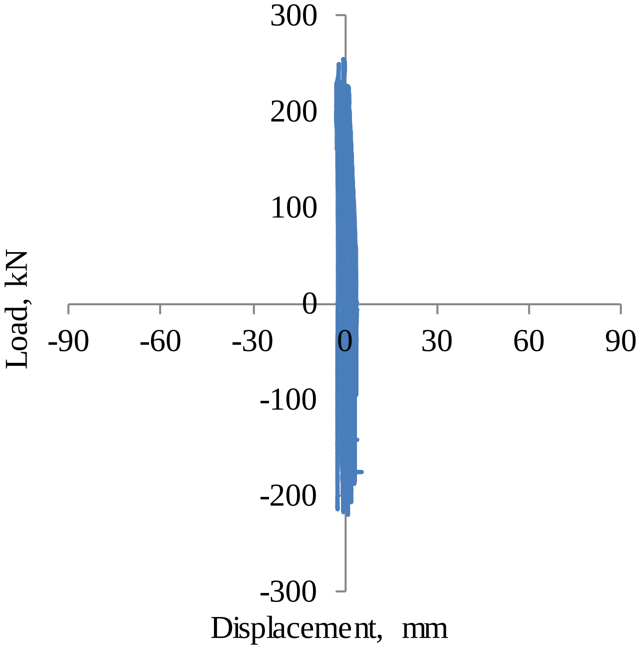

Figure B-6: Load vs. Displacement for SP6 on Specimen 1

B.2 Specimen 2

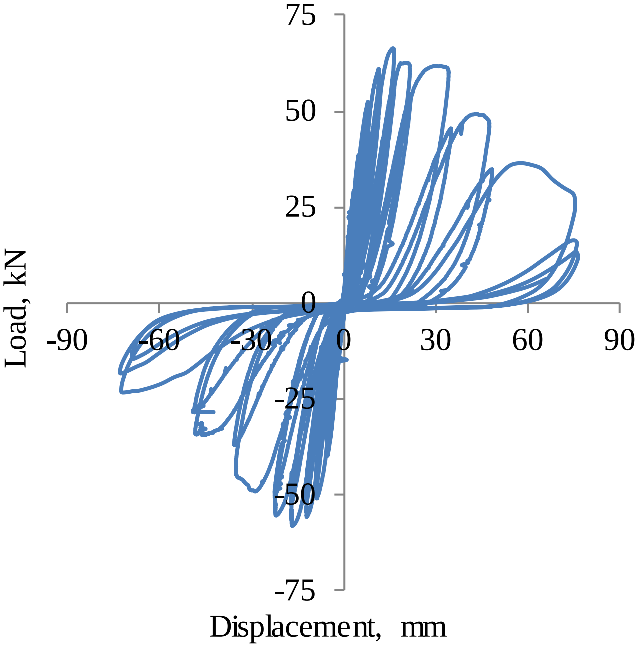

Figure B-7: Load vs. Displacement for SP1 on Specimen 2

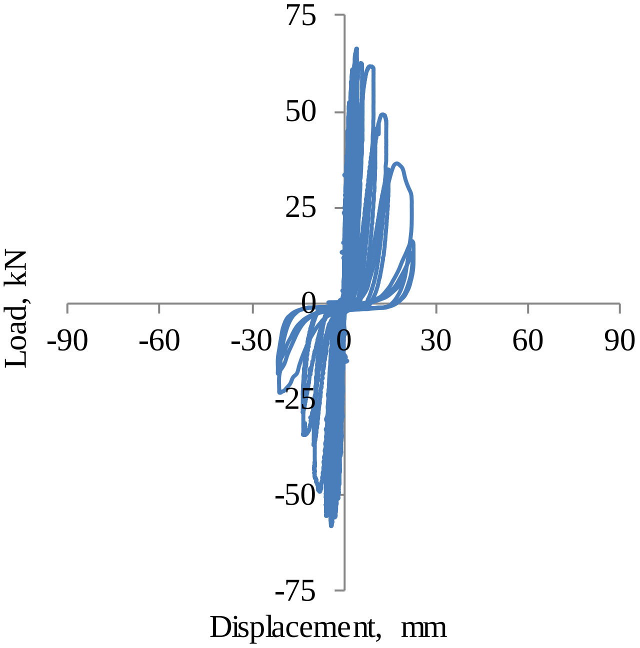

Figure B-8: Load vs. Displacement for SP2 on Specimen 2

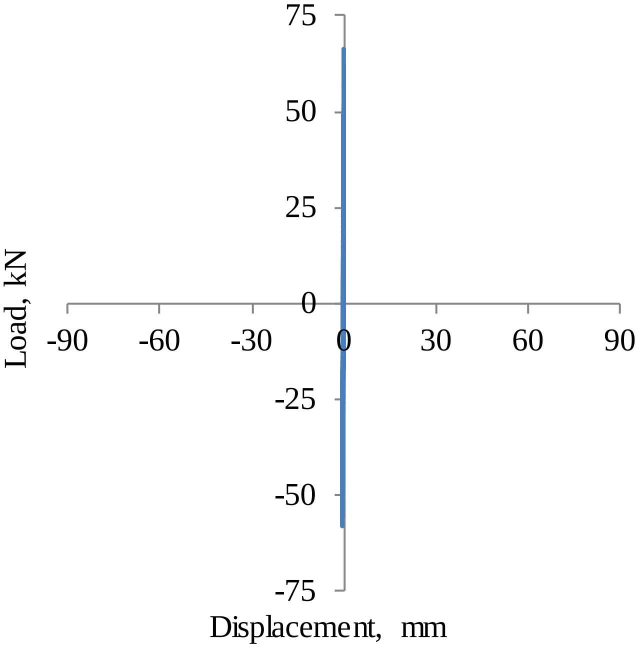

Figure B-9: Load vs. Displacement for SP3 on Specimen 2

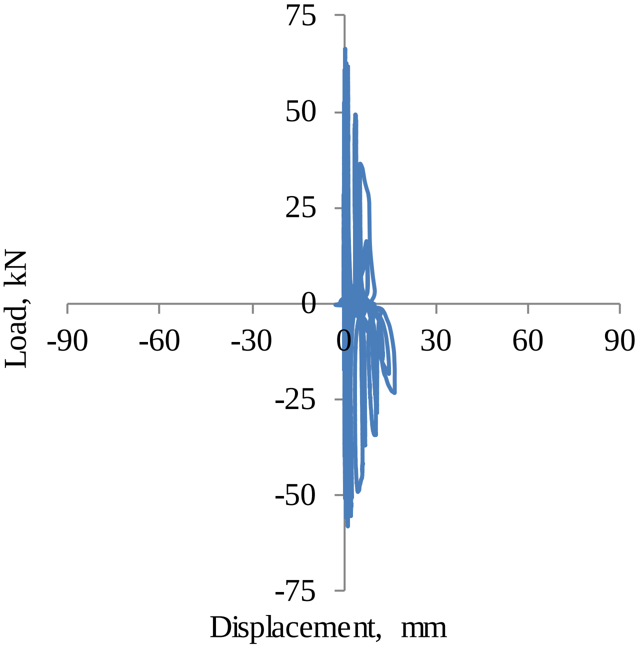

Figure B-10: Load vs. Displacement for SP4 on Specimen 2

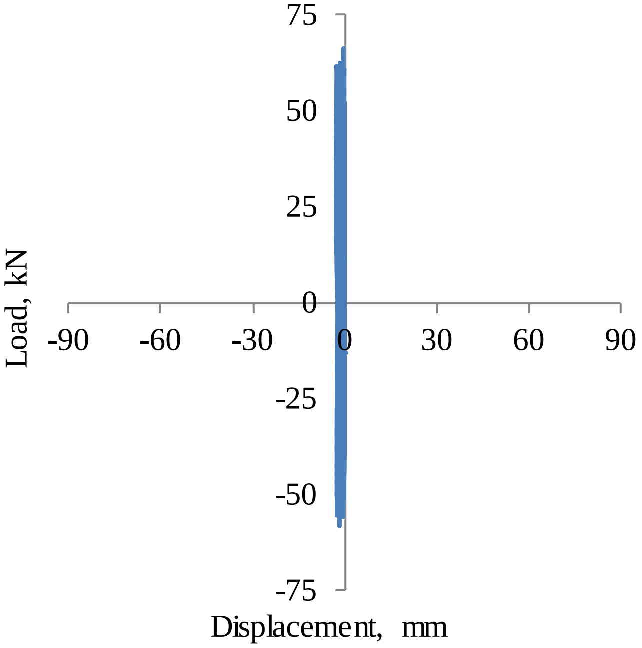

Figure B-11: Load vs. Displacement for SP6 on Specimen 2

B.3 Specimen 3

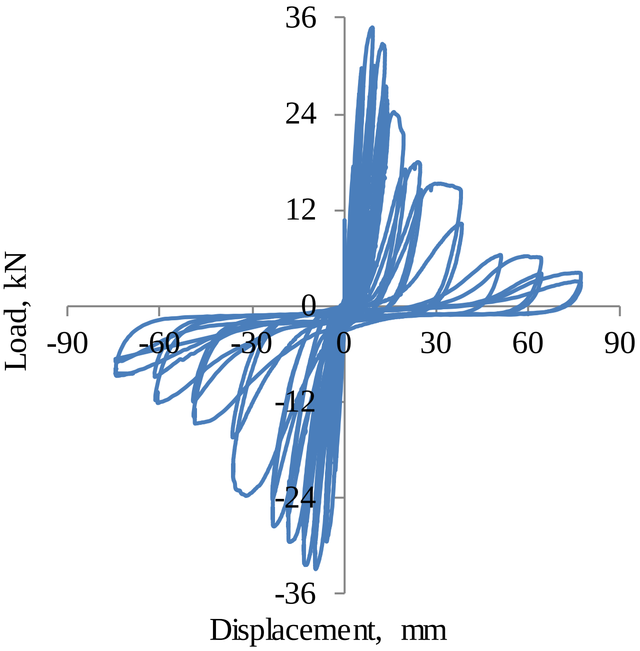

Figure B-12: Load vs. Displacement for SP1 on Specimen 3

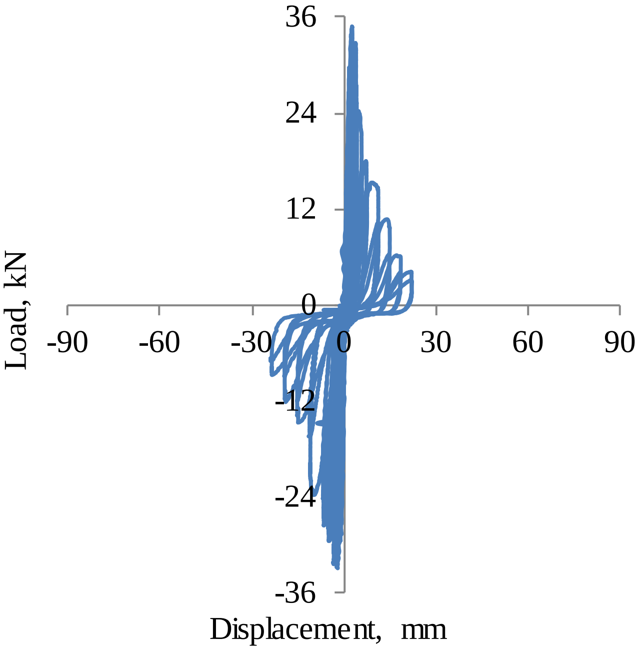

Figure B-13: Load vs. Displacement for SP2 on Specimen 3

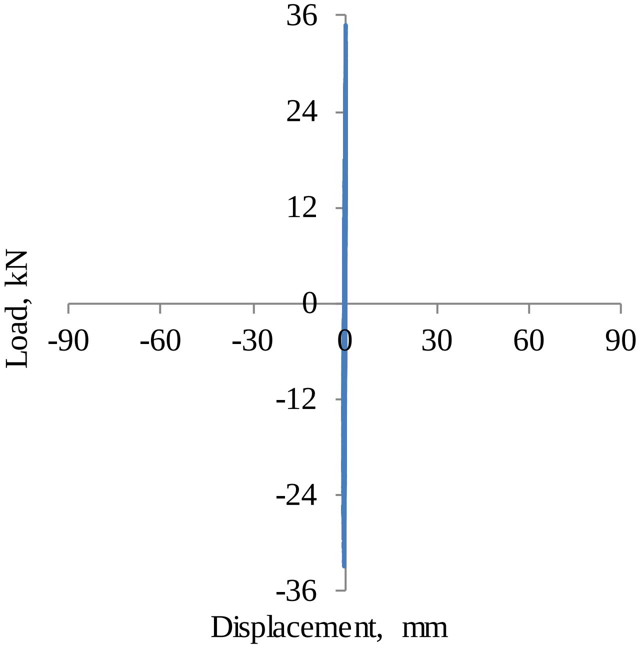

Figure B-14: Load vs. Displacement for SP3 on Specimen 3

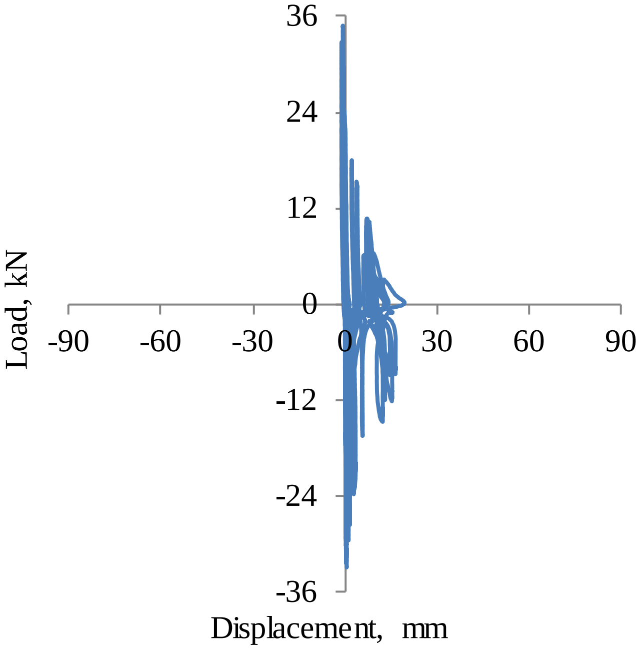

Figure B-15: Load vs. Displacement for SP4 on Specimen 3

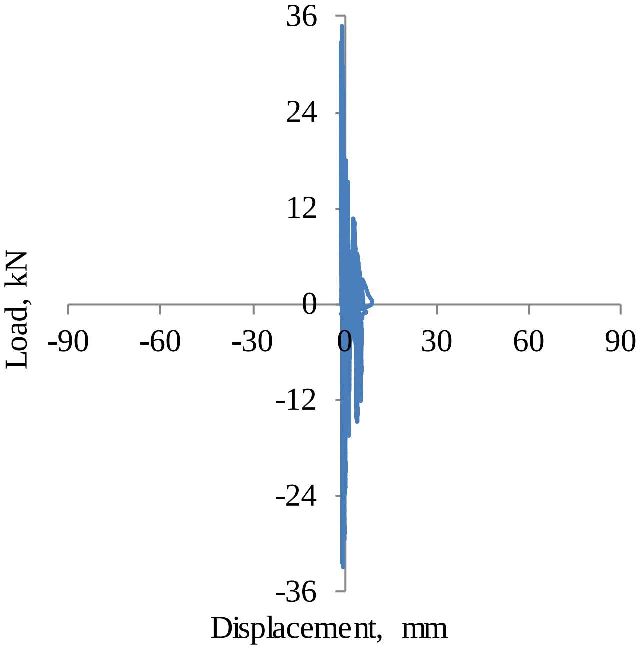

Figure B-16: Load vs. Displacement for SP5 on Specimen 3

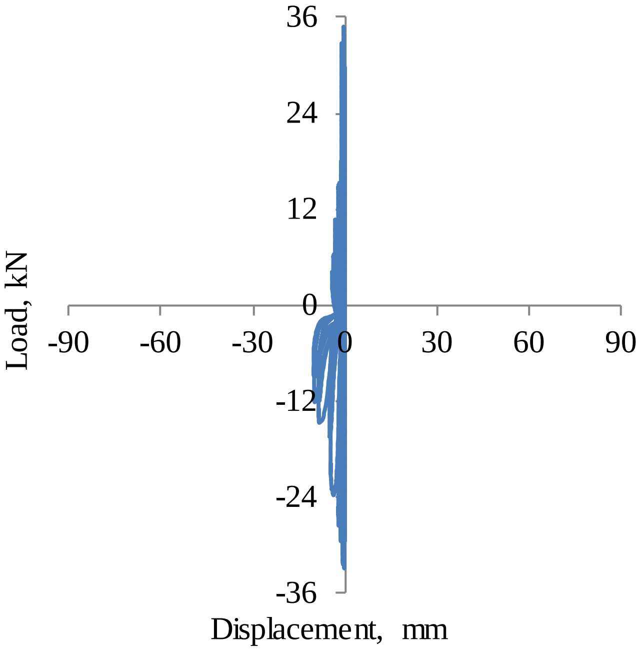

Figure B-17: Load vs. Displacement for SP6 on Specimen 3

APPENDIX C. EXAMPLE OF MARCAKIS AND MITCHELL PROCEDURE

Table C-1 shows the results from an example performed using the procedure presented by Marcakis and Mitchell. This example is based on pile diameter of 0.32 m (12.8 in), a pile embedment depth of 0.46 m (18 in), and a concrete compressive strength of 27.6 MPa (4 ksi).

Table C-1: Data from Marcakis and Mitchell Example

x_f (m)	ε_b	β	α	C_f (kN)	C_b (kN)	V_c (kN)	e (m)	$V_c/f'_c b l_e$	e/l_e
0.24	0.003	0.80	0.92	1585	1443	142	2.82	0.03	6.17
0.25	0.002	0.78	0.93	1651	1348	303	1.31	0.07	2.87
0.26	0.002	0.77	0.92	1717	1245	472	0.82	0.12	1.80
0.27	0.002	0.76	0.90	1783	1137	646	0.58	0.16	1.28
0.28	0.002	0.74	0.87	1849	1028	821	0.44	0.20	0.97
0.29	0.002	0.73	0.84	1915	920	995	0.35	0.24	0.77
0.30	0.002	0.73	0.80	1981	815	1166	0.29	0.29	0.63
0.31	0.001	0.72	0.76	2047	715	1333	0.24	0.33	0.52
0.32	0.001	0.71	0.71	2113	620	1494	0.20	0.37	0.44
0.33	0.001	0.71	0.66	2179	531	1649	0.17	0.40	0.38
0.34	0.001	0.70	0.61	2245	448	1797	0.15	0.44	0.32
0.35	0.001	0.70	0.56	2311	373	1939	0.13	0.47	0.28
0.36	0.001	0.69	0.51	2377	304	2073	0.11	0.51	0.24
0.37	0.001	0.69	0.45	2443	243	2200	0.10	0.54	0.21
0.38	0.001	0.69	0.40	2509	189	2321	0.09	0.57	0.19
0.39	0.001	0.68	0.35	2575	142	2434	0.07	0.60	0.16
0.40	0.000	0.68	0.29	2642	102	2540	0.07	0.62	0.14
0.41	0.000	0.68	0.24	2708	69	2639	0.06	0.65	0.13
0.42	0.000	0.67	0.19	2774	42	2731	0.05	0.67	0.11
0.43	0.000	0.67	0.14	2840	22	2817	0.04	0.69	0.10
0.44	0.000	0.67	0.09	2906	9	2897	0.04	0.71	0.08
0.45	0.000	0.67	0.04	2972	2	2970	0.03	0.73	0.07

APPENDIX D. ADJUSTMENT OF LOADS FROM TESTING

In order to obtain the true horizontal load on the pile, out-of-plane loading due to drift was removed from the actuator load. The drift was obtained from the string pots extending in the north-south direction at the load point of the pile. Using the drift and the distance from the reaction frame to the displaced position of the pile, a drift angle was calculated. This angle was then used to determine the components of the resultant load reported from the actuator. This adjustment had little impact on the original loads recorded during testing.

APPENDIX E. PILE END BEARING STRESS

E.1 Magnitude of Pile End Bearing Stress

The magnitude of the pile end bearing resultant can be found by determining the volume of a cylindrical wedge. Figure E-1 shows a plan view and a side view of half of a cylindrical wedge divided up into triangles with a width of *dx*. Each triangle has a variable base and height.

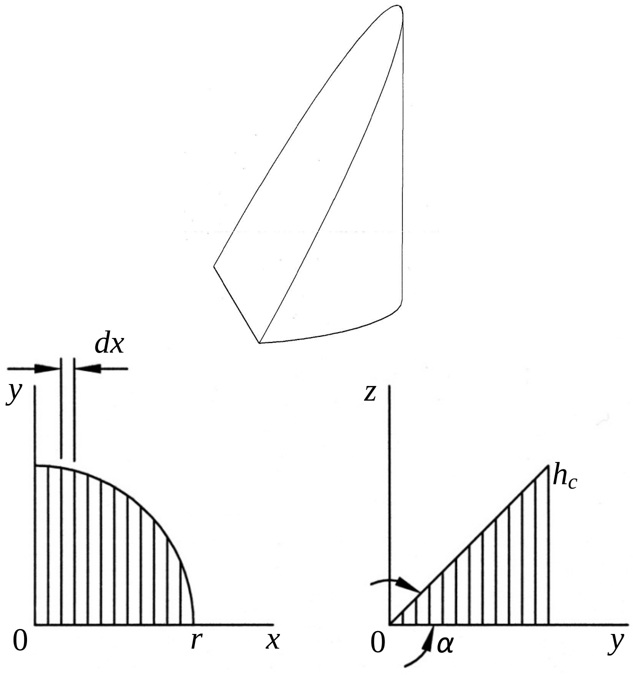

(a) (b)

Figure E-1: Integration of Cylindrical Wedge, a) Top View, b) Side View

The base of each triangle is defined by the equation of a circle with radius, r, and is given by equation E-1.

$$y = \sqrt{r^2 - x^2} \tag{E-1}$$

where:
y = base of triangle
x = distance from centerline of wedge

The height of each triangle, h_t, is dependent upon the base and the angle, α, and is given by equation E-2.

$$h_t = y \tan \alpha \tag{E-2}$$

where:
$\tan \alpha = \frac{h_c}{r}$
h_c = total height of wedge

Using equations E-1 and E-2, the area of each triangle can then be determined as given in equation E-3.

$$A = \frac{1}{2} y h_t \tag{E-3}$$

where:
A = area of triangle

Half of the volume of the wedge can then be calculated by integrating the area of each triangle from 0 to r. This volume can then be doubled to obtain the entire volume of the wedge as given by equation E-4.

$$V = 2 \int_0^r A \, dx \tag{E-4}$$

Substituting equations E-1, E-2, and E-3 into equation E-4 and simplifying gives equation E-5.

$$V = \frac{h_c}{r}\int_0^r r^2 - x^2 \, dx \tag{E-5}$$

Integrating equation E-5 gives equation E-6. This equation can be expressed in terms of the diameter, D, of the cylindrical wedge as given in equation E-7.

$$V = \frac{2}{3}h_c r^2 \tag{E-6}$$

$$V = \frac{1}{6}h_c D^2 \tag{E-7}$$

E.2 Location of Pile End Bearing Stress

The distance, d_e, to the centroid of a solid can be found by using equation E-8. To find the distance to the centroid of a cylindrical wedge, the wedge is divided into triangles as was done previously to find the volume.

$$d_e = \frac{\sum V_i \overline{x_i}}{\sum V} \tag{E-8}$$

The volume of each triangle is defined in equation E-9. The area, A, is the same area that was defined in equation E-3.

$$V_i = A \, dx \tag{E-9}$$

The distance to the centroid of each triangle, $\overline{x_i}$, is given by equation E-10 in terms of the base of the triangle, y.

$$\overline{x_i} = \frac{2}{3}y \tag{E-10}$$

The volume of the wedge was defined previously in equation E-7. Inserting these equations into equation E-8 and simplifying produces the integral in equation E-11.

$$d_e = \frac{1}{r^3}\int_0^r (r^2 - x^2)^{\frac{3}{2}}\ dx \tag{E-11}$$

If equation E-11 is rearranged as given in equation E-12, the integral can be simplified using the trigonometric substitution given by equation E-13.

$$d_e = \frac{1}{r^3}\int_0^r \left[r^2\left(1 - \left(\frac{x}{r}\right)^2\right)\right]^{\frac{3}{2}}\ dx \tag{E-12}$$

$$\sin\alpha = \frac{x}{r} \tag{E-13}$$

Rearranging equation E-13 and differentiating both sides of the equation gives equation E-14.

$$dx = r\cos\alpha\, d\alpha \tag{E-14}$$

Substituting equations E-13 and E-14 into equation E-12 produces equation E-15. The bounds of integration have also been changed due to the trigonometric substitution.

$$d_e = \frac{1}{r^3}\int_0^{\frac{\pi}{2}} \left[r^2\left(1 - \sin^2\alpha\right)\right]^{\frac{3}{2}} r\cos\alpha\ d\alpha \tag{E-15}$$

Simplifying equation E-15 and substituting the trigonometric identity presented in equation E-16 gives equation E-17.

$$\cos^2\alpha = 1 - \sin^2\alpha \tag{E-16}$$

$$d_e = r\int_0^{\frac{\pi}{2}} \cos^4\alpha\, d\alpha \tag{E-17}$$

To further simplify the integration, the half-angle formula presented in equation E-18 is substituted into equation E-17 giving equation E-19.

$$\cos^2 \alpha = \frac{1 + \cos 2\alpha}{2} \tag{E-18}$$

$$d_e = r \int_0^{\frac{\pi}{2}} \left(\frac{1 + \cos 2\alpha}{2}\right)^2 d\alpha \tag{E-19}$$

Expanding equation E-19 gives equation E-20.

$$d_e = \frac{r}{4} \int_0^{\frac{\pi}{2}} (1 + 2\cos 2\alpha + \cos^2 2\alpha)\, d\alpha \tag{E-20}$$

The half-angle formula introduced as equation E-18 is then substituted in to the third term of equation E-20. This substitution is shown in Equation E-21.

$$d_e = \frac{r}{4} \int_0^{\frac{\pi}{2}} \left(1 + 2\cos 2\alpha + \frac{1 + \cos 4\alpha}{2}\right) d\alpha \tag{E-21}$$

Performing the integration and simplifying gives equation E-22. This equation can be expressed in terms of the diameter, *D*, of the cylindrical wedge as given in equation E-23.

$$d_e = \frac{3\pi r}{16} \tag{E-22}$$

$$d_e = \frac{3\pi D}{32} \tag{E-23}$$

APPENDIX F. EXAMPLE OF ULTIMATE STRENGTH MODEL

Table F-1 shows the results from an example performed using the ultimate strength model. This example is based on a pile-to-cap connection with a pile diameter of 0.32 m (12.8 in) and a concrete compressive strength of 27.6 MPa (4.0 ksi). The shear span of the pile is 1.52 m (60 in). In addition, a 0.37 m (14.5 in) diameter plate is welded to the end of the pile embedded in the concrete cap. A coefficient of friction equal to 0.35 was used in calculating the friction force at the back of the connection.

Table F-1: Data from Ultimate Strength Example

l_e (m)	ε_b (m/m)	β	α	σ_e (MPa)	x_f (m)	C_f (kN)	C_b (kN)	C_e (kN)	V_c (kN)
0.03	0.003	0.81	0.92	25.34	0.01	87	82	28.6	4.8
0.05	0.003	0.81	0.92	25.38	0.03	174	163	57.0	11.2
0.08	0.003	0.81	0.92	25.41	0.04	262	243	85.1	18.9
0.10	0.003	0.81	0.92	25.45	0.05	350	322	112.8	28.1
0.13	0.003	0.80	0.92	25.47	0.07	440	401	140.4	38.6
0.15	0.003	0.80	0.92	25.50	0.08	529	479	167.6	50.4
0.18	0.003	0.80	0.93	25.52	0.09	619	556	194.6	63.5
0.20	0.003	0.80	0.93	25.54	0.11	710	632	221.3	77.8
0.23	0.003	0.80	0.93	25.55	0.12	801	708	247.8	93.4
0.25	0.003	0.80	0.93	25.56	0.14	893	783	274.0	110.1
0.28	0.003	0.80	0.93	25.57	0.15	985	857	300.0	128.0
0.30	0.003	0.79	0.93	25.58	0.16	1078	931	325.8	147.0
0.33	0.003	0.79	0.93	25.59	0.18	1171	1004	351.3	167.0
0.36	0.003	0.79	0.93	25.59	0.19	1264	1076	376.6	188.1
0.38	0.003	0.79	0.93	25.60	0.21	1358	1148	401.8	210.2
0.41	0.003	0.79	0.93	25.60	0.22	1452	1219	426.6	233.3
0.43	0.003	0.79	0.93	25.60	0.23	1547	1290	451.3	257.3
0.46	0.003	0.79	0.93	25.60	0.25	1642	1360	475.8	282.2
0.48	0.003	0.79	0.93	25.59	0.26	1737	1429	500.1	308.1
0.51	0.002	0.78	0.93	25.59	0.28	1833	1498	524.3	334.7